Hyperthermal reactions of O(p3sP) with hydrogen and methane
by Donna Joan Garton

A dissertation submitted in partial fulfillment of the requirements for the degree of Doctor of Philosophy in Chemistry
Montana State University

Abstract:
Hyperthermal reactions of O(3P) occur at the surfaces and in the exhaust gases of spacecraft that travel through the residual atmosphere of the Earth at high altitudes (200-600 km). These reactions may degrade materials through oxidation and erosion, or they may yield internally excited reaction products which emit radiation and contribute to the "signature" of a rocket plume. Crossed-beams experiments were used to study model reactions of O(3P) with H2, D2, CH4, and CD4 at center-of-mass collision energies in the range 8-75 kcal mol^-1. Interpretation of the experimental results has been strengthened by theoretical calculations carried out by collaborators. A study of the OH scattered flux as a function of collision energy has led to the determination of an experimental excitation function in the threshold region for the O(3P)+H2 → OH+H reaction. The experimental excitation function clearly matched the theoretical prediction, which confirmed that the laser-detonation source produces O(3P) atoms. The excitation function for the O(3P) + H2 reaction and the dynamics of the O(3P) + D2 reaction, observed experimentally for the first time, demonstrate that these reactions proceed mainly on triplet potential energy surfaces, with little or no intersystem crossing. Experiments on the reactions of O(3P) with methane have revealed a previously unobserved reaction pathway, which involves H-atom elimination: O(3P) + CH4 → OCH3 + H. The excitation function for this reaction has been measured, and the reaction barrier has been determined to be □46 kcal mol^-1. In addition, the expected H-atom abstraction reaction, O(3P) + CH4 → CH3 + OH, has been observed, and the dynamics have been investigated. Theoretical calculations identify a triplet-singlet curve crossing below the triplet barrier for the H-atom elimination reaction, but the observed dynamics indicate reaction exclusively on the two lowest-lying triplet surfaces. While it remains to be seen whether intersystem crossing will affect the outcome of other reactions involving hyperthermal atomic oxygen, unknown reactions which have high barriers are likely to be common in extreme environments such as low-Earth orbit, where spacecraft surfaces and exhaust gases suffer high-energy collisions with ambient atomic oxygen.

HYPERTHERMAL REACTIONS OF O(^3P) WITH HYDROGEN AND METHANE

by

Donna Joan Garton

A dissertation submitted in partial fulfillment
of the requirements for the degree

of

Doctor of Philosophy

in

Chemistry

MONTANA STATE UNIVERSITY
Bozeman, Montana

April 2004

APPROVAL

of a dissertation submitted by

Donna Joan Garton

This dissertation has been read by each member of the dissertation committee and has been found to be satisfactory regarding content, English usage, format, citations, bibliographic style, and consistency, and is ready for submission to the College of Graduate Studies.

Lee Spangler _____ 4/16/04
Date

Approved for the Department of Chemistry

Paul A. Grieco _____ 4-16-04
Date

Approved for the College of Graduate Studies

Bruce McLeod _____ 4-19-04
Date

STATEMENT OF PERMISSION TO USE

In presenting this dissertation in partial fulfillment of the requirements for a doctoral degree at Montana State University, I agree that the Library shall make it available to borrowers under rules of the Library. I further agree that copying of this dissertation is allowable only for scholarly purposes, consistent with "fair use" as prescribed in the U.S. Copyright Law. Requests for extensive copying or reproduction of this dissertation should be referred to Bell & Howell Information and Learning, 300 North Zeeb Road, Ann Arbor, Michigan 48106, to whom I have granted "the exclusive right to reproduce and distribute my dissertation in and from microform along with the non-exclusive right to reproduce and distribute my abstract in any format in whole or in part."

Signature 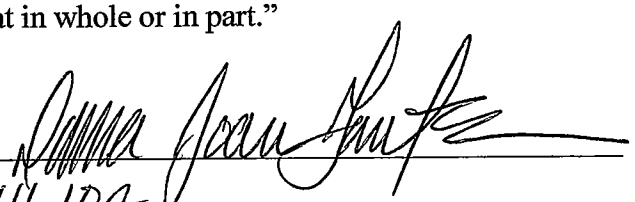

Date 4/16/04

TABLE OF CONTENTS

TABLE OF CONTENTS - CONTINUED

LIST OF FIGURES

LIST OF FIGURES - CONTINUED

Figure Page

LIST OF FIGURES - CONTINUED

Figure Page

LIST OF FIGURES - CONTINUED

Figure Page

LIST OF FIGURES - CONTINUED

Figure Page

ABSTRACT

Hyperthermal reactions of $O(^3P)$ occur at the surfaces and in the exhaust gases of spacecraft that travel through the residual atmosphere of the Earth at high altitudes (200-600 km). These reactions may degrade materials through oxidation and erosion, or they may yield internally excited reaction products which emit radiation and contribute to the "signature" of a rocket plume. Crossed-beams experiments were used to study model reactions of $O(^3P)$ with H_2, D_2, CH_4, and CD_4 at center-of-mass collision energies in the range 8 - 75 kcal mol^{-1}. Interpretation of the experimental results has been strengthened by theoretical calculations carried out by collaborators. A study of the OH scattered flux as a function of collision energy has led to the determination of an experimental excitation function in the threshold region for the $O(^3P) + H_2 \rightarrow OH + H$ reaction. The experimental excitation function clearly matched the theoretical prediction, which confirmed that the laser-detonation source produces $O(^3P)$ atoms. The excitation function for the $O(^3P) + H_2$ reaction and the dynamics of the $O(^3P) + D_2$ reaction, observed experimentally for the first time, demonstrate that these reactions proceed mainly on triplet potential energy surfaces, with little or no intersystem crossing. Experiments on the reactions of $O(^3P)$ with methane have revealed a previously unobserved reaction pathway, which involves H-atom elimination: $O(^3P) + CH_4 \rightarrow OCH_3 + H$. The excitation function for this reaction has been measured, and the reaction barrier has been determined to be ~46 kcal mol^{-1}. In addition, the expected H-atom abstraction reaction, $O(^3P) + CH_4 \rightarrow CH_3 + OH$, has been observed, and the dynamics have been investigated. Theoretical calculations identify a triplet-singlet curve crossing below the triplet barrier for the H-atom elimination reaction, but the observed dynamics indicate reaction exclusively on the two lowest-lying triplet surfaces. While it remains to be seen whether intersystem crossing will affect the outcome of other reactions involving hyperthermal atomic oxygen, unknown reactions which have high barriers are likely to be common in extreme environments such as low-Earth orbit, where spacecraft surfaces and exhaust gases suffer high-energy collisions with ambient atomic oxygen.

INTRODUCTION

Spacecraft in the Low-Earth Orbital Environment

The low-Earth orbital environment, having an altitude range of 200 to 600 km, is host to many short-term and long-term spacecraft, including the International Space Station (350-460 km), space shuttle (~300 km), a large number of private and government satellites, such as communications satellites, and missiles. During their time in low-Earth orbit (LEO) these spacecraft are surrounded by a strongly oxidizing residual atmosphere predominantly composed of atomic oxygen.[1] At typical space shuttle altitudes, the oxygen atom number density is on the order of 10^9 cm^{-3}.[1-3] Most of the oxygen atoms are in the ground, or $O(^3P)$, electronic state, while only 0.001 percent is estimated to be in the first excited state, $O(^1D)$.[2] In addition to the presence of neutral oxygen atoms, there are other neutral species, such as N_2, He, and O_2, with number densities at least ten times lower than the oxygen atoms, and there is also a small ionic component to the LEO atmosphere, of which the most abundant ion, O^+, is 10^4 times less dense than oxygen atoms.[2,4,5]

As spacecraft move in their orbits at relative velocities of about ~7.4 km s^{-1} (accounting for co-rotation of the orbit), they collide with the residual atmosphere.[6,7] At orbital altitudes of ~300-400 km, collisions between the spacecraft surfaces and ambient oxygen atoms have a mean collision energy around 108 kcal mol^{-1}. The roughly 1000 K kinetic temperature[1] of the atmosphere gives an energy spread (full width at half maximum) of ~48 kcal mol^{-1} to the collisions.[7] The collision energy of oxygen atoms striking exhaust plume species released from the spacecraft is not as well defined, as it is heavily dependent on the relative velocity between the two collision partners. The high-energy collisions between oxygen atoms and spacecraft surfaces lead to erosion and oxidation of surface materials, in particular polymers,

compromising the integrity of external surfaces,[8,9] while collisions between spacecraft exhaust species and oxygen atoms result in chemiluminescent products,[10] which have important implications in spacecraft tracking and surveillance, such as identification of the country of origin of a spacecraft or missile. Understanding the chemistry occurring during these high energy, or hyperthermal, collisions of oxygen atoms with spacecraft surfaces and with exhaust plume species is only beginning to be uncovered.

Polymer Erosion in LEO

Energetic collisions of oxygen atoms with spacecraft surfaces are considered to be one of the most important hazards to spacecraft in LEO, because such collisions can lead to eventual failure of exposed materials.[8,9] The detrimental effects of atomic oxygen in LEO were first recognized after post-flight analyses of polymer surfaces that were exposed during the earliest space shuttle flights.[11,12] The polymers showed a loss of surface gloss and concomitant weight loss. Concern over the degradation of materials by atomic oxygen sparked a huge effort, involving space- and ground-based studies, that has been aimed at the identification, understanding, and mitigation of problems caused by atomic oxygen in LEO.[13]

Despite such efforts, uncovering the details of the chemistry behind the oxygen atom erosion of polymers has been a formidable task. Progress towards understanding this chemistry has largely been accomplished, to varying degrees of success, by measuring mass loss during exposure of various polymers to oxygen atoms[14] and studying the chemical structure of the surface before, during, and after exposure.[15] While these approaches provide information about the net result of the complex reactions that are occurring at a polymer surface during exposure to atomic oxygen and allow inferences to be made about the chemical and physical interactions at the surface, they are an insensitive probe of the individual reaction and interaction mechanisms that combine to produce the net result. Experiments can be designed, however,

to study the individual steps of the overall erosion process, from initial interactions of oxygen atoms with a surface (initiation), to oxidation of carbon and scission of the hydrocarbon bond (propagation), and ultimate removal of volatile carbon-containing species (material loss).

Chemiluminescence From O-Atom Reactions with Rocket Plumes

Orbiting spacecraft in and missiles traveling through LEO exhaust plumes of combustion products and unburned fuel when using thrusters to adjust their position in orbit or to maintain their velocity. Other gaseous species, mostly H_2O, may be released from outgassing of materials in the space vacuum. Species within the exhaust plumes, which include fully and partially combusted fuel (including hydrocarbon fuel, in particular CH_4)[10], oxidizer, and possibly other chemical "countermeasures", interact with the ambient oxygen atoms at high center-of-mass (c.m.) collision energies forming internally excited products that produce radiative emissions around the space vehicle. Although some collisions have sufficient energy to form electronically excited products that can emit visible or ultraviolet radiation, it is more common for products to be formed with vibrational and rotational excitation, thus leading to emission of infrared radiation.[10] Both inelastic scattering, $O + X \rightarrow O + X^*$, and reactive scattering, $O + XY \rightarrow OX^* + Y^{**}$, can lead to infrared emissions.[10,16,17] Some efforts have been made to study these interactions in space by optical measurements of rocket firings or fuel dumps, but the experiments are costly and the spectra are extremely complicated by the complex environment.[10,18] More controlled studies can be made in the laboratory wherein identification of the chemical components released by a spacecraft from the spectral signatures can be accomplished by studying the products formed in the collisions and energy partitioning (i.e. electronic, translational, etc.) following the collisions. This information can then be used by theoreticians and modelers to calculate the expected emission spectra. Once the emission

spectra are known, the type of fuel used to propel the spacecraft or the gasses released around the vehicle can be determined. The ability to analyze and identify species in spectral signatures of spacecraft and missile plumes is considered to be a vital component of a modern missile defense.

From LEO to the Laboratory: Simulating Oxygen Atom Reactions Occurring in LEO

Recreating oxygen-atom reactions occurring in the LEO environment for controlled studies in the laboratory is no trivial task. In order to obtain the collision energy range observed in interactions occurring in LEO, experimentalists have two choices, one of which is accelerating a polymer or intact gaseous molecule, in a controlled fashion, to 7.4 km s^{-1} (16,500 mph), exposing it to a beam of thermal $O(^3P)$, and observing reactions occurring upon collision. The other is creating an oxygen atom beam with a velocity of 7.4 km s^{-1}, directing it to react with a stationary polymer surface or other slow-moving molecular collision partner, and making measurements during the collision. While neither option is simple, it is easier to create a high-velocity beam of atoms than accelerate a polymer or intact molecule to such high velocities. Creating a beam of oxygen atoms is an arduous endeavor because of their very high reactivity. Only a few sources of high-velocity oxygen atoms have been developed over the past 20 years. These include the ion neutralization, laser-sustained discharge, electron stimulated desorption, and laser detonation sources. A review of these and other lower energy oxygen atom sources may be found in Ref. 19. Of the sources mentioned, the laser detonation source has a relatively high flux and is well characterized in terms of beam velocity and by-products, such as light and ions. This source is also one of the only sources to be rigorously characterized in terms of the electronic states of the oxygen atoms in the beam; this work will be discussed in Chapter 3 of this thesis. Details on the operation of the laser detonation source are presented in Chapter 2.

Relevant Oxygen Atom Chemistry

Oxygen Atom Reactions with Hydrogen

While the $O(^3P) + H_2 \rightarrow OH + H$ reaction has only minor relevance to plume chemistry and hydrocarbon erosion in LEO, it is an important reaction for determining the electronic state composition of oxygen atoms produced from the laser detonation source without the use of spectroscopic methods, which are currently unavailable in our laboratory. The knowledge of the electronic state composition of the oxygen atom beam is a cornerstone upon which the understanding of all further reactions discussed in this thesis was built. While details of the beam characterization will be discussed in Chapter 3, a brief background on the $O(^3P)$, $O(^1D) + H_2$ reactions will be provided in this section.

Studies on the $O(^3P) + H_2 \rightarrow OH + H$ reaction span nearly 50 years largely because it is a prototype for hydrogen-atom abstraction reactions and is one of the key reactive steps in hydrogen and hydrocarbon combustion. The OH and H products are "simple" to detect experimentally and the reaction is amenable to thorough theoretical probing, offering a wealth of dynamical information, such as abstraction versus insertion mechanisms and curve crossing effects. Efforts to date have involved many theoretical and experimental approaches,[20-37] however, no experiments have been done that directly probe the reaction dynamics. The reason for this knowledge gap in this simple and prototypical triatomic system is partially due to the high reaction barrier, ~9 kcal mol^{-1}, and the small reduced mass of this system. Since the energy available for reaction is the center-of-mass collision energy, which is given by $E_{coll} = \frac{1}{2}\mu v_{rel}^2$, relative velocities near 8 km s^{-1} are required in order the achieve sufficient collision energy for the reaction to occur with thermal H_2. As discussed in the previous section, creating such an oxygen atom beam is an experimental challenge.

An additional experimental difficulty in studying the $O(^3P) + H_2$ reaction is the possible presence of the first electronic excited state of oxygen $O(^1D)$ in the oxygen atom reactant

beam. In contrast to the $O(^3P)$ reactions, the first electronic excited state of atomic oxygen, $O(^1D)$, which lies 45.4 kcal mol^{-1} higher in energy,[38] reacts readily with H_2 to form OH at very low collision energies, so small amounts of $O(^1D)$ in the oxygen atom beam would overshadow OH products from $O(^3P)$. The $O(^1D)$ reaction is exothermic (~41 kcal mol^{-1}) and barrierless,[39] and therefore the reaction cross sections are much larger than the analogous $O(^3P)$ reaction.[34,40] This stark difference in the reactivity of $O(^3P)$ and $O(^1D)$ is utilized in characterizing the electronic state composition of oxygen atoms produced from the laser detonation source discussed in Chapter 3.

Oxygen Atom Reactions with Alkanes

Much has been learned about $O(^3P)$ reactions with alkanes because of their relevance in combustion and atmospheric chemistry. Dynamical studies of oxygen atom reactions with various alkanes have shown that, at near thermal collision energies, an $O(^3P)$ atom typically reacts by abstracting a hydrogen atom to form an OH radical product, similar to the $O(^3P)$ + H_2 reaction.[41-43] Barriers for this reaction range from 5.0 to 8.1 kcal mol^{-1},[44] depending on the type of hydrogen abstracted (primary, secondary, or tertiary). These barriers are also reduced as the size of the hydrocarbon increases. Lower barriers coupled with larger reduced masses make these experiments more accessible to observe experimentally than the $O(^3P)$ + H_2 reaction. Several studies have been performed examining the kinetics and dynamics of hydrogen atom abstraction from various alkanes by $O(^3P)$, including theoretical calculation and experimental determination of reaction rates and vibrational and rotational distributions of the OH product.[41-47] A review of the hydrogen abstraction reaction by $O(^3P)$ from hydrocarbons was recently published by McKendrick *et al.*[45] All of these studies utilized fairly low collision energies conditions.

While it is well established that OH formation is the major channel in the reaction of alkanes with $O(^3P)$ at low collision energies, products, product energy, and angular distributions for reactions at collision energies representative of spacecraft-environment interactions have yet to be examined. It is easy to envision never before seen reaction channels when an oxygen atom reacts with alkanes at high c.m. collision energy, such as hydrogen atom elimination and possibly carbon-carbon bond breakage (in larger alkanes), if the collision energy is above the barriers for these processes. Prior to the work described in this thesis, only one limited theoretical study had considered the high collision energy regime present in LEO: Massa and coworkers performed *ab initio* calculations on the $O(^3P)$ reaction with ethane to form OCH_3 and CH_3 radicals.[48] They found a transition state structure and an activation barrier to the C-C bond breaking mechanism of about 41 kcal mol^{-1}. This channel was the only one considered in their calculations, although several more pathways are energetically possible.

Initial Reactions of $O(^3P)$ with a Hydrocarbon Surface

While it may seem counter intuitive to study reactions of gas-phase alkanes to elucidate mechanisms occurring on a surface, gas-phase-like processes have been observed in collisions of oxygen atoms with a saturated hydrocarbon surface.[19,49,50] In these experiments, which probe only the initial steps of the erosion process, 115 kcal mol^{-1} oxygen atoms were directed at a liquid hydrocarbon surface.[49,50] Only volatile reaction products could be detected in this experiment, and two products were observed: OH, which is formed via hydrogen atom abstraction by an oxygen atom, reminiscent of the gas-phase $O(^3P)$ + alkane reaction, and H_2O, formed from further reaction of the OH radical with the surface. In the formation of the OH product, the oxygen atom is believed to collide with a surface fragment of finite mass in

a localized interaction, similar to the interaction between an oxygen atom and a gas-phase hydrocarbon species. In fact, the effective mass of the surface fragment with which the oxygen atoms collided was found to be about 44 amu, the same mass as a propane molecule. This gas-phase-like formation of OH was determined to be one of the important first steps in the erosion process.

The observation that gas-phase-like reactions are occurring on surfaces led to using gas-phase hydrocarbons as collision partners for the oxygen atoms in order to study the dynamics, instead of the hydrocarbon surface. Reducing the size of the hydrocarbon reaction partner from a liquid, such as used in the experiment discussed above, squalane ($C_{30}H_{62}$), to a gaseous hydrocarbon, for example propane (C_3H_8), should lead to analogous results for the initial reactive events. However, since the alkanes are already in the gas phase, all reaction products formed, including possible oxygen-containing hydrocarbon species, would be detectable using the methods available and their dynamics could be examined. The smaller alkanes serve as excellent model systems to understand the reactions that can occur at surfaces and in spacecraft plumes. Furthermore, unlike the surfaces, these model systems can be treated in depth with modern theoretical methods. Chapters 5 and 6 in this thesis represent the first exploration into the reaction dynamics of hyperthermal atomic oxygen with saturated hydrocarbons by considering the reaction of $O(^3P)$ with the simplest hydrocarbon, methane.

Experiment-Theory Coupling

In the experiments undertaken, theoretical calculations done exclusively by Prof. George Schatz, Dr. Diego Troya, Dr. Biswajit Maiti, and Ronald Pascual at Northwestern University (NU) were invaluable in interpreting the data obtained. For every experiment, calculations were performed by Schatz at various levels of theory to serve not only as an invaluable aid to experimental data interpretation, but to refine codes developed at NU. The ultimate goal in

both of these efforts is to understand how a hydrocarbon polymer erodes in LEO and be able to model it reliably. None of the theoretical calculations herein are to be interpreted as the work of the author.

References

1. K. S. W. Champion, A. E Cole and A. J. Kantor, "Standard and Reference Atmospheres," *Handbook of Geophysics and the Space Environment*, Ed. A. S. Jursa (United States Air Force, Air Force Geophysics Laboratory, 1985).

2. R. G. Roble, "Energetics of the Mesosphere and Thermosphere," *The Upper Mesosphere and Lower Thermosphere: A Review of Experiment and Theory*, Eds. R. M. Johnson and T. L. Killeen (American Geophysical Union, Washington, D.C., 1995) pp. 1-21.

3. J. T. Visentine, "Environmental Definition of the Earth's Neutral Atmosphere," *NASA/ SDIO Space Environmental Effects on Materials Workshop held in Hampton, VA, 28 June - 1 July 1988*, NASA Conference Publication 3035, Part 1, Eds. L.A. Teichman and B.A. Stein (NASA, Washington, D.C., 1989) pp. 179-195.

4. *Natural Orbital Environmental Guidelines for Use in Aerospace Vehicle Development*, Eds. B. J. Anderson and R. E. Smith, NASA Technical Memorandum 4527 (NASA, Washington, D.C., 1994).

5. D. B. Green, G. E. Caledonia, and T. D. Wilkerson, *J. Spacecraft Rockets* **22**, 321 (1988).

6. E. Murad, *J. Spacecraft Rockets* **33**, 131 (1996).

7. B. A. Banks, K. K. deGroh, S. L. Rutledge and F. J. DeFilippo, *Prediction of In-Space Durability of Protected Polymers Based on Ground Laboratory Thermal Energy Atomic Oxygen*, NASA Technical Memorandum 107209 (NASA, Washington, D.C., 1996).

8. L. K. English, *Mat. Eng.* August, 39 (1987).

9. D. E. Hunton, *Sci. Am.* 261, 92 (1989).

10. F. S. Simmons, *Rocket Exhaust Plume Phenomenology* (American Institute of Aeronautics and Astronautics, Inc., Reston, VA, 2000).

11. L. J. Leger and J. T. Visentine, *J. Spacecraft Rockets* **23**, 505 (1986).

12. L. J. Leger, *Oxygen Atom Reaction with Shuttle Materials at Orbital Altitudes*, NASA Technical Memorandum 58246 (NASA, Houston, TX, 1982).

13. L. E. Murr and W. H. Kinard, *Am. Sci.* **81**, 153 (1993).

14. A. F. Whitaker and B. Z. Jang, *J. Appl. Polymer Sci.* **48**, 1341 (1993).

15. D. E. Brinza, S. Y. Chung, T. K. Minton, and R. H. Liang, *Final Report on the NASA/ JPL Evaluation of Oxygen Interactions with Materials-3 (EOIM-3)*, NASA JPL Publication (NASA, Pasadena, CA, 1994).

16. G. E. Caledonia, "Infrared Radiation Produced in Ambient/Spacecraft-Emitted Gas Interactions Under LEO Condition," in *Proceedings of the 38th AIAA Aerospace Sciences Meeting & Exhibit held in Reno, NV, 10-13 January, 2000*, AIAA-00-0104 (AIAA, Reston, VA, 2000).

17. B. L. Upschulte and G. E. Caledonia, *J. Chem. Phys.* **96**, 2025 (1992).

18. L. S. Berstein, Y-H. Chiu, J. A. Gardner, A. L. Broadfoot, M. I. Lester, M. Tsiouris, R. A. Dressler, and E. Murad, *J. Phys. Chem. A*, 107, 10695 (2003).

19. T. K. Minton and D. J. Garton, "Dynamics of Atomic-Oxygen-Induced Polymer Degradation in Low Earth Orbit," in *Advance Series in Physical Chemistry: Chemical Dynamics in Extreme Environments*, ed. R. Dressler (World Scientific, Singapore, 2000).

20. G. Dixon-Lewis and D. J. Williams, *Comp. Chem. Kinet.* **17**, 1 (1977).

21. N. Cohen and K. R. Westberg, *J. Phys. Chem. Ref. Data* **12**, 531 (1983).

22. N. Presser and R. J. Gordon, *J. Chem. Phys.* **82**, 1291 (1985).

23. S. Javoy, V. Naudet, S. Abid, and C. E. Paillard, *Int. J. Chem. Kinet.* **32**, 686 (2000).

24. G. C. Light, *J. Chem. Phys.* **68**, 2831 (1978).

25. J. Han, X. Chen, and B. R. Weiner, *Chem. Phys. Lett.* **332**, 243 (2000).

26. R. E. Howard, A. D. McLean, and W. A. Lester, *J. Chem. Phys.* **71**, 2412 (1979).

27. S. P. Walch, T. H. Dunning, R. Raffenetti, and F. W. Bobrowitz, *J. Chem. Phys.* **72**, 406 (1980).

28. J. S. Wright, D. J. Donaldson, and R. J. Williams, *J. Chem. Phys.* **81**, 397 (1984).

29. T. H. Dunning, Jr., L. B. Harding, A. F. Wagner, G. C. Schatz, and J. M. Bowman, *Science* **240**, 453 (1988).

30. T. Joseph, D. G. Truhlar, and B. C. Garrett, *J. Chem. Phys.* **88**, 6982 (1988).

31. S. Rogers, D. Wang, A. Kuppermann, and S. P. Walch, *J. Chem. Phys.* **104**, 2308 (2000).

32. B. R. Johnson and N. W. Winter, *J. Chem. Phys.* **66**, 4116 (1977).

33. R. Schinke and W. A. Lester, **70**, 4893 (1979).

34. G. C. Schatz, *J. Chem. Phys.* **83**, 5677 (1985).

35. D. C. Chatfield, R. S. Friedman, G. C. Lynch, D. G. Truhlar, and D. W. Schwenke, *J. Chem. Phys.* **98**, 342 (1993).

36. B. C. Garrett, D. G. Truhlar, and G. C. Schatz, *J. Am. Chem. Soc.* **108**, 2876 (1986).

37. A. F. Wagner and J. M. Bowman, *J. Chem. Phys.* **86**, 1976 (1987).

38. M. W. Chase, Jr., C. A. Davies, J. R. Downey, Jr., D. J. Frurip, R. A. McDonald, and A. N. Syverud, *J. Phys. Chem. Ref. Data* **14** (Suppl. 1), 531 (1639).

39. G. C. Schatz, L. A. Pederson, and P. J. Kuntz, *Faraday Discuss.* **108**, 357 (1997).

40. D. J. Garton, T. K. Minton, B. Maiti, D. Troya, and G. C. Schatz, *J. Chem. Phys.* **118**, 1585 (2003).

41. P. Andresen and A. C. Luntz, *J. Chem. Phys.* **72**, 5842 (1980).

42. N. J. Dutton, I. W. Fletcher, and J. C. Whitehead, *Mol. Phys.* **52**, 475 (1984).

43. G. M. Sweeney, A. Watson, and K. G. McKendrick, *J. Chem. Phys.* **106**, 9172 (1997).

44. J. T. Herron, *J. Phys. Chem. Ref. Data* **17**, 967 (1988).

45. F. Ausfelder and K. G. McKendrick, *Prog. React. Kinet. Mech.* **25**, 299 (2000).

46. M. C. Lin, "Dynamics of Oxygen Atom Reactions," in *Advances in Chemical Physics: Potential Energy Surfaces*, Ed. K. P. Lawley (John Wiley & Sons, Ltd., Chichester, Great Britain, 1980) pp. 113-167.

47. X. Liu and A. G. Suits, "The Dynamics of Hydrogen Atom Abstraction From Polyatomic Molecules," in *New Directions in Reaction Dynamics*, Eds. K. Liu and X. Yang (World Scientific, Singapore) to be published.

48. A. Gindulyte, L. Massa, B. A. Banks, and S. K. Rutledge, *J. Phys. Chem. A* **104**, 9976 (2000).

49. D. J. Garton, T. K. Minton, M. Alagia, N. Balucani, P. Casavecchia, and G. G. Volpi, *Faraday Discuss.* **108**, 387 (1997).

50. J. Zhang, D. J. Garton, and T. K. Minton, *J. Chem. Phys.* **117**, 6239 (2002).

METHODS

Crossed Molecular Beams Experiments

Crossed molecular beams methods provide a means to study fundamental gas-phase reaction dynamics under single-collision conditions. Y. T. Lee was a pioneer of "universal detection" in crossed-beams scattering experiments,[1-3] and he demonstrated the power of the crossed-beams method in elucidating the details of bimolecular collision dynamics. In his approach, two atomic or molecular beams are crossed at 90°, and products that scatter from the intersection region are detected with a mass spectrometer detector. The detector uses electron-impact ionization, which allows detection of a wide variety of products (thus the term "universal detection").

The hyperthermal oxygen atom reaction dynamics described in this thesis utilized a third generation crossed molecular beams apparatus based on the Y. T. Lee design.[1] A schematic diagram of the apparatus is shown in Fig. 2.1. A pulsed beam containing hyperthermal atomic oxygen is crossed at right angles by a pulsed supersonic beam of pure hydrogen or methane. Products that scatter from the intersection region are detected with a mass spectrometer detector (which rotates in the plane defined by the two beams) as a function of scattering angle and arrival time in the detector. Once ionized by the Brink-type electron-impact ionizer,[4] the products are mass selected with a quadrupole mass filter and counted with the use of a Daly-type ion counter.[5] The signal levels are always low enough that the detector is operated in a pulse counting mode, where electrical pulses resulting from individual ions emerge from the Daly ion counter and are accumulated as a function of their arrival time by a multichannel scaler. The ion flight time from the electron-impact ionizer to the Daly ion counter is proportional to the square root of the mass-to-charge ratio of the ion, and the

proportionality constant is determined empirically. Determination of the arrival time of neutral products at the electron-impact ionizer requires subtraction of the ion flight time from the time when ion counts are registered on the multichannel scaler. The number of ions generated in the electron-impact ionizer is dependent on the number density of neutral species present. Therefore, at a particular detector angle and mass-to-charge ratio, the mass spectrometer detector measures number density distributions as a function of arrival time, $N(t)$. These distributions are commonly referred to as time-of-flight (TOF) distributions. Integrated TOF distributions as a function of detector angle are called "laboratory angular distributions" and

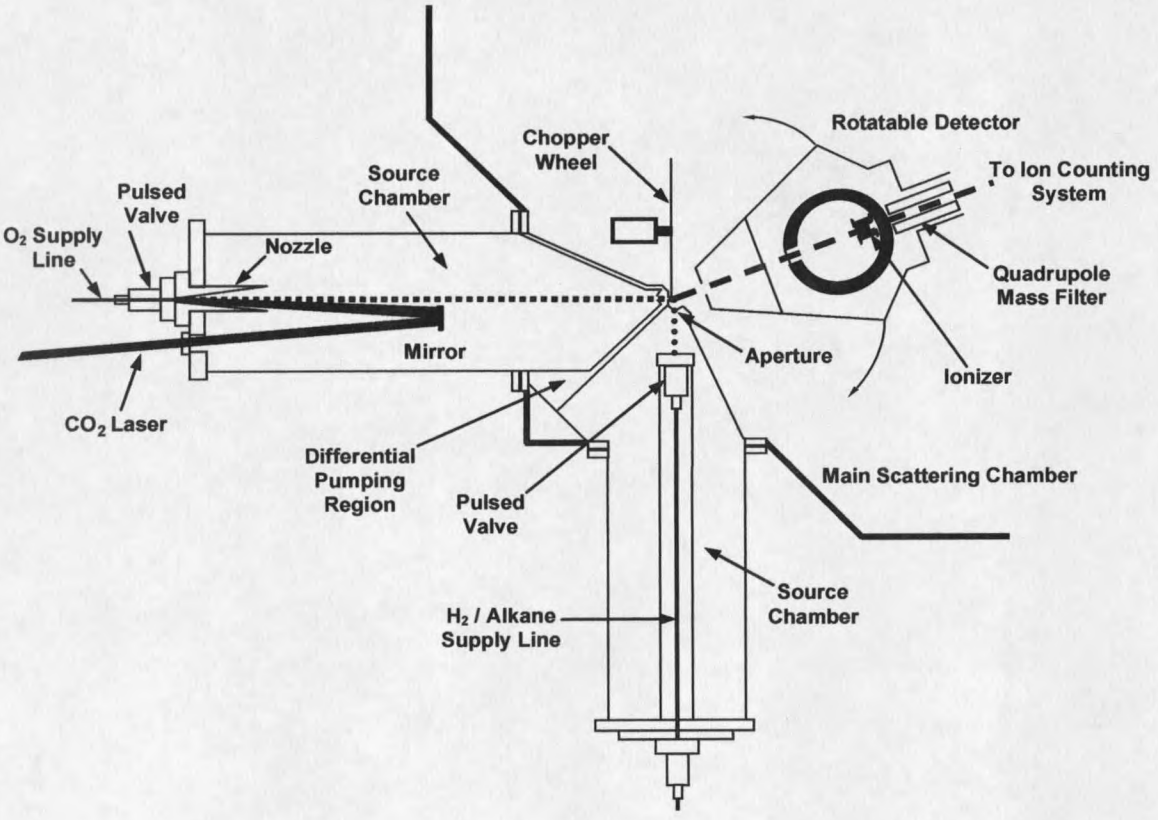

Figure 2.1. Schematic diagram of the crossed molecular beams apparatus at Montana State University. Components of the illustrated apparatus include the laser-detonation hyperthermal beam source, pulsed supersonic H_2/alkane source, differential pumping region, main scattering chamber, and rotatable mass spectrometer detector.

are given the designation $N(\Theta)$, where Θ is the angular direction of the scattered products with respect to the direction of the oxygen-atom beam. (The oxygen-atom beam direction is taken to be a laboratory angle of zero, and the positive angular direction is defined by a rotation from the oxygen-atom beam toward the hydrogen/alkane beam.) The primary data, then, are $N(t)$ and $N(\Theta)$ distributions of mass-selected products. In addition to detecting scattered products, the mass spectrometer detector is used to interrogate the atomic/molecular beams by aligning the detector such that the beam may enter it directly.

Beam Sources

Laser Detonation Source of Hyperthermal Atomic Oxygen

A unique and critical part of the research described herein is the laser detonation source (based on the source invented by Physical Sciences, Incorporated[6,7]), which provides a pulsed beam containing high velocity (6-9 km s^{-1}) oxygen atoms. The key elements of this source are a pulsed piezoelectric molecular beam valve,[8] a gold-plated, water-cooled copper nozzle, and a high energy (~7 J $pulse^{-1}$) CO_2 TEA laser. The pulsed valve introduces a high pressure (250 psig) surge (approximately 100 μs long) of pure O_2 gas into the conical nozzle through a 1 mm diameter × 250 mm long cylindrical channel at the apex of the cone. As the gas begins to expand into the nozzle, the CO_2 laser is fired, and the laser light passes through an antireflection-coated ZnSe window into the source chamber where it is then focused into the nozzle with the use of a bare gold mirror of 1 m radius of curvature. The beam waist of the laser is at the apex of the conical nozzle, but as the beam shape is roughly 4 × 4 mm at the waist, the laser light mainly impinges on the sides of the gold-coated cone and is reflected down into the orifice channel. The concentrated laser pulse initiates a breakdown of the gas and heats the resulting plasma to more than 20,000 K. The high-temperature, high-density

plasma expands rapidly into the 10 cm long, 20° included angle cone following detonation and engulfs the remaining cold gas. The local densities in the nozzle are sufficient to allow for efficient electron-ion recombination, but by the time the majority of the atoms formed in the plasma have cooled enough to recombine, the termolecular collision rate has dropped so low that the atomic species are, in effect, frozen in the emerging beam. Nevertheless, some atoms do recombine before the beam emerges from the nozzle, and the resulting beam thus contains both atomic and molecular oxygen. The ratio of atomic to molecular oxygen is variable depending on various source operating conditions, but the typical atomic fraction is about 70 percent. There is a small ionic component (<<1%), but any residual ions in the experiments described herein were deflected in a magnetic field produced by permanent magnets mounted on the source chamber roughly 50 cm downstream from the nozzle. The laser detonation source is generally operated at a repetition rate of 2 Hz, which is the practical limit allowed by the pumping speed of the source chamber. The pressure in the source chamber rises to ~1 mTorr during the gas pulse.

The hyperthermal beam is first collimated with the use of a 1 cm diameter aperture located 80 cm from the apex of the conical nozzle, and then the beam passes through a region of differential pumping (operating pressure ~10^{-6} Torr) and exits this region through a 3 mm diameter skimmer positioned ~95 cm from the apex of the nozzle. (In one experiment on the $O + D_2$ reaction, a smaller, 1.2 mm diameter, skimmer was used.) The hyperthermal beam reached the interaction region (the center of rotation of the detector) 99 cm from the nozzle apex, where it was only negligibly larger than the diameter of the previous skimmer. The operating pressure in the main scattering chamber was ~2×10^{-7} Torr.

The temporal profile of the atomic oxygen component of the overall hyperthermal beam pulse is seen in Fig. 2.2. The dashed line shows the TOF distribution of atomic oxygen, detected at $m/z = 16$. "Time zero" in this figure is the time at which the CO_2 laser fires, which

is the point in time when the oxygen atoms are created. The ion flight time has been subtracted, so the observed time is the time required for oxygen atoms to travel 132.7 cm from the apex of the nozzle cone to the electron-impact ionizer. As can be seen by the dashed curve in Fig. 2.2, the overall oxygen-atom pulse is very broad. In order to narrow the time (and velocity) width of the oxygen-atom beam pulse, a synchronized chopper wheel is typically used to select only a small portion of the overall beam pulse. This chopper wheel was placed just past the second aperture, in the main scattering chamber. The rotation rate of the chopper wheel was either 270, 300, or 400 Hz for these experiments. Two chopper wheels were used in the experiments, an older chopper wheel with four slots, having a maximum frequency of 270 Hz, and a newer chopper wheel which had three slots, each 1.5 mm wide, currently having a maximum frequency of 400 Hz. Care was taken to fabricate a new chopper wheel that could run stably for an entire day or more, with only a ±200 ns variation in its period. The solid curve in Fig. 2.2 shows the narrowed O-atom beam pulse that was selected with the new synchronized chopper wheel operating at 400 Hz and a final skimmer of 3 mm diameter. Besides defining a narrow oxygen-atom beam pulse, the chopper wheel adds the advantage of blocking all the light from the plasma when the hyperthermal beam was formed.

Supersonic Beam of Hydrogen and Alkanes

A piezoelectric pulsed valve, of the same type as that used for the oxygen-atom source, was used to produce pure beams of molecules (H_2, D_2, CH_4, and CD_4) that served as collision partners for the hyperthermal atomic oxygen. The nozzle orifice diameter was 1 mm, and the pressure behind the orifice was varied from 23 to 80 psig, depending on the gas. Two configurations for the H_2/alkane source were used in the current experiments. In one configuration, a differential pumping region was used between the source chamber and main scattering chamber. In the other configuration, the differential pumping region was removed.

The H_2/alkane beam exited the source chamber (or differential region) through a 1.2 mm diameter skimmer (no differential region) or a 2.5 mm diameter aperture (differential region) located roughly 3 cm from the crossing point of the two beams (interaction region). When the differential region was used, a 5 mm aperture was used between the source and differential chambers, and the distance between this aperture and the second aperture was 2 cm. The distance between the nozzle and first aperture was variable, and for each experiment this distance was set to give optimum scattered signal. Depending on the experiment, various pulse widths were used for the H_2/alkane beam (100 - 650 μs), but in all cases, the duration of the interaction of this beam with the oxygen-atom beam was determined by the temporal width of the oxygen-atom beam, which was less than 15 μs wide (full width at half maximum) at the interaction region. The velocities of the hydrogen and alkane beams were estimated with the use of the formula:[9]

$$\mathbf{v} = \sqrt{\frac{2k_B T}{m}\left(\frac{\gamma}{\gamma - 1}\right)},$$

where $\gamma = C_p/C_v$, T is the nozzle temperature, and m is the mass of the species in the neat beam. The velocity of this beam is probably only accurate to ±10%, but the errors caused by the uncertainty in the H_2/alkane beam velocities are negligible compared to the uncertainties caused by the hyperthermal oxygen-atom beam, which has a nominal velocity that is nearly one order of magnitude larger than and a velocity spread that is almost as large as that of the H_2/alkane beam.

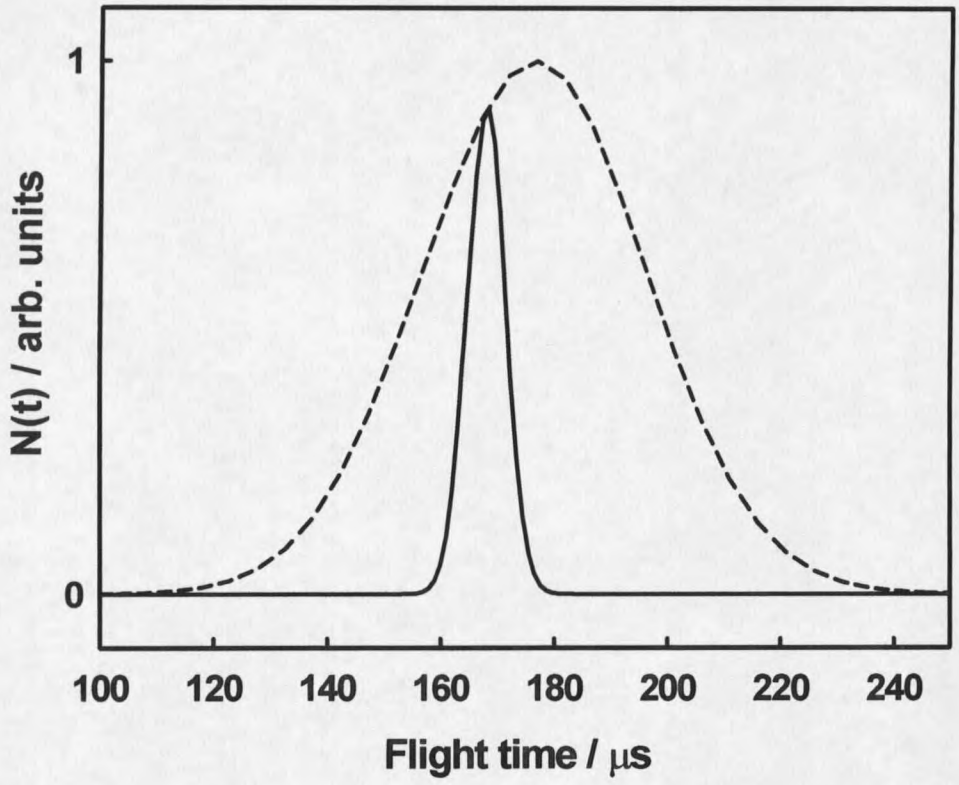

Figure 2.2. Representative oxygen-atom beam time-of-flight distributions. The overall beam distribution (dashed line) was narrowed in all of the experiments with the use of a synchronized chopper wheel. Using a 400 Hz chopper wheel, the beam distribution was narrowed significantly (solid line) and the beam velocity was tunable.

Experiment Timing

Timing is particularly important in pulsed crossed-beams experiments, because the two beam pulses must reach the interaction region at the same time in order for reaction between the two reactant beams to occur. The laser detonation source and associated synchronized chopper wheel impose additional complexity to the timing of the experiments. A timing diagram is shown in Fig. 2.3. The chopper wheel spins at a constant rate and produces a train of pulses as the slots in the chopper wheel pass over an LED/photodiode arrangement. The repetition rate of the experiment is determined by a 2 Hz reference oscillator. The train of

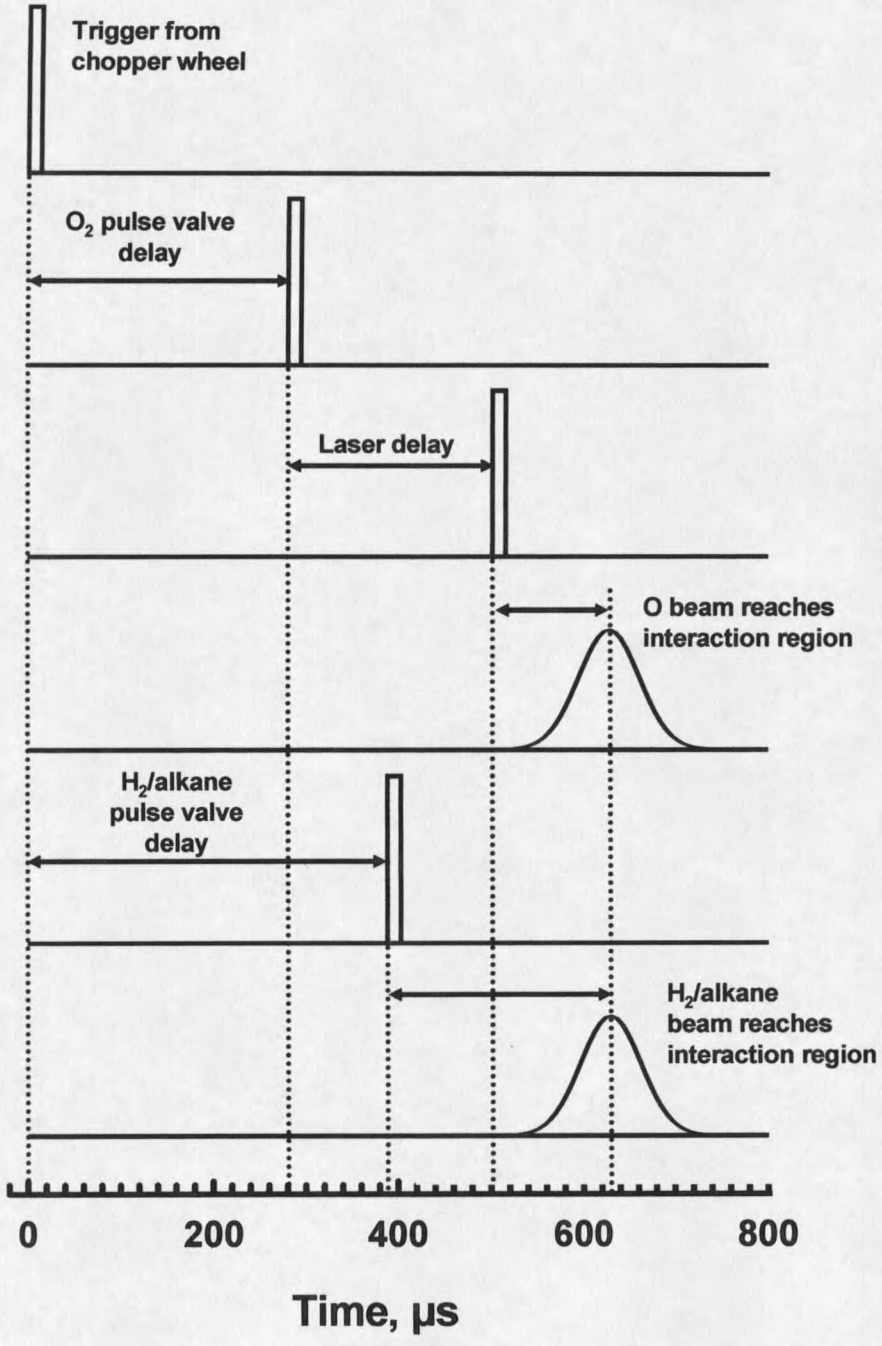

Figure 2.3. Example timing diagram used in the experiments. The timing is set by a chopper wheel placed in front of the oxygen atom beam. All delays are adjusted for each set of experiments.

chopper wheel (photodiode) pulses and the 2 Hz reference pulses are put into a timing circuit that allows the next photodiode pulse following a reference pulse to be output to a digital delay generator. Thus, while the repetition rate is controlled by the 2 Hz reference pulses, the actual experiment timing is controlled by the chopper wheel. The two pulsed valves are triggered at variable, independent delays after the photodiode pulse is received by the delay generator. These delays are labeled in Fig. 2.3 as "O_2 pulsed valve delay" and "H_2/alkane pulsed valve delay." After the O_2 valve is opened, there is a delay of about 200 - 230 μs before the CO_2 laser is fired. The delay generator also controls this "Laser delay." The remaining delays are determined by the flight times of the beam pulses to the interaction region. The laser delay is adjusted to provide the desired nominal oxygen-atom beam velocity. The O_2 pulsed valve delay is adjusted to select the desired portion of the overall oxygen-atom beam pulse with the chopper wheel. And the H_2/alkane pulsed valve delay is adjusted to yield the maximum scattered product signal.

The multichannel scaler is typically triggered by the same pulse that triggers the opening of the O_2 pulsed valve; therefore, measured TOF distributions include the laser delay, the flight time of the oxygen-atom beam pulse to the interaction region, the flight time of neutral products to the electron-impact ionizer, and the ion flight time from the ionizer to the Daly ion counter. The ion flight time is given by $\alpha(m/z)^{1/2}$, where α, which typically has a value of ~2.5, is a parameter that is determined by comparing the raw arrival times of the O and O_2 components of the hyperthermal beam. Because the chopper wheel selects only species in the hyperthermal beam that are traveling at a specific velocity, the difference in raw arrival times of O and O_2 comes from the difference in the ion flight times of O^+ and O_2^+. Thus the ion flight time parameter α is found from the measured difference in the O and O_2 arrival times and the difference in the square roots of the mass-to-charge ratios: $\alpha = \Delta t/\Delta(m/z)^{1/2}$. The flight time of the oxygen-atom pulse from the nozzle cone to the interaction region is

determined by measuring the velocity of the oxygen-atom beam and calculating the time for the beam pulse to travel the known 99 cm distance to the interaction region. The beam velocity is determined by measuring the oxygen-atom flight time – i.e., the time between when the CO_2 laser fires and the time when the beam pulse arrives at the ionizer (132.7 cm away). There is some uncertainty in this measurement, however, because the exact point of origin of the oxygen atoms is not extremely well defined and the pulse width of the laser may be as long as a few microseconds (sharp narrow peak followed by a slow tail). There is thus an estimated uncertainty in the measured flight times of approximately 2 μs. In order to conduct the analysis of the scattered products, their TOF distributions must be corrected such that they reflect the number density distributions of products arriving at the ionizer as a function of flight time from the interaction region. The correction is accomplished by subtracting from the raw TOF distributions: the ion flight time, the oxygen-atom flight time from the nozzle to the interaction region, and the laser delay.

Center-of-Mass to Laboratory Transformation

Both the TOF distributions, $N(t)$, at a fixed angle and the integrated TOF distributions as a function of angle, $N(\Theta)$, contain a wealth of information about the microscopic interactions between the species in the two crossed beams. The measured quantities are number density distributions in the laboratory reference frame, but the relevant microscopic information comes from scattered flux in the center-of-mass (c.m.) reference frame. The two reference frames are different, because the c.m. of the two colliding species is moving in the laboratory frame. The relationship between the c.m. and laboratory velocities can be illustrated with a velocity vector diagram, usually known as a Newton diagram.[9-10] Newton diagrams corresponding to specific reactions studied are presented in the following chapters. While a Newton diagram aids in the determination of c.m. velocities and angles from known laboratory

velocities and angles, it does not provide a means to determine directly c.m translational energy and angular distributions from measured laboratory number density distributions. In fact, because of the complexity of the experiment, including beam velocity distributions, beam angular divergences, ionizer width, and various other apparatus effects, it is extremely difficult (essentially impossible) to deconvolute the measured distributions in order to derive c.m. quantities. Therefore, a "forward convolution" method is typically employed to derive c.m. quantities from the data. The general approach is to start with trial distributions in the c.m. frame and, taking into account apparatus effects, use a Jacobian coordinate transformation to calculate expected laboratory number density distributions and compare these results with the experimental data. In this method, which has been discussed in detail elsewhere,[11-13] the c.m. scattered flux per unit solid angle, $I_{cm}(E_T, \theta)$, is typically assumed to be separable into the product of two functions: a c.m. translational energy distribution, $P(E_T)$, and a c.m. angular distribution, $T(\theta)$, where E_T is the sum of the translational energy of both products which scatter following a collision in the c.m. frame and θ is the angle at which a product scatters in the c.m. frame (with respect to the relative velocity vector of approach of the two collision partners). Trial $P(E_T)$ and $T(\theta)$ distributions are used to calculate TOF distributions with the relationship (derived from a Jacobian transformation),

$$N(t,\Theta) \propto \frac{l^2}{u t^3} I(E_T, \theta) = \frac{l^2}{u t^3} P(E_T) T(\theta),$$

where l is the flight length, u is the product velocity in the c.m. frame, and t is the laboratory flight time. The calculated TOF distributions, which take into account apparatus effects, including the arrival time distribution of the oxygen atoms at the interaction region, are compared with the laboratory TOF and angular distributions, and the input $P(E_T)$ and $T(\theta)$ distributions are iteratively adjusted until optimum fits to all laboratory distributions are obtained. Uncertainties in the derived $P(E_T)$ and $T(\theta)$ distributions are determined by observing

the maximum variation in these distributions that can still produce reasonable calculated fits. In order to allow for easy manipulation of the $P(E_T)$ and $T(\theta)$ distributions, parametrized functions are commonly used. For the current analysis, the $P(E_T)$ distribution was typically based on the versatile RRK form:[12]

$$P(E_T) = (E_T - B)^p (E_{avail} - E_T)^q ,$$

where E_{avail} is the total energy available for translation in the c.m. frame. Thus, E_{avail} is equal to the sum of the c.m. collision energy, E_{coll}, and the reaction energy, ΔE_r. B, p, and q are adjustable parameters that affect the width and the position of the energy maximum in the distribution. An eleven-term Legendre polynomial function, with adjustable weighting of each of the polynomial terms, was used to describe the $T(\theta)$ distribution. The Legendre polynomials can be obtained using Rodrigues' formula:

$$T_k(\theta) = \frac{a_k}{2^k k!} \frac{d^k}{d(\cos(\theta))^k} (\cos^2(\theta) - 1)^k ,$$

where $k = 0, 1, 2,...,10$ (for the 11 total polynomial terms used) and a_k are the coefficients used to adjust the weighting of the terms. By summing over all of the terms, the $T(\theta)$ distribution is obtained.

Once an acceptable fit to the experimental data from the forward convolution simulation is achieved, the $T(\theta)$ and $P(E_T)$ distributions from the forward convolution simulation of the data can be used to create the final outcome of the reactive scattering experiment, the c.m. velocity-flux contour map or differential cross section. This contour map is a plot of the scattered intensity as a function of angle and velocity in the c.m. frame and can be viewed as an image of the reaction.

The computer program used to carry out the center-of-mass to laboratory transformation is the MSU XBEAM Program, Version 2.2, which is derived from the CMLAB program that was originally developed at UC Berkeley in the 1970's and later modified to the GMTHRASH version in the late 1980's and early 1990's. The previous programs were written for crossed beams experiments with continuous beams, so the MSU XBEAM version required significant modification to account for the crossing of pulsed beams,[14] where one of the beams (the oxygen-atom beam) has a distribution of incident times at the interaction region and the atoms arriving at different times have different velocities.

Experimental Resolution

The crossed-beams method used for these experiments is subject to severe limitations in velocity resolution. The product velocity in the laboratory frame is the vectorial sum of the velocity of the center of mass of the two colliding species (in the laboratory frame) and the velocity of the reaction product in the c.m. frame. Because the velocity of the center of mass is high (on the order of 4 km s^{-1}), the product velocities are therefore also high. The product velocities are determined by measuring the product flight time over a 33.7 cm distance. Thus, typical flight times are in the range of 40 - 50 μs. As mentioned previously, there could easily be a 2 μs error in the measurement of the flight time, which would create an error in the laboratory velocity of roughly 400 m s^{-1}, or 5 percent. A compounding source of error is the c.m. velocity, which is only as accurate as the beam velocities. Therefore, the error in the measured laboratory velocities could be as much as 10 percent, which could result in uncertainties in translational energies that are more than 20 percent. Much care must be taken in order to minimize timing errors, because even such a small measurement error of one microsecond can have a large effect on translational energy distributions that are derived from the experiments.

In addition to the uncertainties imparted by the high product velocities, the temporal width of the incident oxygen-atom beam also inhibits velocity resolution and thus the ultimate precision of the derived translational energy distributions. Even with the use of the 400 Hz chopper wheel, the base width of the incident oxygen-atom beam pulse (measured at the detector) was 25 μs, which means that the base width of the product TOF distributions will be at least this much, even if the product translational energy distribution is extremely narrow. The width of the arrival time of the incident beam is accounted for in the analysis, as is the fact that different arrival times correspond to different beam velocities and thus different collision energies. However, when the width of the arrival time distribution accounts for a significant amount of broadening of the product signal, then the energy width of the trial $P(E_T)$ distribution may be varied by many kcal mol^{-1} and have no effect on the calculated TOF distributions. Thus, it becomes difficult to derive a unique $P(E_T)$ distribution. Furthermore, the analysis assumes that over the range of c.m. collision energies resulting from the velocity spread in the oxygen-atom beam, the shape of the $P(E_T)$ distribution of the products will remain constant. This approximation breaks down if the $P(E_T)$ distribution is strongly dependent on collision energy. So, the $P(E_T)$ distribution that is derived represents a sort of average distribution over the range of collision energies in the experiment. In the experiments reported here, it is believed that the width of the arrival time distribution of the incident oxygen-atom beam results in more uncertainty in the derived $P(E_T)$ distributions than does the range of c.m. collision energies.

It is possible to narrow the temporal width of the oxygen-atom beam pulse even further by (1) spinning the chopper wheel faster, (2) reducing the width of the slots in the chopper wheel, or (3) reducing the diameter of the beam as it passes through the chopper wheel. Unfortunately, all of these approaches reduces the beam intensity and thus the signal in the experiment. For the relatively high signal experiment on the reaction of oxygen atoms with

D_2 (see Chapter 4), the diameter of the beam was narrowed in order to improve the time resolution of the experiment. But in all the other experiments reported in this thesis, an improvement in the resolution would have lowered the signals to the point of making the experiments effectively impossible. The choice of chopper slot width and wheel speed was investigated, and it was found more effective to use a wider slot and spin the wheel faster than to use a narrower slot and spin the wheel slower. A possible reason for this observation is that the incident oxygen-atom beam pulse produces a localized pressure increase in the vicinity of a narrow slot, which leads to multiple collisions and a consequent attenuation of the pulse that makes it through the slot. The local pressure does not build up to this extent if the slot width is wider. Another possibility is that scattering from the edges of the slot, again leading to multiple collisions and beam attenuation, is more important for narrower slots than for wider slots. A slot width of 1.5 mm and wheel speed of 400 Hz appeared to be a good compromise, but it was a significant challenge to have a chopper wheel built that could operate very stably in vacuum at this high frequency.

Given the inherent uncertainties associated with the methods employed in the experiments discussed herein, a question arises as to why this method was used instead of another crossed-beams approach, such as velocity map imaging of laser-ionized products.[15-16] Velocity map imaging essentially allows detection of products in the c.m. frame, so the velocity resolution is not so limited by very high laboratory velocities. Moreover, there is the possibility with velocity map imaging to not only identify c.m. angular and translational energy distributions but also internal state distributions of products. The disadvantage of velocity map imaging and other techniques that rely on photon-based detection [single photon ionization, resonance-enhance multiphoton ionization (REMPI), or laser-induced fluorescence (LIF)] is that either the products must be small so the spectroscopy is known (REMPI, LIF) or the light source must be in the vacuum ultraviolet (single-photon ionization). On the other hand, electron-

impact ionization detection is generally applicable to any products that may be formed in a reaction. Ideally, a laboratory for the study of reaction dynamics would have capabilities to conduct both "survey" crossed-beams studies with a rotatable mass spectrometer (or rotatable source and fixed mass spectrometer detector) and velocity map imaging with single-photon ionization for the ultimate in detailed and accurate information. But having both these complementary capabilities would require substantial resources not currently available. And given the fact that the experiments described in this thesis are the first of their kind ever to be performed, it was reasonable to take the approach of universal detection in order to gain the most global knowledge about these heretofore unstudied hyperthermal O-atom reactions.

References

1. Y. T. Lee, J. D. McDonald, P. R. LeBreton, and D. R. Herschbach, *Rev. Sci. Instrum.* **40**, 1402 (1969).

2. Y. T. Lee, J. D. McDonald, P. R. LeBreton, and D. R. Herschbach, *J. Chem. Phys.* **49**, 2247 (1968).

3. Y. T. Lee, J. D. McDonald, P. R. LeBreton, and D. R. Herschbach, *J. Chem. Phys.* **51**, 455 (1969).

4. G. O. Brink, *Rev. Sci. Instrum.* **37**, 857 (1966).

5. N. R. Daly, *Rev. Sci. Instrum.* **31**, 264 (1960).

6. G. E. Caledonia, R. H. Krech, and B. D. Green, *AIAA J.* **25**, 59 (1987).

7. G. E. Caledonia, R. H. Krech, B. D. Green, and A. N. Pirri, *Source of High Flux Energetic Atoms*, Physical Sciences, Inc., US Patent No. 4894511, 1990.

8. D. Proch and T. Trickl, *Rev. Sci. Instrum.* **60**, 713 (1989).

9. J. I. Steinfeld, J. S. Francisco, and W. L. Hase, *Chemical Kinetics and Dynamics, 2nd Ed.* (Prentice Hall, New Jersey, 1999).

10. P. Houston, *Chemical Kinetics and Reaction Dynamics* (McGraw Hill, Boston, 2001).

11. *Atomic and Molecular Beam Methods*, Vol. 1, edited by G. Scoles (Oxford University Press, New York, 1988).

12. R. J. Buss, Ph. D. Thesis, University of California, Berekely (1979).

13. X. Zhao, Ph. D. Thesis, University of California, Berkeley (1988).

14. J. Zhang, Ph. D. Theisis, Montana State University, Bozeman (2001).

15. D. Townsend, M. P. Minitti, and A. G. Suits, *Rev. Sci. Instrum.* **74**, 2530 (2003).

16. X. Liu, R. L. Gross, G. E. Hall, J. T. Muckerman, and A. G. Suits, *J. Chem. Phys.* **117**, 7947 (2002).

EXCITATION FUNCTION FOR THE $O(^3P) + H_2 \rightarrow OH + H$ REACTION: CHARACTERIZATION OF THE OXYGEN ATOM ELECTRONIC STATE IN THE HYPERTHERMAL BEAM

Introduction

The reaction, $O(^3P) + H_2 \rightarrow OH + H$, is of fundamental significance in chemistry, as it is the simplest reaction involving oxygen atoms, one of the key reactions in the combustion of hydrogen and hydrocarbons, and a prototype for hydrogen-atom abstraction reactions. While the reaction has been the subject of numerous investigations beginning in the 1960's, including experimental kinetics studies of rate constants and isotope effects,[1-5] state resolved reaction rates,[6-7] theoretical studies of potential energy surfaces,[8-13] classical trajectory,[14-17] quantum dynamics,[18-23] and transition state theory calculations,[24-27] it has never been studied by molecular beams methods. The reason for this is the high barrier to reaction, 9 kcal mol^{-1}, and small reduced mass, requiring high beam velocities in order to reach sufficient center-of-mass (c.m.) collision energy for the reaction to occur. Additionally, this reaction has very unfavorable kinematics for studying the dynamics experimentally. Figure 3.1 shows a Newton diagram for the reaction, $O(^3P) + H_2 \rightarrow OH + H$, in which the oxygen atom beam velocity is 7900 m s^{-1} and the H_2 beam velocity is 2500 m s^{-1} (representative laboratory conditions). The OH Newton circle is very small and covers a less than 10° range of laboratory angles. Taking into account that the detector viewing angle is ~2°, it is very difficult to obtain angular dependencies of the scattered OH product. Additionally, the small size of the Newton circle inhibits resolution of the forward and backward components of the scattered OH product.

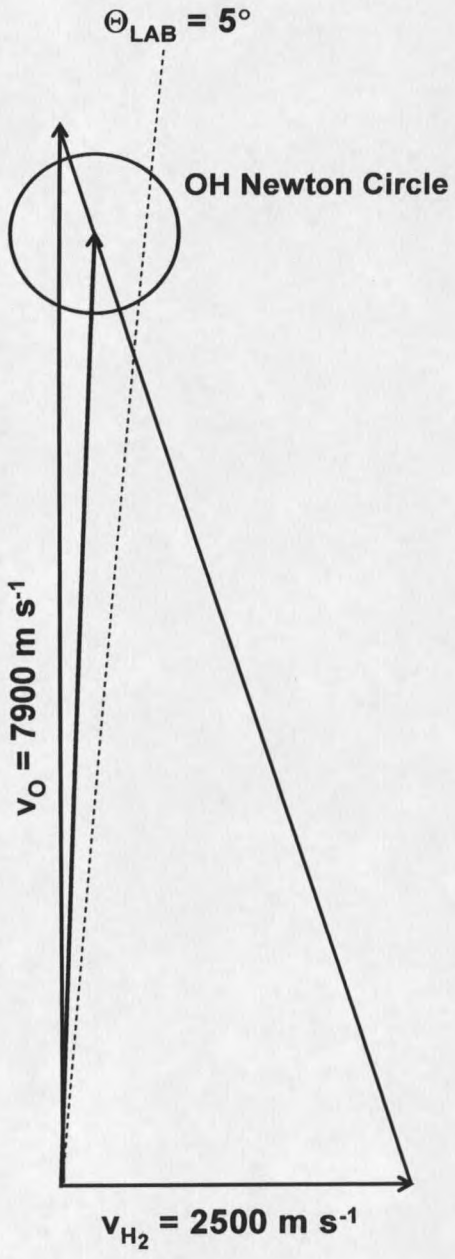

Figure 3.1. Newton diagram for the OH + H channel of the O(^3P) + H_2 reaction at E_{coll} = 15 kcal mol^{-1}. The circle represents the maximum recoil velocity of the OH product given the energy available for reaction, which is the collision energy minus the endoergicity of the reaction.

Despite these unfavorable conditions for obtaining detailed dynamical information, the $O(^3P) + H_2$ reaction is ideal for obtaining a relative excitation function, proportional to reaction cross section as a function of collision energy. The small Newton circle becomes an asset when the primary experimental goal is an excitation function, because the OH flux is scattered over a small region so the detected flux at a fixed detector angle will be representative of the overall reactive product flux.

Although measuring the $O(^3P) + H_2$ excitation function seems experimentally plausible, any $O(^1D)$ in the oxygen-atom beam produced by the laser detonation source would significantly interfere. Since the cross section for the $O(^1D)$ reaction with H_2 is much higher than the $O(^3P)$ reaction in the region of the $O(^3P)$ reaction threshold,[20] OH formed from $O(^1D)$ in the beam would overshadow any OH formed from $O(^3P)$. It is therefore valuable to compare the experimental excitation function with the excitation function predicted by theoretical calculations on the $O(^3P) + H_2$ and $O(^1D) + H_2$ reactions. Very accurate potential energy surfaces (PESs) exist for these reactions, and dynamics calculations involving these PESs, such as excitation function calculations, should be very accurate representations of what will be seen experimentally. We can therefore investigate the possible role that $O(^1D)$ would play in measurements if it were present in an oxygen atom beam by comparing the measured excitation function for $O + H_2$ with calculated cross sections that are based on accurate PESs for both the $O(^3P)$ and $O(^1D)$ reactions with H_2.

Experimental Details

The experiment was performed with the use of the crossed molecular beams apparatus described in Chapter 2. A pulsed beam of hyperthermal oxygen atoms produced in the laser detonation source was crossed by a pulsed supersonic beam of neat H_2 having a nominal velocity of 2.5 km s^{-1}. The hyperthermal oxygen-atom beam pulse was narrowed with the

use of the older, four-slot synchronized velocity selector wheel rotating at 270 Hz. The synchronization between the chopper wheel and the overall beam pulse was varied in order to produce oxygen-atom beams with nominal velocities from 5920 to 10100 m s^{-1}, with velocity widths (FWHM) of 660 to 1800 m s^{-1}. Velocity distributions of the eight different chopped oxygen-atom beams used are shown in Fig. 3.2. The hyperthermal beam nominally consisted of about 70 percent oxygen atoms and 30 percent oxygen molecules, but the relative amounts of O and O_2 varied with the beam velocities; lower velocity beams contained larger fractions of O_2. TOF distributions of products scattered from the crossing region of the two beams were collected at a fixed detector angle of 5° with respect to the oxygen-atom beam, as shown in Fig. 3.1.

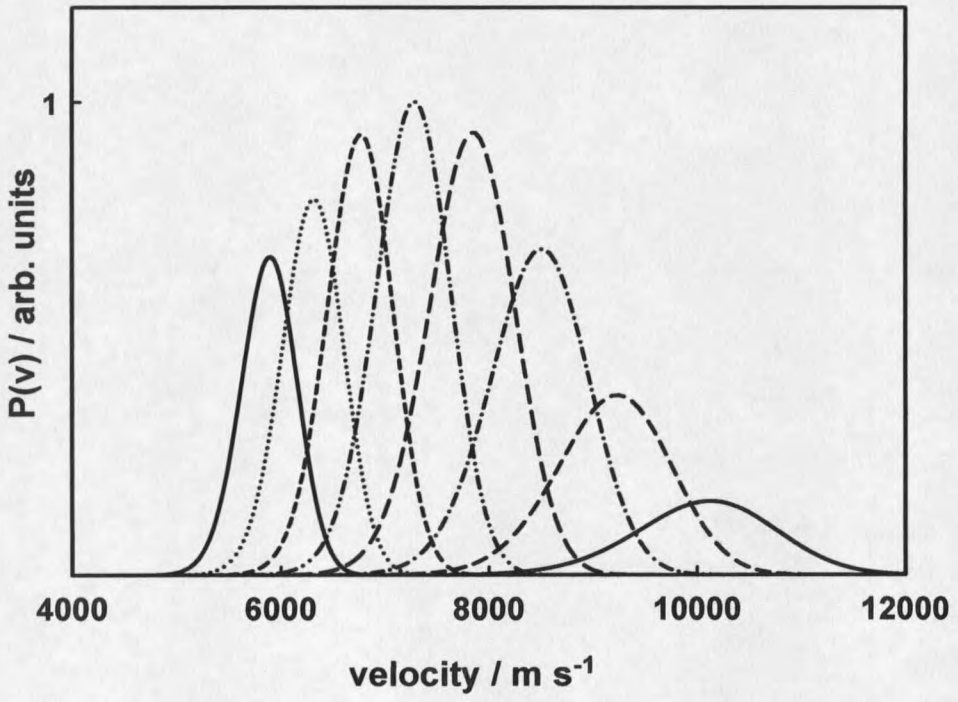

Figure 3.2. Oxygen-atom beam velocity distributions created from chopping the overall beam pulse with a velocity selector wheel rotating at 270 Hz. The synchronization between the chopper wheel and pulsed valve is varied to obtain distributions with different peak velocities.

Results and Analysis

Only inelastically scattered O and reactively scattered OH were detected. Figure 3.3 shows TOF distributions for both O and OH corresponding to eight different nominal center-of-mass (c.m.) collision energies, ranging from 8.8 to 23 kcal mol^{-1}. The signal intensities of the scattered products varied with c.m. collision energy primarily in proportion to the corresponding oxygen atom flux in the hyperthermal beam. In order to obtain the dependence of the scattered OH flux on collision energy, the integrated OH flux at a particular collision energy was divided by the integrated oxygen atom flux at that collision energy. The scattered flux, $I(t)$, is determined from the relationship, $I(t) \propto N(t)/t$, where $N(t)$ is the measured (relative) number density, and t is the flight time from the crossing region of the two beams to the ionizer of the mass spectrometer detector. The integrated flux is thus $\Sigma N(t)/t$. Because the c.m. velocities of scattered O and OH are small compared to the oxygen atom beam velocity, a large fraction of the scattered flux is detected at a single detector angle. Thus, the scattered OH flux as a function of c.m. collision energy should mirror the excitation function for the $O + H_2 \rightarrow OH + H$ reaction. The relative OH flux as a function of collision energy is shown as circles in Fig. 3.4. Within experimental error, the OH flux is zero for a c.m. collision energy of 8.8 kcal mol^{-1}, and the flux rises dramatically as the c.m. collision energy increases to 23 kcal mol^{-1}.

Discussion

Reactive scattering calculations were carried out by Schatz, *et al.* for the same reaction using the $^3A''$ and $^3A'$ analytical potential energy surfaces developed by Rogers *et al.*[13] Dynamics calculations were performed using quasiclassical trajectory (QCT) calculations as well as more accurate time dependent quantum mechanical (TDQM) wave packet methods.[28]

All calculations were done assuming no coupling between the two triplet surfaces, no coupling to any singlet states, and neglecting the 2 ^{3}A″ surface, which would only produce excited products. In order the understand and estimate the role of O(^1D) in the experiment, QCT calculations were performed on the 1 ^{1}A′ and 1 ^{1}A″ analytical potential energy surfaces developed by Dobbyn and Knowles.[29]

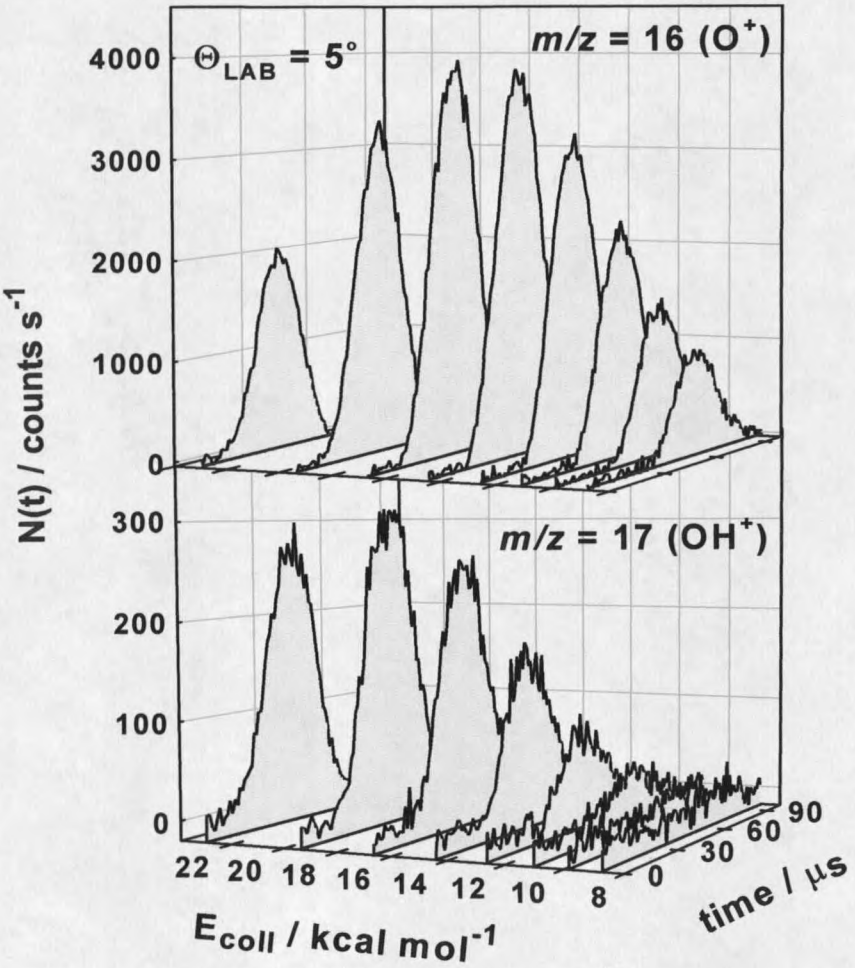

Figure 3.3. Time-of-flight (TOF) distributions of inelastically scattered O (top) and reactively scattered OH (bottom), collected with a detector angle of 5° with respect to the oxygen-atom beam. Eight TOF distributions were collected for both products, corresponding to eight different center-of-mass collision energies, E_{coll}. Time zero in these distributions corresponds to the nominal time at which the oxygen-atom beam pulse intersected the H_2 beam pulse.

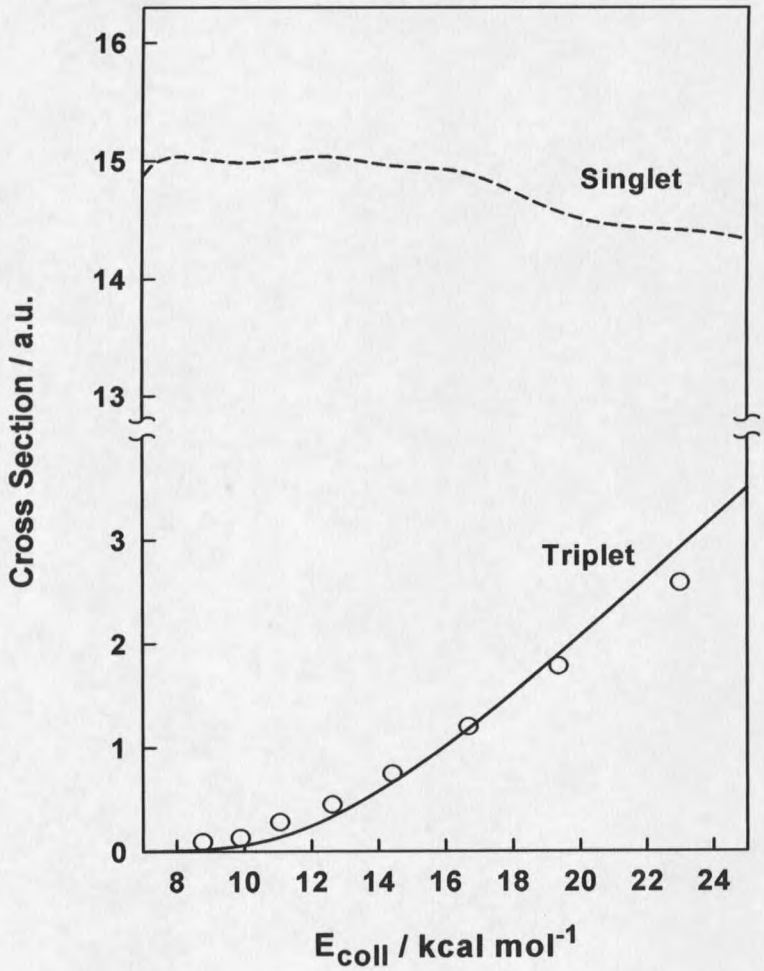

Figure 3.4. Predicted excitation curves (lines) for the $O + H_2$ reaction on singlet and triplet surfaces and experimental data points (circles) for the relative flux of scattered OH product. The predicted curves were determined by averaging the excitation functions shown in Fig. 3.5 [tiplet = ($^3A''$, TDQM + $^3A'$, TDQM)/3; singlet = ($^1A''$, QCT + $^1A'$, QCT)/5] and then convoluting the resulting triplet and singlet curves with the experimental center-of-mass collision energy distributions. Experimental error bars, estimated from the statistical counting errors, are comparable to the size of the circles used to represent the data points.

Figure 3.5 shows the excitation function calculated from the TDQM and QCT methods for both the singlet and triplet surfaces. These results show the threshold near 9 kcal mol^{-1} in the TDQM results for the triplet reaction, which is in stark contrast to the nearly flat singlet cross section (on average) over the same energy range. The QCT results are in good agreement

with the TDQM results for energies more than 2 kcal mol^{-1} above threshold, however close to threshold the TDQM calculations show evidence of tunneling. Results for the two triplet surfaces, which have the same barrier height, are very similar, but, the $^3A''$ surface has somewhat higher reactivity.

The predicted excitation curves for the two reactions, $O(^3P) + H_2$ and $O(^1D) + H_2$, determined by averaging the excitation functions shown in Fig. 3.5 according to the appropriate statistical weight [triplet = ($^3A''$, TDQM + $^3A'$, TDQM)/3; singlet = $^1A''$, QCT + $^1A'$, QCT)/ 5] and then convolving the resulting triplet and singlet curves with the experimental c.m. collision energy distribution, are shown in Fig, 3.4. The experimental OH fluxes, which represent a relative excitation function, have a striking similarity in their dependence on c.m. collision energy to that of the predicted excitation function for the $O(^3P) + H_2$ reaction. Furthermore, the experimental OH flux is zero (within experimental error) at the lowest collision energy of 8.8 kcal mol^{-1}, which is also consistent with reaction on a triplet surface. Given the nearly identical shapes of the experimental excitation function for the $O(^3P) + H_2$ reaction and the fact that the OH flux drops to zero below the predicted threshold for this reaction, we conclude that the dominant reactive species in the hyperthermal beam is $O(^3P)$. The predicted cross sections for the singlet and triplet surfaces and the uncertainty in our data allow us to estimate an upper limit of 1.0 percent for the fraction of $O(^1D)$ in the beam; however, this fraction might in fact be much lower.

Close inspection of the data suggests that the rise in experimental scattered OH flux with collision energy is slightly slower than the predicted rise. This difference is the expected result of the fixed detector angle of 5°. As the collision energy increases, the relative velocity of the O and H_2 increases, and the OH products scatter at higher velocities in the c.m. frame. Therefore, the fraction of products that can be detected at a given lab angle decreases slightly with increasing collision energy, which will tend to reduce effective detection sensitivity as

the collision energy increases. In addition, the fixed detector angle will lead to a slight detection bias toward more sideways c.m. angles as the collision energy increases. The OH product is predicted to be backward scattered (with respect to the c.m. direction of the incident oxygen atoms);[30] thus, a systematic sampling of ever more sideways c.m. angles, as the collision energy is increased, will slightly reduce the rise in measured OH flux from that which would be observed if the detected range of c.m. angles had remained constant. These two systematic errors have only a minor effect on the comparison with the predicted excitation function and no effect on the conclusion that we have observed unequivocal evidence of the $O(^3P) + H_2$ reaction.

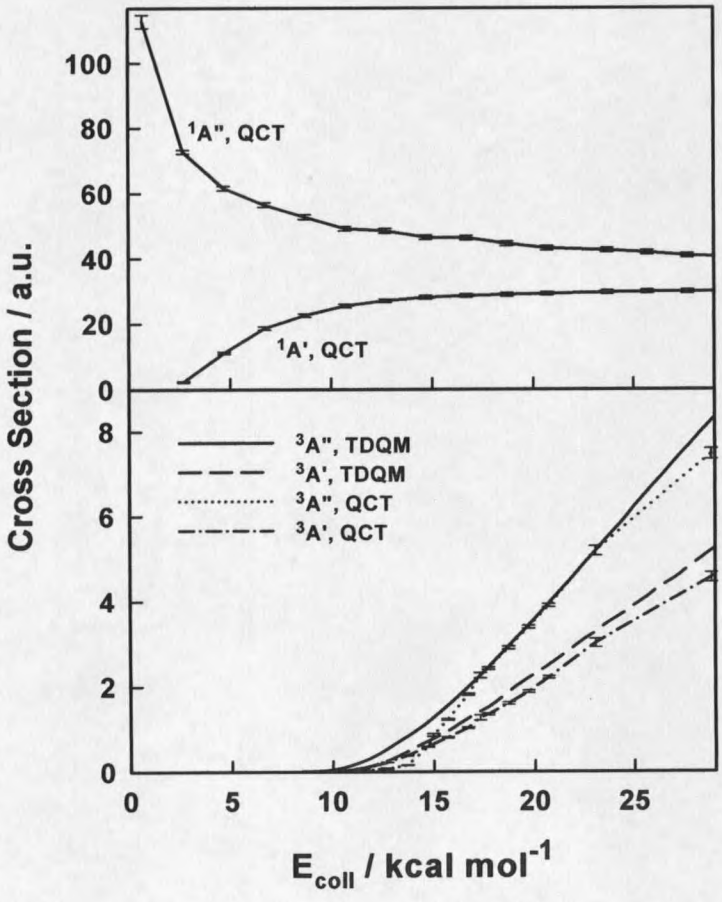

Figure 3.5. Calculated excitation functions from Schatz *et al.* for the $O(^3P) + H_2 \rightarrow OH + H$ reaction. (Top) QCT excitation functions for $O(^1D) + H_2 \rightarrow OH + H$. (Bottom) TDQM and QCT excitation functions for $O(^3P) + H_2 \rightarrow OH + H$.

Conclusion

The excitation function for the reaction, $O(^3P) + H_2 \rightarrow OH + H$, has been investigated with crossed molecular beams methods and has been compared to theoretical excitation functions obtained with accurate quantum wave packet calculations. The close match between experimental and predicted excitation functions leads to the conclusion that the detected OH signal is the result of $O(^3P)$ reacting with H_2. Further quasiclassical trajectory (QCT) calculations yield the excitation function for the reaction, $O(^1D) + H_2 \rightarrow OH + H$, and allow an upper limit of 1.0 percent to be placed on the fraction of O atoms in the beam that are in the excited $O(^1D)$ state. This result suggests that the laser detonation source, which has been used exclusively in this thesis and is often used for simulation of space environmental effects, may be used to create an environment in which the effect of hyperthermal oxygen atoms reflects interactions involving ground-state $O(^3P)$.

References

1. G. Dixon-Lewis and D. J. Williams, *Comp. Chem. Kinet.* **17**, 1 (1977).
2. N. Cohen and K. R. Westberg, *J. Phys. Chem. Ref. Data* **12**, 531 (1983).
3. N. Presser and R. J. Gordon, *J. Chem. Phys.* **82**, 1291 (1985).
4. H.-X. Yang, K. S. Shin, and W. Gardiner, *Chem. Phys. Lett.* **207**, 69 (1993).
5. S. Javoy, V. Naudet, S. Abid, and C. E. Paillard, *Int. J. Chem. Kinet.* **32**, 686 (2000).
6. G. C. Light, *J. Chem. Phys.* **68**, 2831 (1978).
7. J. Han, X. Chen, and B. R. Weiner, *Chem. Phys. Lett.* **332**, 243 (2000).
8. R. E. Howard, A. D. McLean and W. A. Lester, *J. Chem. Phys.* **71**, 2412 (1979).
9. S. P. Walch, T. H. Dunning, R. Raffenetti, and F. W. Bobrowicz, *J. Chem. Phys.* **72**, 406 (1980).
10. J. S. Wright, D. J. Donaldson, and R. J. Williams, *J. Chem. Phys.* **81**, 397 (1984).
11. T. H. Dunning, Jr., L. B. Harding, A. F. Wagner, G. C. Schatz, and J. M. Bowman, *Science* **240**, 453 (1988).
12. T. Joseph, D. G. Truhlar and B. C. Garrett, *J. Chem. Phys.* **88**, 6982 (1988).
13. Rogers, D. Wang, A. Kuppermann, and S. P. Walch, *J. Phys. Chem. A* **104**, 2308 (2000).
14. B. R. Johnson and N. W. Winter, *J. Chem. Phys.* **66**, 4116 (1977).
15. R. Schinke and W. A. Lester, *J. Chem. Phys.* **70**, 4893 (1979).
16. Z. B. Alfassi, and M. Baer, *Chem. Phys.* **63**, 275 (1981).
17. M. Braunstein, S. Adler-Golden, B. Maiti, and G. C. Schatz, *J. Chem. Phys.* **120**, 4316 (2004).
18. D. C. Clary and J. N. L. Connor, *Mol. Phys.* **41**, 689 (1980).

19. J. M. Bowman, and K. T. Lee, in *Potential Energy Surfaces and Dynamics Calculations*; ed. D. G. Truhlar (Plenum, New York, 1981) p. 359

20. G. C. Schatz, *J. Chem. Phys.* **83**, 5677 (1985).

21. K. Haug, D. W. Schwenke, D. G. Truhlar, Y. C. Zhang, J. Z. H. Zhang, and D. J. Kouri, J. *Chem. Phys.* **87**, 1892 (1987).

22. J. M. Bowman, *Chem. Phys. Lett.* **141**, 545 (1987).

23. D. C. Chatfield, R. S. Friedman, G. C. Lynch, D. G. Truhlar, and D. W. Schwenke, *J. Chem. Phys.* **98**, 342 (1993).

24. B. C. Garrett, D. G. Truhlar, R. S. Grev and A. W. Magnuson, *J. Phys. Chem.* **84**, 1730 (1980).

25. B. C. Garrett, and D. G. Truhlar, *Int. J. Quant. Chem.* **29**, 1463 (1986)

26. B. C. Garrett, D. G. Truhlar, and G. C. Schatz, *J. Am. Chem. Soc.* **108**, 2876 (1986).

27. A. F. Wagner and J. M. Bowman, *J. Chem. Phys.* **86**, 1976 (1987).

28. N. Balakrishnan, C. Kalyanaraman, and N. Sathyamurthy, *Phys. Rep.* **280**, 79 (1997); J. Z. H. Zhang, *Theory and Application of Quantum Molecular Dynamics* (World Scientific, Singapore, 1999).

29. A. J. Dobbyn and P. J. Knowles, *Mol. Phys.* **91**, 1107 (1997).

30. R. Schinke and W. A. Lester, Jr., *J. Chem. Phys.* **70**, 4893 (1979).

INELASTIC AND REACTIVE SCATTERING DYNAMICS OF $O(^3P) + D_2$

Introduction

In the previous chapter, the experimental excitation function for the reaction, $O(^3P) + H_2 \rightarrow OH + H$, was measured and compared to very accurate quantum reactive scattering calculations. Two important results emerged from the excitation function study: (1) no intersystem crossing was observed in the reaction of $O(^3P)$ with H_2 at the collision energies under investigation, and (2) less than one percent of the oxygen atoms in the beam produced via laser detonation were in the excited $O(^1D)$ state. The absence of $O(^1D)$ in the beam opened up the possibility of examining the dynamics of many $O(^3P)$ reactions at high relative velocities, with confidence that $O(^1D)$ reactions would not interfere with the experimental results. The first system chosen for study was the $O(^3P) + D_2$ reaction, because it could be modeled very accurately by theoretical methods. In addition, the OD product from this reaction scatters at higher velocities in the c.m. frame than the OH product from the $O(^3P) + H_2$ reaction (for a given relative velocity of the collision); thus the kinematics of the $O(^3P) + D_2$ system are more favorable for investigating the dynamics of the $O(^3P)$ + hydrogen reaction. A Newton diagram showing $O(^3P)$ scattering from D_2 inelastically (O) and reactively (OD) is presented in Fig. 4.1.

Although the dynamics of the $O(^3P) + H_2 \rightarrow OH + H$ reaction have been studied in detail theoretically,[1-13] there are no previous experimental investigations of the dynamics of this reaction. As mentioned before, the primary reason for the paucity of data on the dynamics of this reaction this is the high relative velocity required to overcome the ~9 kcal mol^{-1} barrier. Many experiments and calculations have been done on the $O(^1D) + H_2 \rightarrow OH + H$ reaction, however, which is virtually barrierless.[14-19] These studies have revealed that the OH product

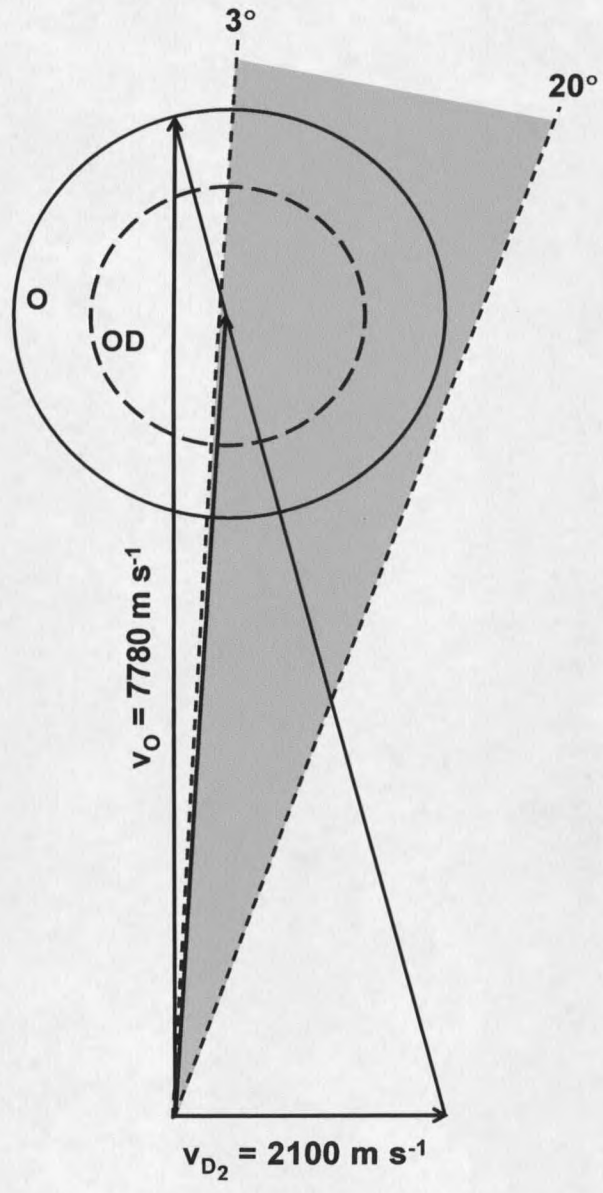

Figure 4.1. A Newton diagram showing inelastically scattered O and reactively scattered OD from hyperthermal collisions of O(^3P) with D_2 at E_{coll} = 25 kcal mol^{-1}. The angular range in gray represents the range of laboratory detection angles used. The circles represent the maximum recoil velocity of the O (solid line) and OD (dashed line) given the energy available for reaction. The available energy for the inelastic scattering is the collision energy, while the available energy for the reaction to form OD is the collision energy minus the endoergicity of the reaction (~2.3 kcal mol^{-1}).

angular distribution is forward-backwards symmetric, with low vibrational and relatively high rotational excitation of the OH product.[17] The reaction occurs mostly on the ground state (^{1}A′) surface. In contrast, recent calculations on the reaction of O(^3P) with $H_2(v)$ have predicted mostly backwards scattering for $v = 0$ and 1, shifting to more forward scattering as the initial vibrational energy of the H_2 increases.[20] This shift in scattering behavior has been attributed to the increasing importance of higher impact parameters as the vibrational quantum number increases.[7] As mentioned in the previous chapter, the two lowest lying surfaces, ^{3}A′ and ^{3}A″, are the only triplet surfaces that lead to formation of ground state OH($^2\Pi$). The third triplet state, 2^3A″, is known to lead only to electronically excited products, which are not energetically accessible in our experiments.

A very important feature of the O + H_2 potential energy surfaces (PESs) is the presence of crossings between the low-spin singlet surface and the high-spin triplet surface. Although the singlet surface starts off much higher in energy (~45 kcal mol^{-1}), it possesses a deep potential well, causing it to cross over to the lower energy triplet surfaces. Hoffmann and Schatz have found that the most important singlet-triplet crossings (for nonlinear O–H–H geometries) involve the two triplet states correlated to the OH($^2\Pi$) product and the lowest O(^1D) + H_2 surface, ^{1}A′.[21] Figure 4.2 shows potential energy curves along the minimum energy path of the reaction for slightly bent O–H–H geometries in both the adiabatic (top) and diabatic (bottom) representations.[22] These curves, which are derived from full dimensional potential energy surfaces and CASSAF spin-orbit couplings, show a singlet-triplet crossing just before the top of the triplet barrier. The small energy gap between the singlet and triplet adiabats indicates weak spin-orbit coupling in the system. It therefore appears that intersystem crossing (ISC) from the triplet to the singlet surfaces is possible, but it has not yet been observed experimentally. There are two experimental studies in which reactions involving O(^3P) led to ISC: (1) Casavecchia *et al.*[23] saw intersystem crossing in the a crossed-beams

reactive scattering study of the O(^3P) with CH_3I reaction and (2) Naaman and coworkers[24,25] observed evidence of ISC in reactions of O(^3P) with hydrocarbon clusters and thin organic films, wherein insertion of the oxygen atom was observed instead of abstraction. While the first example contained a heavy atom which is believed to facilitate ISC,[23] the second example demonstrated the possibility to observe ISC without the presence of heavy atoms.

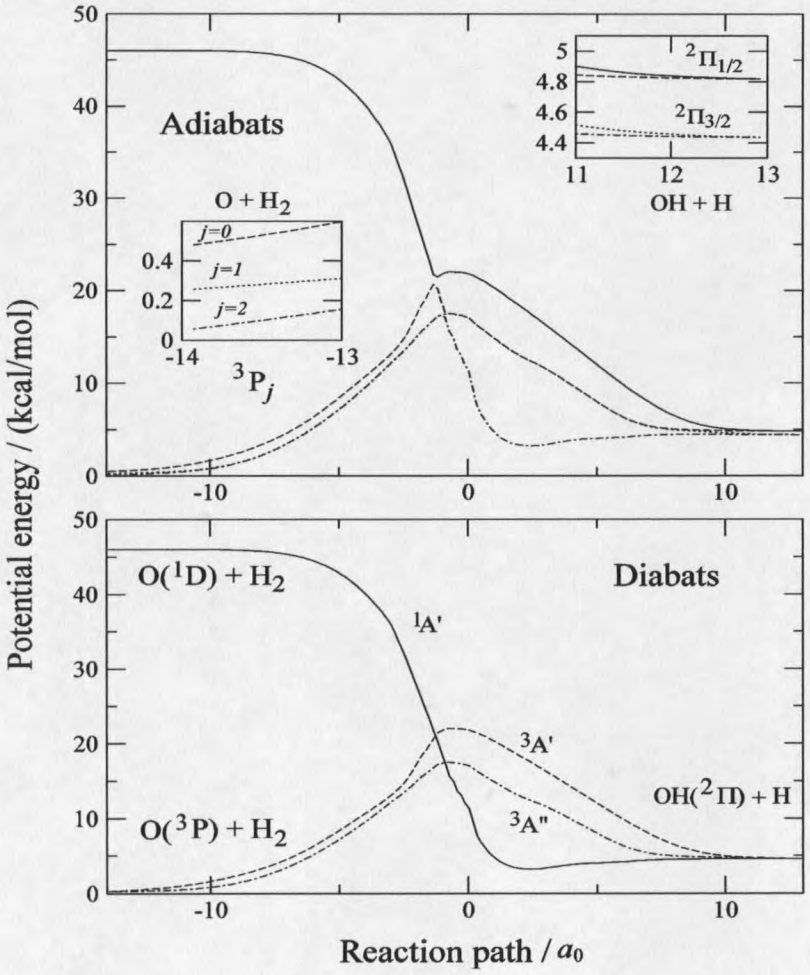

Figure 4.2. Potential energy curves along the minimum energy path for the triplet reaction with H_2 at slightly bent O-H-H geometries (Jacobi angle of 30°). The surfaces ($^1A'$, $^3A'$, and $^3A''$) that correlate to the ground state OH($^2\Pi$) product and that are involved in intersystem crossing are shown. (The collinear geometry has a lower minimum energy path, but no crossings occur.) The top plot shows the adiabatic representation, while the bottom plot shows the diabatic representation. This figure was provided by G. C. Schatz *et al.*

In this chapter, the dynamics of inelastic scattering of $O(^3P)$ from D_2 are explored, as are the dynamics of the only reactive channel, formation of OD. The presence of ISC at these high collision energies is also investigated.

Experimental Details

Experiments were performed on the crossed molecular beam apparatus described in Chapter 2. A pulsed beam of oxygen atoms produced in the laser detonation source and having a nominal velocity of 7780 m s^{-1} was crossed with a pulsed supersonic beam of pure D_2 gas having a nominal velocity of 2100 m s^{-1}. A synchronized 400 Hz chopper wheel was used for velocity selection of the overall oxygen atom beam pulse. Products scattering from the crossing region of the two beams were detected with a rotatable quadrupole mass spectrometer detector.

The oxygen-atom beam exited the source region through a 1 cm diameter skimmer, traveled through a differential pumping region held around 10^{-6} torr, and passed through a second 1.2 mm diameter skimmer before entering the main scattering chamber. The D_2 beam traveled through a 2 mm diameter skimmer into a differential pumping region and then through a 2.5 mm diameter aperture. The main scattering chamber was held at 2×10^{-7} torr throughout the experiment. The oxygen-atom beam produced by the laser detonation source consisted of 63 percent oxygen atoms and 37 percent O_2. As shown in Chapter 3, the oxygen atoms are mostly in the ground, or ^3P, electronic state, with less than one percent (and perhaps no population at all) in the first excited state, ^1D. The oxygen-atom beam distributions were obtained under two detector conditions, both with the D_2 beam off. For one distribution, the detector was placed directly on axis (0°) and for the other the detector was placed at +3° off the oxygen atom beam axis (toward the D_2 beam axis). This served to verify the beam velocity, and also the off-axis beam provided a beam time-of-flight (TOF) distribution under

the same conditions that the scattered products were detected. Products that scattered from the crossing region traveled 33.7 mm to the electron bombardment ionizer in the detector. Ions were selected with a quadrupole mass filter and the resulting ion signals were amplified and counted using a Daly ion counter and multichannel scaler.

Inelastic scattering signals were detected at m/z = 16 (O^+) and 32 (O_2^+). The range of detector angles for which data were collected was based on the Newton diagram shown in Figure 4.1, and varied for detected masses. Signals for m/z = 16 (O^+) were detected at laboratory angles from +3° to +20°. Signals for m/z = 32 (O_2^+), used to corrected the m/z = 16 data for the contribution of cracking of O_2 to O in the ionizer, were detected from +3° to +10° (O_2 did not scatter appreciably to larger angles). Reactive product signals were detected only at m/z = 18 (OD^+) and at laboratory angles of +3° to +12.5°. Counting times varied from 12.5 min for collection of the m/z = 16 and 32 data to 1.4 h for m/z = 18.

Results and Analysis

TOF and laboratory angular distributions were collected for m/z = 16 (O^+), 18 (OD^+), and 32 (O_2^+) at a collision energy, E_{coll}, of 25 kcal mol^{-1}. The Newton diagram in Fig. 4.1 shows the maximum recoil velocity of O and OD given the available energy. For inelastic scattering of oxygen atoms, the available energy is the collision energy (25 kcal mol^{-1}). However, for the reactive scattering to form OD, the maximum energy available for translation is the collision energy minus the endoergicity of the reaction (25 - 2.3 kcal mol^{-1}), or 22.7 kcal mol^{-1}. Scattered O_2 is not included in the Newton diagram since the only purpose for its collection was to correct for its contribution (from dissociative ionization) to the TOF distributions detected at m/z = 16.

Inelastic Scattering

Figure 4.3 shows TOF distributions for $m/z = 16$ collected at six laboratory angles. The TOF distributions at 3° - 10°, where signal was observed for $m/z = 32$, were corrected for the contribution of O_2 cracking to O in the ionizer. This was done by subtracting 11 percent of the signal at $m/z = 32$ (after correction for the ion flight time difference between O and O_2) from the signal at $m/z = 16$. The laboratory angular distribution, or integrated signal as a function of angle, for the oxygen atom inelastic scattering is shown in Fig. 4.4. The solid line in both Figs. 4.3 and 4.4 is the forward convolution simulation to the data based on the c.m. translational energy and angular distributions in Figs. 4.5 and 4.6. These translational energy and angular distributions, which were derived from the experimental TOF and laboratory angular distributions, were very similar to quasiclassical trajectory (QCT) calculation results for $O + D_2 \rightarrow O + D_2$ scattering at $E_{coll} = 25$ kcal mol^{-1} performed by Schatz *et al.* The QCT calculations were run on analytical potential energy surfaces (PES) for the $^3A'$ and $^3A''$ states developed by Rogers *et al.* for reaction of $O(^3P)$ with H_2,[5] and c.m. translational energy and angular distributions were extracted from the trajectory data. Both the $^3A'$ and $^3A''$ surfaces gave nearly identical results for inelastic scattering. The major differences between the c.m. distributions derived from the experimental data and the QCT results for both surfaces were in the widths of the two distributions. The QCT results for the translational energy distribution fell to zero around 22 kcal mol^{-1}, as opposed to ~18 kcal mol^{-1} in the experimentally derived translational energy distribution. The angular distribution also fell more sharply in the QCT. The general results from the QCT calculations and the experimentally derived distributions were the same, showing forward scattering of the oxygen atoms, with very little energy transferred into the D_2 collision partner. The simulation provides reasonably good agreement with the data in Figs. 4.3 and 4.4; however, it must be noted that due to the fairly low resolution of the data, the simulated "fits" are not entirely unique. Small changes in the c.m.

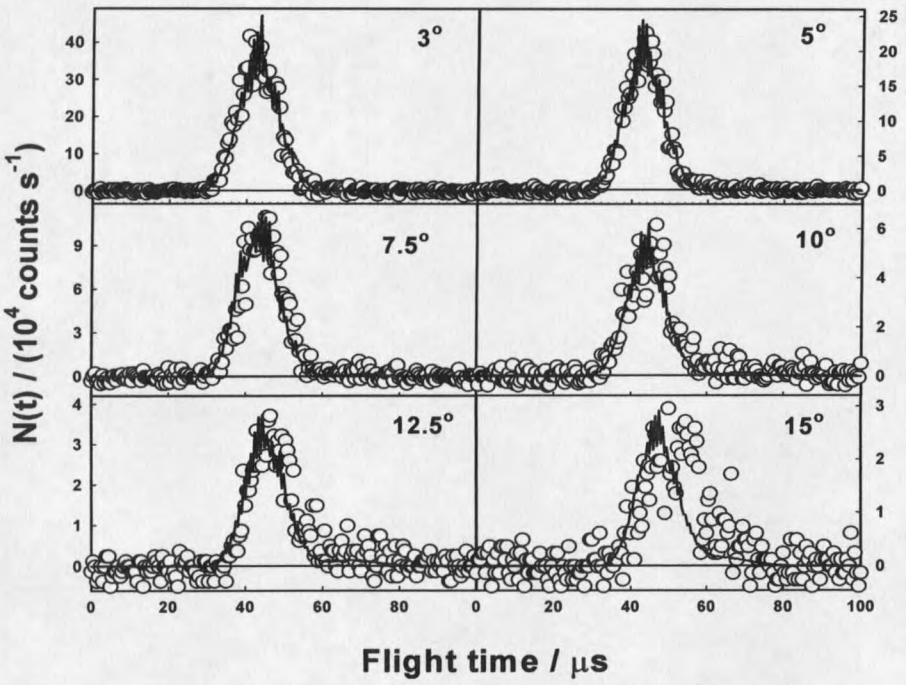

Figure 4.3. Representative time-of-flight distributions of inelastically scattered O following collisions with D_2 at E_{coll} = 25 kcal mol^{-1}. The open circles are the experimental data. The solid line is the forward convolution simulation to the data, derived from the c.m. translational energy and angular distributions in Figs. 4.5 and 4.6.

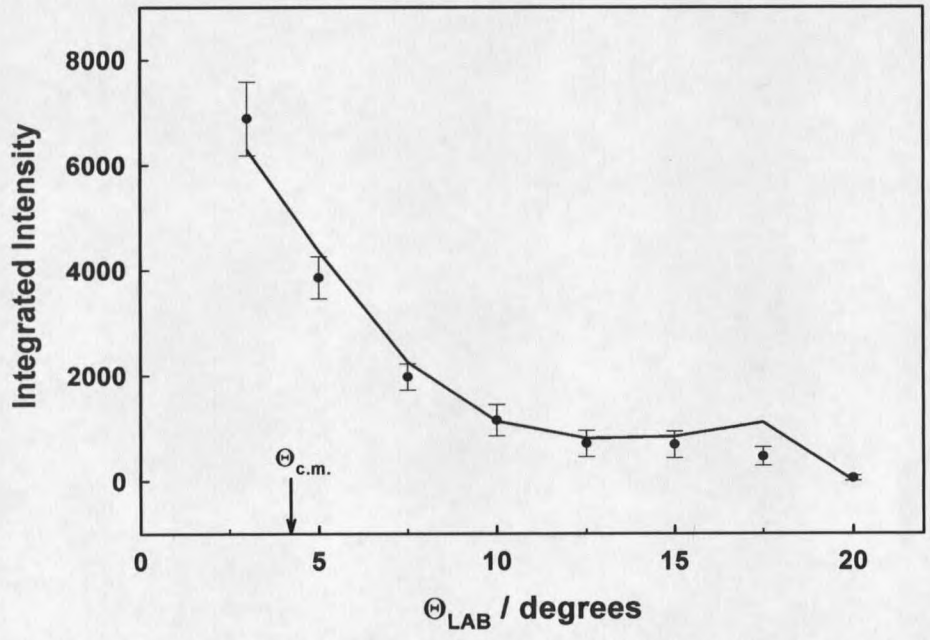

Figure 4.4. Laboratory angular distribution of m/z = 16 (O^+) inelastically scattered from D_2 with E_{coll} = 25 kcal mol^{-1}. The circles are the experimental data, and the solid line is the forward convolution fit to the data.

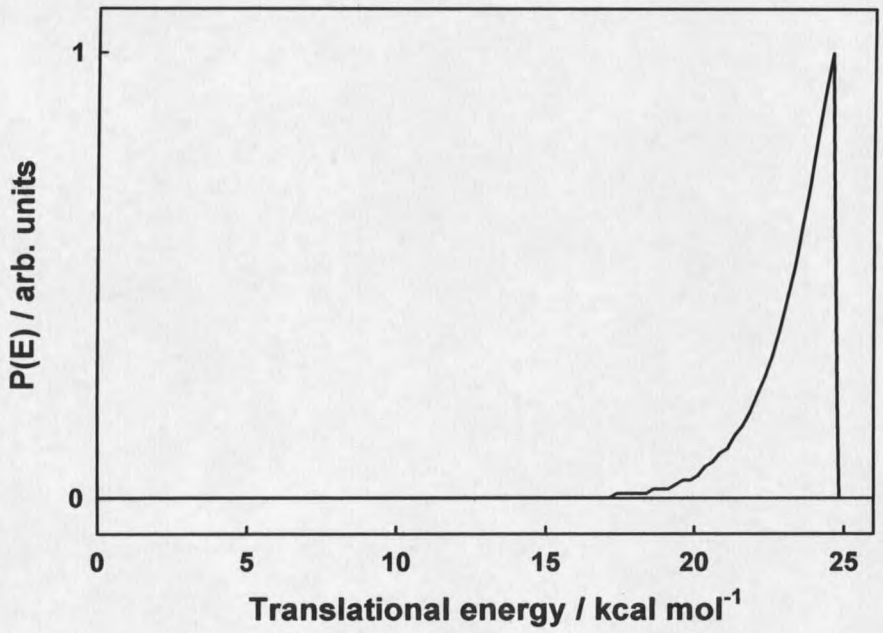

Figure 4.5. Center-of-mass translational energy distribution for the inelastic scattering of O from D_2 at E_{coll} = 25 kcal mol^{-1}, derived from the TOF and laboratory angular distributions for m/z = 16 (O^+) through the forward convolution method.

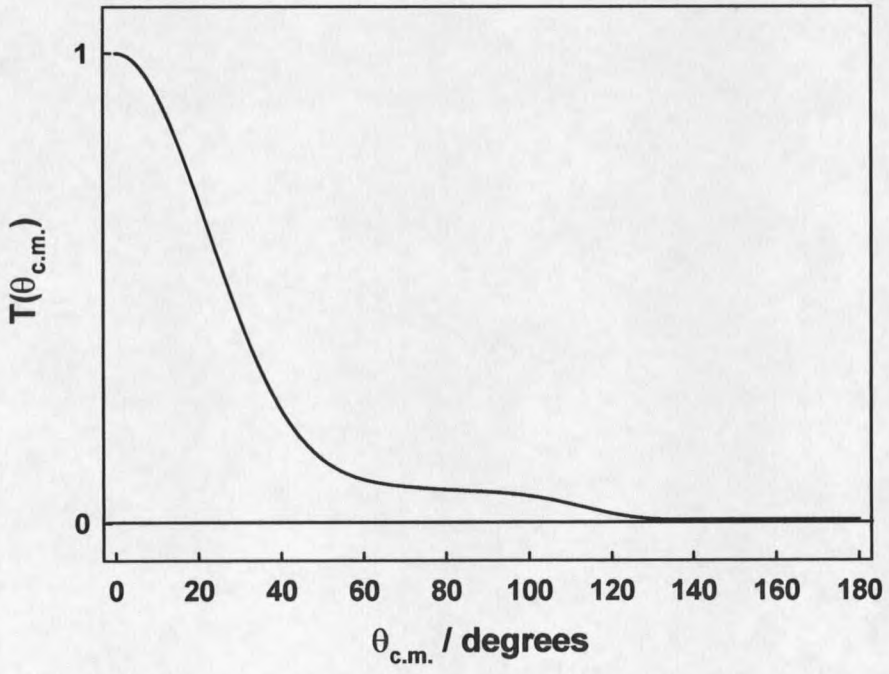

Figure 4.6. Center-of-mass angular distribution for O atoms that scatter inelastically from D_2 at E_{coll} = 25 kcal mol^{-1}, derived from the TOF and laboratory angular distributions for m/z = 16 (O^+) through the forward convolution method.

translational energy and angular distributions will still result in acceptable "fits" to the data. For example, the translational energy distribution for the inelastic scattering of O from D_2 can be broadened slightly, while keeping the peak near 25 kcal mol^{-1}, and the fit to the laboratory TOF and angular distributions is not greatly affected. On the other hand, large changes, altering the character of the generated c.m. distributions, show significant deviations from the simulated results. This insensitivity of the experimental data to small changes in the c.m. distributions is the result of high product velocities and, especially, the temporal width of the incident oxygen-atom beam distribution, which inhibits velocity resolution and thus the accuracy of the derived c.m. distributions. Although the velocity resolution is lower than would be desired, there are limits within which to work. (The error associated with the simulations will be explored in more detail in the following section.) While we cannot achieve perfect "fits" to the data because of limited resolution, we can make general statements about the nature of the scattering in the c.m. frame, such as scattering direction and energy transfer. A c.m. velocity flux map, created from the two experimentally derived c.m. distributions for oxygen atom inelastic scattering, is shown in Fig. 4.7.

Reactive Scattering

Representative TOF distributions of the only reactively scattered product observed, OD, collected at laboratory angles of 3°, 7.5°, 12.5°, and 15° are shown in Fig. 4.8. The distributions at 3°, 5°, and 7.5° had to be corrected for the contribution of ^{18}O that scattered inelastically from D_2. This correction was done by multiplying the scattering signal at $m/z = 16$ (O^+) for each angle by 0.002 (0.2 percent ^{18}O, which was measured by scattering oxygen from helium and looking at the scattered signal at $m/z = 16$ (O^+) and $m/z = 18$ ($^{18}O^+$) in a separate experiment), shifting by the appropriate ion flight time, and subtracting it from the TOF distributions collected at $m/z = 18$. This correction was negligible (less than one count) at

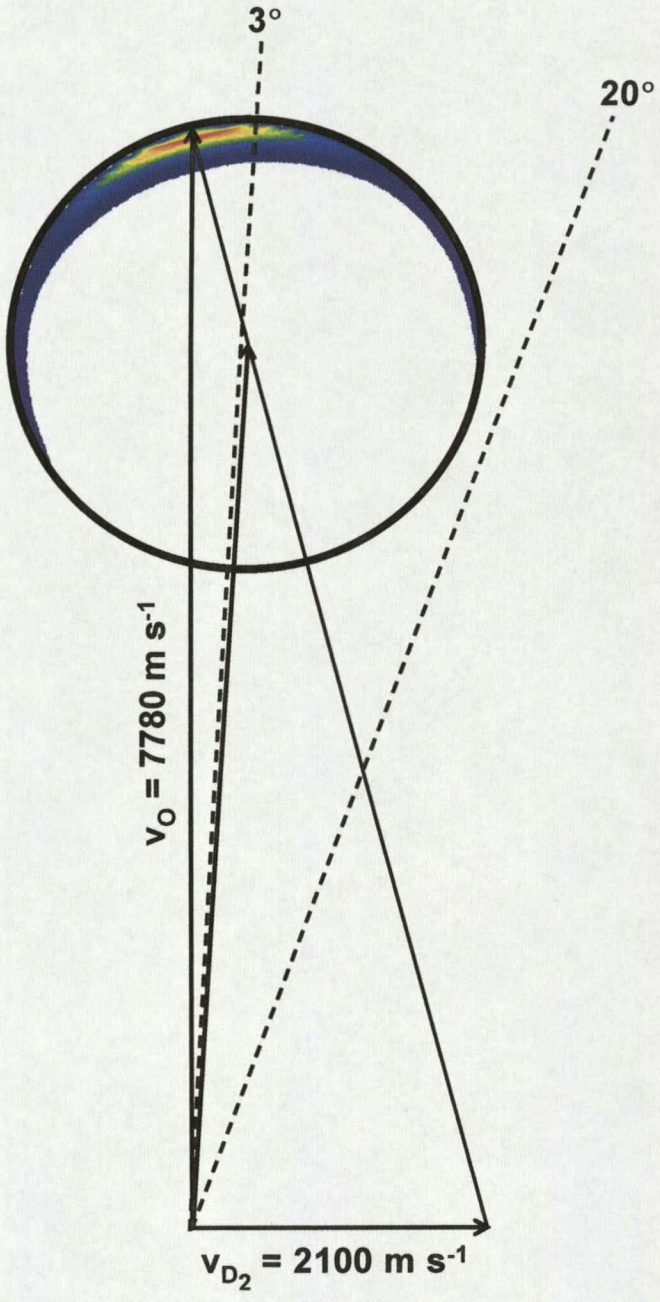

Figure 4.7. Center-of-mass velocity-flux map superimposed on a Newton diagram for O atoms that scatter inelastically from D_2 at E_{coll} = 25 kcal mol^{-1}. The translational energy and angular distributions in Fig. 4.5 and 4.6 were used to create this velocity-flux contour map. Scattered intensity is maximum in the forward direction (indicated by the red color).

angles greater than 7.5°, and so these angles were not corrected for ^{18}O contributions. Laboratory angular distributions are shown in Fig. 4.9. The three curves in each plot represent three different "fits" to the data, one using the results of QCT trajectory calculations and two from c.m. translational energy and angular distributions that gave reasonable fits to all the data. Multiple c.m. distributions were used, in order to investigate carefully the sensitivity of the data to different c.m. functions. The black curves in Figs. 4.8 - 4.11 are the results of high quality single surface QCT calculations performed by Schatz *et al.* on the two triplet surfaces ($^3A'$ and $^3A''$) that correlate to the OD + D products in the ground electronic state. (The third surface is very repulsive and leads to the formation of excited state products that would not be accessible with the collision energies used in the experiment. This surface was therefore not included in the trajectory studies.) Center-of-mass translational energy and angular distributions for the $O(^3P) + D_2 \rightarrow OD + D$ reaction were obtained from the trajectory calculations. Forward convolution of the c.m. distributions obtained from these triplet-only trajectory calculations allowed conversion of the data into the laboratory frame and gave predicted TOF and laboratory angular distribution. These results (black curves) were compared with the experimental data in Fig. 4.8 and 4.9, and seem to provide acceptable fits to the TOF distributions in Fig. 4.8, but they do not show very good agreement with the laboratory angular distribution in Fig. 4.9. The inability of the QCT results to fit the laboratory angular distributions prompted us to try different c.m. translational energy and angular distributions, in order to improve the agreement between the c.m. and laboratory distributions. The red and green curves in Fig. 4.8 - 4.11 are c.m. distributions that provide the superior fits to the data. However, as both curves provide good "fits" to the data, they also show the problem of "uniqueness" in the forward convolution simulation to the data. The red and green curves in Fig. 4.10 have a maximum near the same energy and are quite different in shape, but they are similar in the total energy range they cover. And both of the experimentally derived

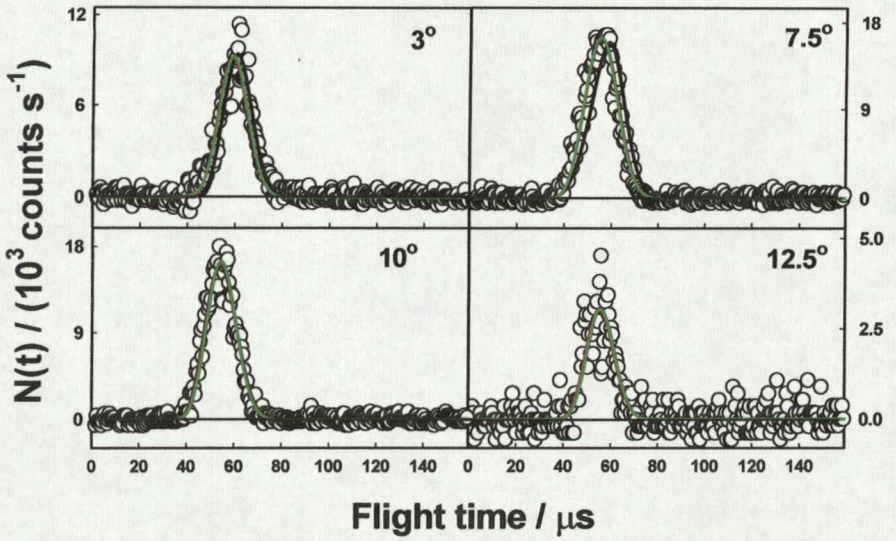

Figure 4.8. Representative time-of-flight distributions of reactively scattered OD following reaction of O(^3P) with D_2 at E_{coll} = 25 kcal mol^{-1}. The open circles are the experimental data. The solid lines show three different results from forward convolution simulation of the data, derived from c.m. distributions shown in Figs. 4.10 and 4.11. The black line shows the results from quasiclassical trajectory calculations (also shown in black in Figs. 4.9, 4.10, and 4.11). The green and red lines show two different results obtained from forward convolution of the corresponding c.m. distributions shown as green and red curves, respectively, in Figs. 4.10 and 4.11. Where red and green lines overlap, a green line is shown.

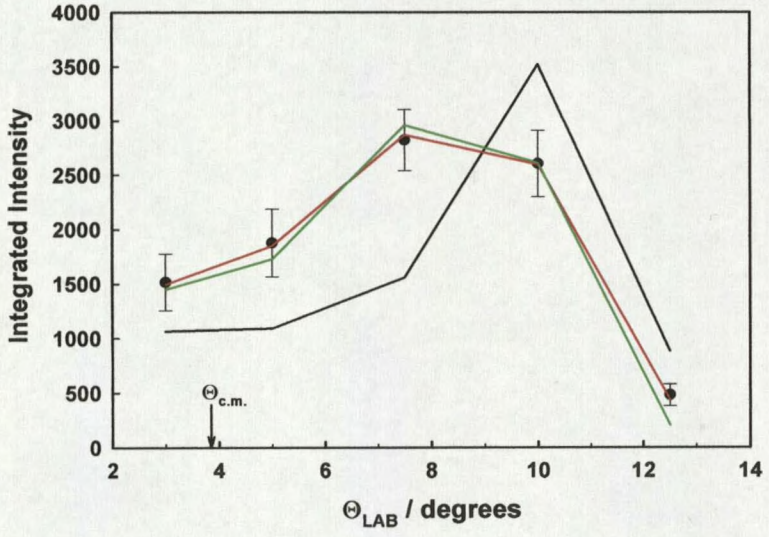

Figure 4.9. Laboratory angular distribution of the OD product from the reaction of O(^3P) with D_2 at E_{coll} = 25 kcal mol^{-1}. The black dots are the experimental data. The error bars are estimated from fitting the TOF distributions with a modified gaussian function and finding maximum and minimum acceptable fits by adjusting the gaussian parameters. The integrated range of these fits are shown as error bars.

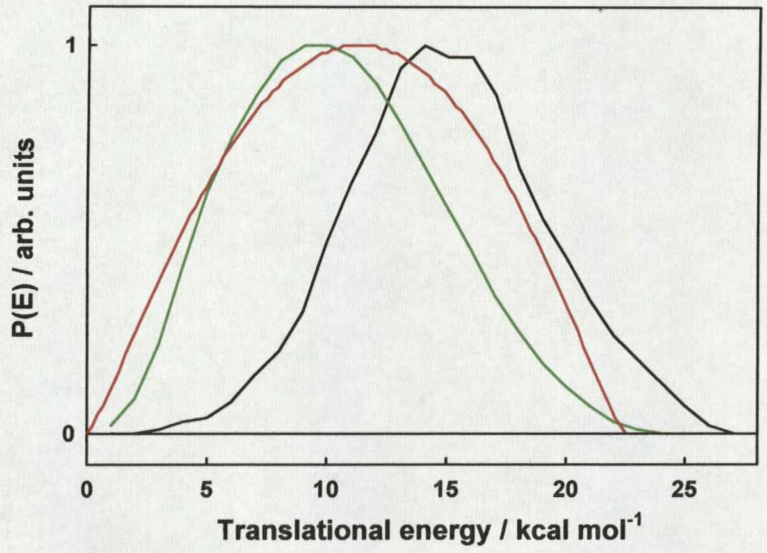

Figure 4.10. Center-of-mass translational energy distributions for the $O(^3P) + D_2 \rightarrow OD + D$ reaction at $E_{coll} = 25$ kcal mol^{-1}. The black curve is the translational energy distribution from quasiclassical trajectory calculations by Schatz *et al.* The green and red curves are two seperate "fits" derived from the TOF and laboratory angular distributions for $m/z = 18$ (OD^+) through the forward convolution method. The green and red curves represent the degree of error in simulating the experimental data.

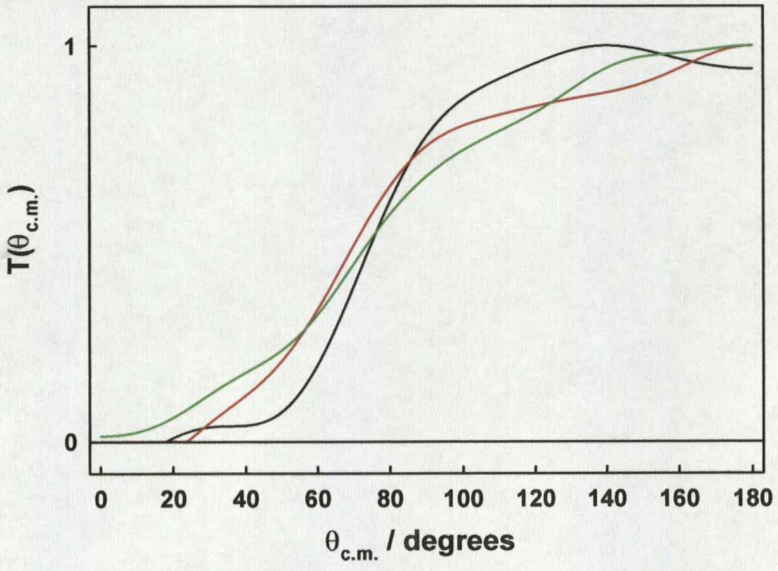

Figure 4.11. Center-of-mass angular distributions for the $O(^3P) + D_2 \rightarrow OD + D$ reaction at $E_{coll} = 25$ kcal mol^{-1}. The black curve is the angular distribution from quasiclassical trajectory calculations by Schatz *et al.* The green and red curves are two seperate "fits" derived from the TOF and laboratory angular distributions for $m/z = 18$ (OD^+) through the forward convolution method. The green and red curves represent the degree of error in simulating the experimental data.

translational energy distributions (red and green curves) have maxima at lower energies than that of the distribution from the QCT calculations. The c.m. angular distributions, shown in Fig. 4.11, corresponding to the red and green translational energy distributions, show similar features, such as a preponderance of backwards scattering and very little forward scattering. Both the experimentally derived c.m. angular distributions are also similar to the distribution obtained from the QCT calculations. The three different c.m. translational energy and angular distributions thus provide an effective error range for the forward convolution simulation procedure. We can draw general conclusions about the scattering based on the three "fits". All three c.m. angular distributions show a large backward scattered peak. The presence of forward scattered OD is difficult to determine with the resolution of the data, but it is possible that there is a small amount of forward scattered OD. We can also determine that there is a broad range of energy transferred into the recoiling OD fragment, and on average ~50 percent of available energy for reaction (E_{coll} - ΔE_r) goes into internal energy of the OD. The inability of the QCT results to predict the laboratory angular distribution suggests that the maximum energy in the translational energy distribution is overestimated. A velocity-flux maps created from the three different sets of translational energy and angular distributions from Figs. 4.10 and 4.11 are shown in Figs. 4.12 - 4.14.

Discussion

The inelastic and reactive scattering events resulting from collisions of $O(^3P)$ with D_2 exhibit significantly different dynamics. For both the inelastic and reactive scattering experiments, results have been compared with high quality triplet-only QCT calculations provided by Schatz *et al.* In the case of inelastic scattering, experimental results showed that oxygen atoms scatter from D_2 with little change in direction and translational energy. The c.m. translational energy distribution for the oxygen atoms has a maximum near the c.m.

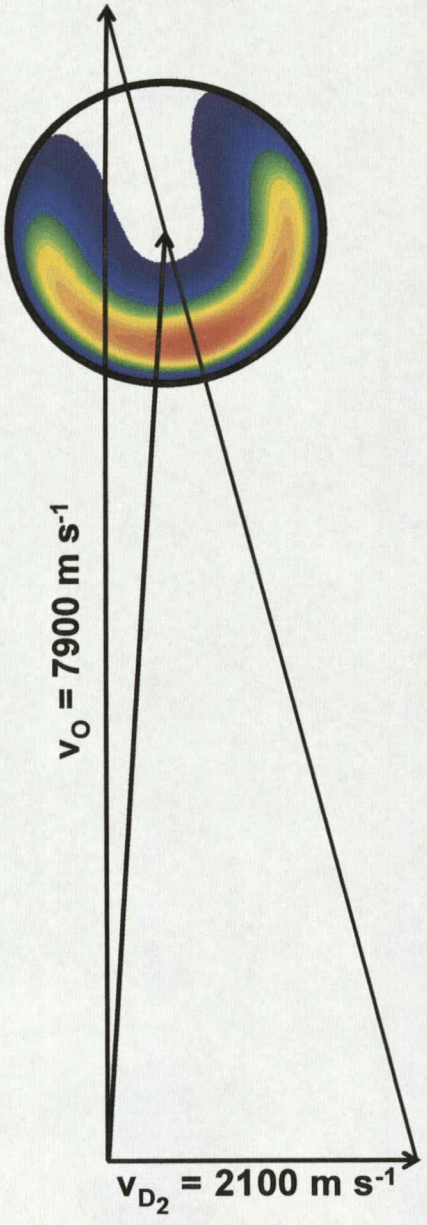

Figure 4.12. Center-of-mass velocity-flux map superimposed on a Newton diagram for the OD product from the reaction of $O(^3P) + D_2 \rightarrow OD + D$ at $E_{coll} = 25$ kcal mol^{-1}. This velocity flux map was created using the red translational energy and angular distributions in Figs. 4.10 and 4.11.

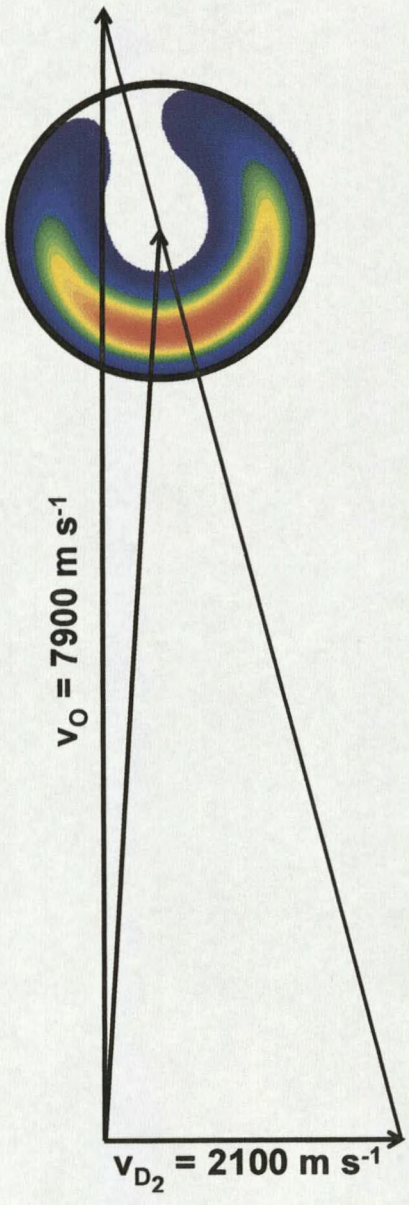

Figure 4.13. Center-of-mass velocity-flux map superimposed on a Newton diagram for the OD product from the reaction of $O(^3P) + D_2 \rightarrow OD + D$ at $E_{coll} = 25$ kcal mol^{-1}. This velocity flux map was created using the green translational energy and angular distributions in Figs. 4.10 and 4.11.

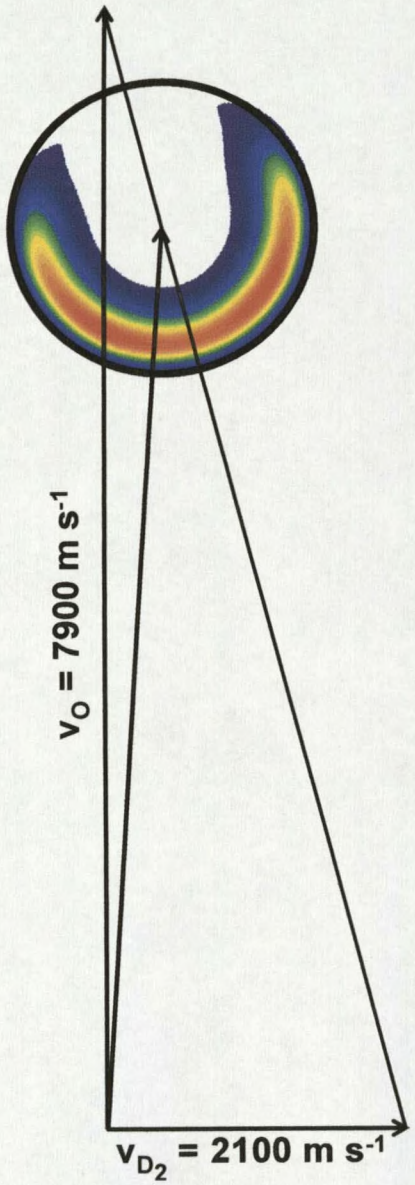

Figure 4.14. Center-of-mass velocity-flux map superimposed on a Newton diagram for the OD product from the reaction of $O(^3P) + D_2 \rightarrow OD + D$ at $E_{coll} = 25$ kcal mol^{-1}. This velocity-flux map was created using the QCT results for translational energy and angular distributions (black curves) in Figs. 4.10 and 4.11.

collision energy in both the experimental and the QCT results, implying little internal energy transfer. It appears as though some of the energy in the collision may be transferred into internal energy of the D_2, but this quantity is estimated to be less than 15 to 20 percent of the collision energy. The c.m. angular distribution derived from the experimental data for the inelastic scattering of O is highest in the direction of the oxygen-atom beam, which is in excellent agreement with the QCT calculations, although the experimentally derived results are slightly broader. We can thus conclude that within our experimental error, the QCT calculations accurately reproduced the experimental findings, and in both experiment and theory, the picture of scattering that emerges is one in which the oxygen atoms scatter from the D_2 with large impact parameter ("glancing") collisions, resulting in very little energy transfer into the D_2 molecule and very little change in direction.

Reactive scattering of OD was observed, but the data were challenging to simulate with unique c.m. translational energy and angular distributions. Because $O(^3P) + H_2$ had been shown in QCT calculations (with no coupling to singlet surfaces) to lead to backwards scattered products and about half of the available energy in translation, these conditions were the starting point in the forward convolution. The resulting match to the data was acceptable for the TOF distributions but unacceptable for the laboratory angular distribution. Different c.m. distributions were therefore investigated in order to obtain a good fit to both laboratory distributions and test the sensitivity of the data to the assumed c.m. distributions. More than one distribution that provided good "fits" to the TOF and angular distributions was found, demonstrating the difficulty of uniqueness in the c.m. distributions as the result of low velocity resolution in the experimental data. Nonetheless, we were able to show that the OD is significantly backwards scattered, and on average, ~50 percent of the available energy goes into internal energy of the OD fragment. The nature of the OD scattering dynamics, highly backwards scattered and large internal excitation, is indicative of a small impact parameter

("head-on") collision between the O and D_2. The prominent backwards scattering and large energy transfer is in stark contrast to the inelastic scattering dynamics which showed exclusive forward scattering with very little energy transfer.

In these experiments it is impossible to tell how the energy is partitioned into vibration and rotation; however, this issue has been addressed in QCT calculations by Braunstein and Schatz.[20] They found that in the reaction, $O + H_2(v = 0) \rightarrow OH(v', j) + H$, at $E_{coll} = 26$ kcal mol^{-1}, the $v' = 0$ state of the OH was found to be the most populated, followed by small populations in the $v' = 1$ and 2.[20] There was no population found in vibrational states above $v' = 2$ when starting from the ground vibrational state of H_2. Rotational distributions calculated for reaction at $E_{coll} = 18$ kcal mol^{-1}, showed rotational population up to the $j = 16$ state of OH, with a peak around $j = 6$ for the $v' = 0$ state.[20] It therefore appears as though the internal energy that is transferred goes into both rotation and vibration of the OH product.

The issue of ISC in the $O + D_2 \rightarrow OD + D$ reaction can be investigated by analysis of the scattering behavior of the OD product. It appears from the c.m. translational energy distributions for this reaction that there is very little or no scattering directly forward ($\Theta = 0°$). If ISC were occurring in the experiments, some forward scattering of the OD product would be expected to be observed, because the products would exhibit singlet dynamics, which show forward-backwards symmetry in the angular distribution. It is difficult to tell from the experimental data, but the presence of some forward scattering is certainly within our experimental error; therefore, it is possible that there may be a small amount, perhaps less than ~5 percent, of the reactions proceeding via ISC to the singlet surface. We can, however, conclude from the experiments that the reaction is occurring almost exclusively on the $^3A'$ and $^3A''$ diabats, with negligible surface hopping. Absence of ISC was also observed in the measurement of the excitation function for $O + H_2 \rightarrow OH + H$ reaction in Chapter 3, which was examined at lower collision energies.

A final point of discussion involves whether the molecular oxygen present in the oxygen beam would affect the observed scattering distributions. For the inelastic scattering signals, TOF distributions were collected for both O and O_2, and any cracking of O_2 in the ionizer to O was subtracted from the $m/z = 16$ (O^+) TOF distributions. The presence of O_2 therefore would not affect the results for the inelastic scattering. Regarding the reactive scattering results to form OD, the lowest barrier reaction in which O_2 can lead to signal at $m/z = 18$ (OD^+) is $O_2(^3\Sigma) + D_2 \rightarrow OOD + D$, where the OOD cracks to OD in the ionizer. The endoergicity of this reaction, however, is ~55 kcal mol^{-1}, much larger than the available energy, thus this reaction cannot occur, since the barrier must be at least as large as the endothermicity. We can therefore rule out any interference of O_2 on the OD reactive signal.

Conclusion

The dynamics of the interactions of $O(^3P)$ with D_2 have been investigated in detail using crossed molecular beams methods. Experiments on the inelastic scattering of $O(^3P) + D_2$ show that oxygen atoms scatter from D_2 in relatively large impact parameter collisions leading to forward scattering with very little internal energy transfer into D_2. In contrast, the only reactive channel, $O + D_2 \rightarrow OD + D$, gave OD products that were almost exclusively backwards scattered and underwent large energy transfers (on average 50 percent) into internal modes of OD. The scattering behavior of the OD was thus indicative of small impact parameter collisions between the two reactants. All of the dynamics observed in the experiments were in relatively good agreement with very accurate quasiclassical trajectory calculations by Schatz *et al.* The presence of intersystem crossing was investigated, and little to no intersystem crossing is observed even at the high collision energies (25 kcal mol^{-1}) used in the experiments, even though theoretical calculations suggest that surface hopping is possible above collision energies of ~20 kcal mol^{-1}.

References

1. R. E. Howard, A. D. McLean and W. A. Lester, *J. Chem. Phys.* **71**, 2412 (1979).

2. S. P. Walch, T. H. Dunning, R. Raffenetti, and F. W. Bobrowicz, *J. Chem. Phys.* **72**, 406 (1980).

3. J. S. Wright, D. J. Donaldson, and R. J. Williams, *J. Chem. Phys.* **81**, 397 (1984).

4. T. Joseph, D. G. Truhlar and B. C. Garrett, *J. Chem. Phys.* **88**, 6982 (1988).

5. Rogers, D. Wang, A. Kuppermann, and S. P. Walch, *J. Phys. Chem. A* **104**, 2308 (2000).

6. B. R. Johnson and N. W. Winter, *J. Chem. Phys.* **66**, 4116 (1977).

7. R. Schinke and W. A. Lester, *J. Chem. Phys.* **70**, 4893 (1979).

8. G. C. Schatz, *J. Chem. Phys.*, **83**, 5677 (1985).

9. J. M. Bowman, *Chem. Phys. Lett.* **141**, 545 (1987).

10. D. C. Chatfield, R. S. Friedman, G. C. Lynch, D. G. Truhlar, and D. W. Schwenke, *J. Chem. Phys.* **98**, 342 (1993).

11. B. C. Garrett, and D. G. Truhlar, *Int. J. Quant. Chem.* **29**, 1463 (1986).

12. B. C. Garrett, D. G. Truhlar, and G. C. Schatz, *J. Am. Chem. Soc.* **108**, 2876 (1986).

13. A. F. Wagner and J. M. Bowman, *J. Chem. Phys.* **86**, 1976 (1987).

14. M. Alagia, N. Balucani, L. Cartechini, P. Casavecchia, E. H. van Kleef, G. G. Volpi, P. J. Kuntz, and J. J. Sloan, *J. Chem. Phys.* **108**, 6698 (1998).

15. J. A. Davidson, H. I. Schiff, G. E. Streit, J. R. McAfee, A. L. Schmeltekopf, and C. J. Howard, *J. Chem. Phys.* **67**, 5021 (1977).

16. S. K. Gary, G. G. Balint-Kurti, G. C. Schatz, J. J. Lin, X. Liu, S. Harich, and X. Yang, *J. Chem. Phys.* **113**, 7330 (2000).

17. X. Liu, J. J. Lin, S. Harich, G. C. Schatz, and X. Yang, *Science* **289**, 1536 (2000).

18. F. J. Aoiz, L. Banares, J. F. Castillo, M. Brouard, W. Denzer, C. Vallance, P. Honvault, J-M Launay, A. J. Dobbyn and P. J. Knowles, *Phys. Rev. Lett.* **86**, 1729 (2001).

19. G. C. Schatz, L. A. Pederson, and P. J. Kuntz, *Faraday Discuss.* **108**, 357 (1997).

20. M. Braunstein, S. Alder-Golden, B. Maiti, and G. C. Schatz, *J. Chem. Phys.* **120**, 4316 (2004).

21. M. R. Hoffman and G. C. Schatz, *J. Chem. Phys.* **113**, 9456 (2000).

22. B. Maiti and G. C. Schatz, *J. Chem. Phys.* **119**, 12360 (2003).

23. M. Alagia, N. Balucani, L. Cartechini, P. Casavecchia, M. van Beek, G. G. Volpi, L. Bonnet, and J. C. Rayez, *Faraday Discuss.* **113**, 133 (1999).

24. Y. Rudlich, S. Lifson, and R. Naaman, *J. Chem. Phys.* **98**, 2936 (1993).

25. Y. Paz, S. Trakhtenberg, and R. Naaman, *J. Phys. Chem.* **97**, 9075 (1993).

EXCITATION FUNCTION FOR THE $O(^3P) + CH_4 \rightarrow OCH_3 + H$ REACTION

Introduction

The key to understanding the mechanisms of hydrocarbon polymer degradation in low Earth orbit lies in deciphering the detailed mechanism of each microscopic interaction the $O(^3P)$ atoms have with the polymer surface. While much has been and will continue to be learned from studying gas-surface interactions, investigating analogous gas-phase reactions can provide important information that would otherwise be lost in the surface studies. Additionally, performing theoretical calculations on surfaces is much more difficult and time consuming than calculations done on smaller gas-phase systems. We therefore have performed experiments to probe the detailed dynamical interactions between $O(^3P)$ atoms and saturated hydrocarbons by starting with the smallest possible model hydrocarbon system, methane. Because it contains only one carbon, it is the easiest hydrocarbon system for which to obtain a dynamical picture from both experiments and theoretical calculations.

Prior to the experiments described herein, the only reaction known to occur when an $O(^3P)$ atom collides with a methane molecule is hydrogen atom abstraction to form OH. The relatively low barrier of this reaction, ~8 kcal mol^{-1},[1] has made the study of hydrogen atom abstraction accessible in a few low collision energy experiments. The first investigation of the dynamics of the reaction was carried out by Hirota *et al.*,[2] who looked at the vibrational distributions of the CH_3 radical. McKendrick and coworkers also performed experiments on the $O(^3P) + CH_4$ reaction, but chose to detect and obtain internal state information on the OH product using laser induced fluorescence.[3] While not many dynamics studies exist on the reaction of $O(^3P) + CH_4$, many theoretical investigations have been done as well as numerous studies on larger saturated hydrocarbons.[4-6] The seminal (albeit low-energy) work on $O(^3P)$

reactions with hydrocarbons was done by Andresen and Luntz.[4] In a dual experiment and theory effort, they concluded that the oxygen atom stripped a hydrogen atom off, with very little internal energy transfer, leaving the alkyl radical as just a spectator in the reaction. The size of the alkyl fragment was only believed to be important because of its effect on the strength of the C-H bond, since a primary C-H bond is thought to weaken in a saturated hydrocarbon as the number of carbons is increased.

Consideration of an energy diagram (see Fig. 5.1) for the $O(^3P) + CH_4$ reaction reveals that the OH abstraction, while the lowest barrier channel, is not the only channel that is accessible at high collision energies. Recent observation of new reaction channels at high collision energies both in our laboratory and in calculations by Schatz *et al.*[1,7] have motivated more detailed experimental and theoretical studies at hyperthermal energies (center-of-mass collision energies in the range 35-95 kcal mol^{-1}). The most significant of these new channels is an oxygen atom addition with subsequent hydrogen atom elimination that yields H + OCH_3.

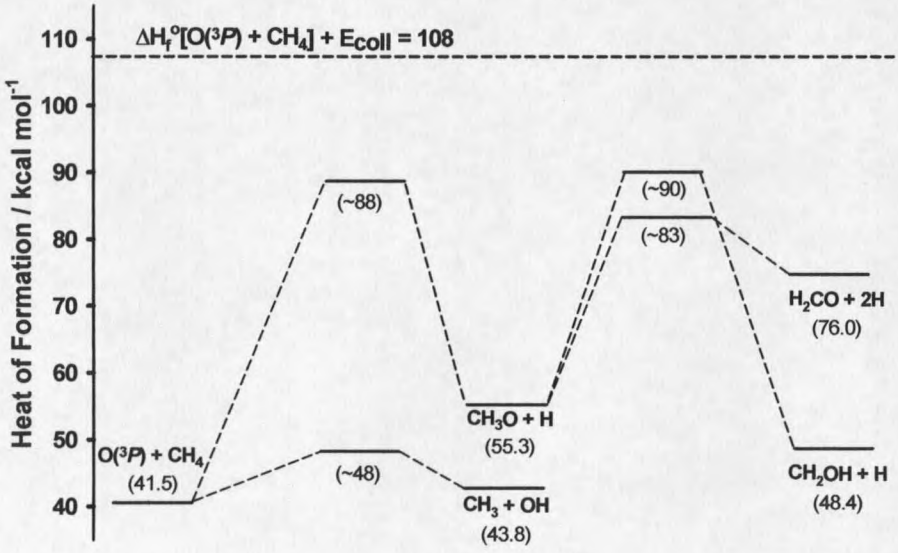

Figure 5.1. Energy diagram for the possible reaction channels in the reaction of $O(^3P)$ with CH_4. The numbers in parenthesis are in kcal mol^{-1}. The horizontal line at the top shows the maximum available energy for reaction under experimental conditions in kcal mol^{-1}.

The $O + CH_4 \rightarrow OCH_3 + H$ reaction is difficult to study with crossed-beams methods because of the small Newton circle into which the OCH_3 product is scattered. A Newton diagram with representative oxygen atom and CH_4 laboratory beam velocities is shown in Fig. 5.2. As in the case of $O + H_2$, which was discussed in Chapter 3, the small Newton circle limits product angular and translational energy resolution, information that would be useful in deciphering the reaction dynamics. However, it is ideal for the purposes of observing the formation of the OCH_3 product and obtaining the excitation function, since the flux measurement at one angle would give a good representation of the overall flux of products produced in the reaction.

In this chapter, the occurrence of the important and hitherto unstudied reaction of $O(^3P) + CH_4 \rightarrow OCH_3 + H$ is investigated and the experimental excitation function is measured for a broad range of collision energies close to the reaction threshold. The experimental data is compared with theoretical results based on direct dynamics quasiclassical trajectory (QCT) calculations by Schatz *et al.* The experiment and theory comparisons allow clarification of two fundamental issues that are encountered in any study of $O(^3P)$ + hydrocarbon (gas-phase or polymer) reactions: (1) the effect of excited surfaces of overall triplet multiplicity on the reactive cross sections, and (2) the importance of intersystem crossing on the reactive cross sections.

Experimental Details

The experiments were performed with the use of the crossed molecular beams apparatus described in Chapter 2. The oxygen-atom beam created by the laser detonation source passed from the source chamber through a 1 cm diameter aperture into a differential pumping region and then passed through a 3 mm diameter collimating aperture (~95 cm from the source nozzle) into the main scattering chamber. The newer synchronized chopper

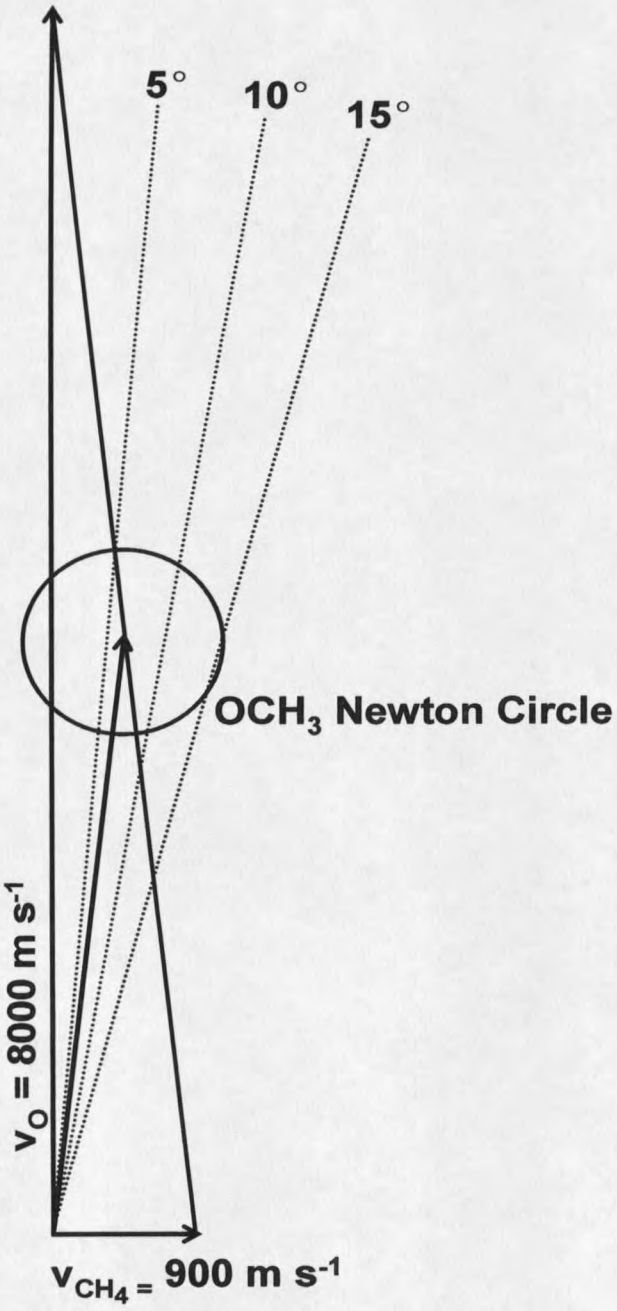

Figure 5.2. A Newton diagram for the OCH_3 + H channel of the $O(^3P)$ + CH_4 reaction at E_{coll} = 62 kcal mol^{-1}. The circle represents the maximum velocity of the OCH_3 product given the energy available for reaction.

wheel was used to select a narrow portion of the beam pulse. The chopper wheel frequency was 300 Hz. The narrowed oxygen-atom beam pulse had a nominal velocity width (FWHM) of ~450 m s^{-1}, and this width was somewhat dependent on the average velocity of the pulse that passed through the chopper wheel: larger average velocities had broader velocity distributions. The hyperthermal oxygen-atom beam was crossed at right angles with a beam pulse of pure CH_4. The crossing region of the two beams was at 99 cm from the apex of the laser-detonation nozzle cone and 12 cm from the CH_4 pulsed valve source. The CH_4 beam also passed through two regions of differential pumping, including a collimating aperture, and the resulting beam cross section at the crossing region was 2.5 mm × 2.5 mm. The CH_4 beam had a nominal velocity of ~0.9 km s^{-1}. As mentioned in Chapter 2, the value of this velocity was only determined to an accuracy of about ten percent, but this error had no effect on the experimental results, because the colliding oxygen-atom beams had average oxygen-atom velocities of an order of magnitude higher than the CH_4 beam. The rotatable mass spectrometer detector was used to monitor the oxygen-atom and CH_4 beams as well as the products that scattered from the crossing region of the two beams. Number density distributions of mass-selected species were collected as a function of their arrival time in the ionizer. The CH_4 beam showed no signal at masses that would indicate the presence of dimers or higher clusters in the beam. In order to determine the incident oxygen-atom velocity distribution, the detector was rotated such that the detection and hyperthermal beam axes coincided, and number density distributions, *N(t)* (also known as time-of-flight distributions), were collected as a function of the flight time from the nozzle to the ionizer of the mass spectrometer detector. Time-of-flight (TOF) distributions of inelastically and reactively scattered products were collected, with the detector rotated away from either beam axis, as a function of the flight time from the crossing region of the two beams to the detector ionizer (33.66 cm). From the TOF distributions of the oxygen-atom beam, velocity distributions

were derived, thus allowing the determination of collision energy distributions of O with CH_4 in the center-of-mass reference frame. The nominal collision energy (E_{coll}) was varied by adjusting the oxygen-atom beam velocity through the synchronization between the chopper wheel and the oxygen-atom beam pulse. Time-of-flight distributions were also used to derive relative fluxes of scattered products ($flux(\Theta) \propto \Sigma N(\Theta, t)/t$), where Θ is the laboratory detector angle with respect to the oxygen-atom beam. These distributions were collected with a detector angle in the range 4° to 7°. (Recall that the positive detector rotation direction goes from the oxygen-atom beam, which is defined as $\Theta = 0°$, toward the CH_4 beam.). The entire angular range over which scattered OCH_3 products could possibly be detected in the laboratory reference frame was ~10° to ~15°, depending on the oxygen-atom velocity; however, the effective angular range was always much less than 10°, because the average fraction of the available energy that went into translation for the $O(^3P) + CH_4 \rightarrow OCH_3 + H$ reaction was approximately 40-50 percent,[2] thus concentrating the OCH_3 products near the center-of-mass direction in the laboratory frame. Therefore, given the concentration of the scattered OCH_3 products over a small angular range and the detector viewing angle of ~2°, a measurement of scattered OCH_3 flux as a function of center-of-mass collision energy should closely mirror the excitation function for the title reaction. Ten center-of-mass collision energy distributions were used to study the energy dependence of the reaction of $O(^3P)$ with CH_4. An effort was made to collect data at a laboratory angle that corresponded to the direction of the center-of-mass velocity vector of the colliding reactants. Thus, for each collision energy, the detector angle was adjusted slightly (usually a fraction of a degree), because the direction of the center-of-mass velocity vector in the laboratory frame depends on the beam velocities.

Results and Analysis

Figure 5.3 shows representative TOF distributions that indicate the existence of the $O(^3P)$ + $CH_4 \rightarrow OCH_3$ + H reaction pathway. Although O_2 is present in the beam and may be thought to lead to the signal observed, calculations by Schatz *et al.* have shown that O_2 reactions with CH_4 have cross sections only a few percent that of the reaction with $O(^3P)$ and therefore the experimental signal observed reflects reactions of CH_4 with $O(^3P)$ and not O_2. These data in Fig. 5.3 were collected at the center-of-mass angle (6.5°) for O + CH_4 collisions with $E_{coll} = 67$ kcal mol^{-1}. The observed ionizer fragmentation pattern suggests that a significant fraction of the OCH_3 products are formed with enough internal energy to dissociate to OCH_2 + H or to isomerize to CH_2OH. This conclusion is also supported by the calculations of Schatz *et al.*[1] who found that (1) a concerted reaction to form OCH_2 + 2H directly is highly improbable and (2) the nascent OCH_3 products retain a large fraction of the available energy. The small signal seen at a mass-to-charge ratio (*m/z*) of 31 suggests the presence of CH_2OH, because the OCH_3^+ ion is not stable but the CH_2OH^+ ion is stable.[8,9] Ionizer fragments, *m/z* = 28, 29, and 30 are expected for electron bombardment ionization of the OCH_3 radical, but the observed fragmentation pattern differs from that reported earlier.[9] The ratio of signals detected at *m/z* = 29 and 30 suggest the presence of a species that has a higher propensity to form OCH_2^+ than does OCH_3. Secondary dissociation of nascent OCH_3 on the way to the ionizer could produce OCH_2, which would lead to large ion signals at both *m/z* = 30 (OCH_2^+) and 29 (CHO^+),[10] while the dominant ion signal from OCH_3 should be seen at *m/z* = 29. Using published fragmentation patterns for OCH_2, OCH_3, and CH_2OH, we estimate from our data that the relative yields of these three species in our experiment at $E_{coll} = 67$ kcal mol^{-1} are 0.73:0.22:0.05. This result must be considered very approximate, because it is dependent on ionizer fragmentation patterns that were obtained under different ionizer conditions and with species whose internal energies probably differ from those in the present experiment.

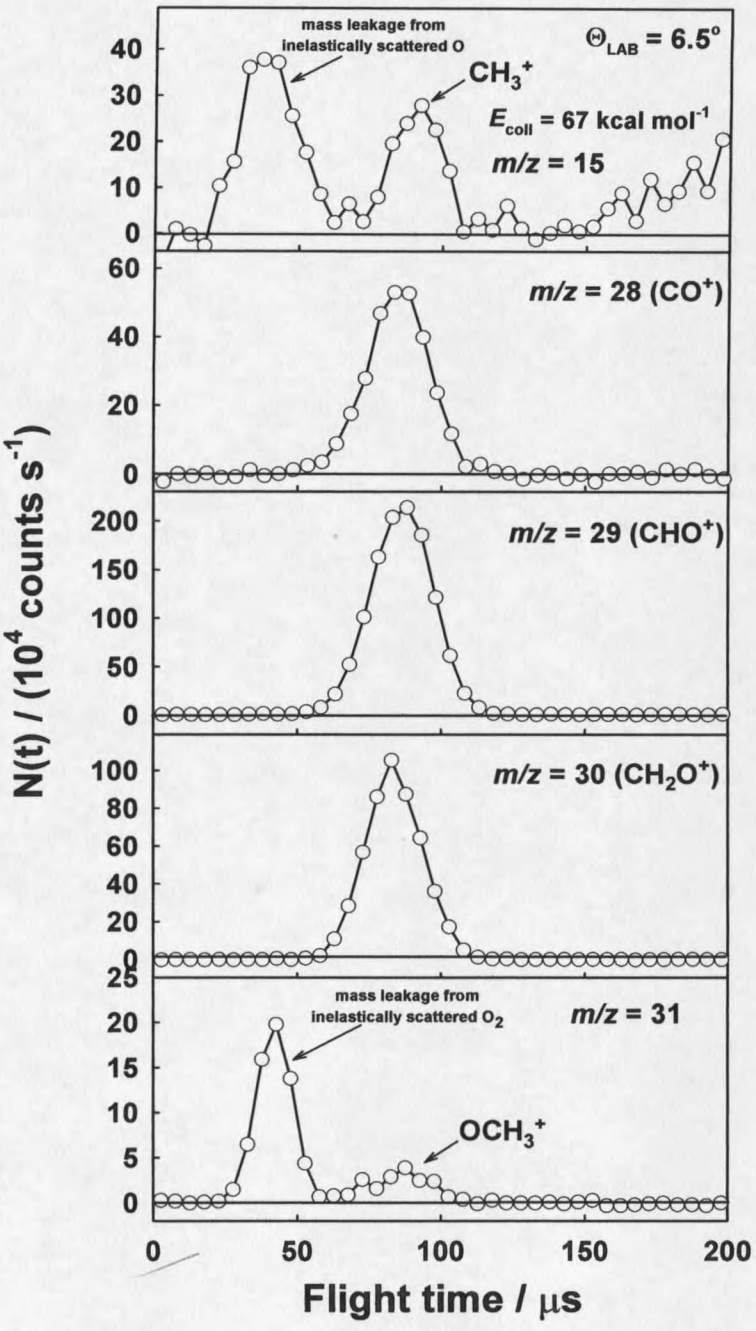

Figure 5.3. Time-of-flight distributions collected at five different mass-to-charge ratios that indicate the formation of oxygen-containing products from the reaction of $O(^3P)$ with CH_4. The center-of-mass collision energy, E_{coll}, was 67 kcal mol^{-1}, and the detector angle was aligned with the velocity vector of the center-of-mass: Θ_{LAB} = 6.5° with respect to the direction of the hyperthermal oxygen atom beam. A solid line is used to connect the data points.

Nevertheless, we can conclude that secondary dissociation of nascent OCH_3 to OCH_2 is a likely process, while isomerization to CH_2OH is not. This can be understood in terms of the barrier heights for both processes. Calculations by Walch[11] and by Harding and coworkers[12] have shown that the barrier height for the hydrogen-atom elimination process from OCH_3 yielding OCH_2+H is about 5 kcal mol^{-1} lower than that for OCH_3 isomerization to CH_2OH. The barrier height for the $OCH_3 \rightarrow H_2CO + H$ process was reported to be 23.3 [25.1] kcal mol^{-1} at the MR-CCI+Q/cc-pVTZ // CASSCF/DZP[10] [CCSD(T)/aug-cc-pVTZ // CCSD(T)/ cc-pVDZ[11]] levels, while that for $OCH_3 \rightarrow CH_2OH$ is 30.2 [30.0] kcal mol^{-1} at the same levels of theory.

The $m/z = 29$ signal was much larger than the signals detected at other mass-to-charge ratios, so we chose to focus on the $m/z = 29$ signal in order to determine an experimental excitation function for the title reaction. Even though a significant fraction of the $m/z = 29$ signal must be the result of secondary dissociation of the primary OCH_3 product, this signal will still reflect the formation of OCH_3. Secondary dissociation will produce OCH_2 that is recoiling very slowly from the light hydrogen-atom counter fragment. Therefore, both the primary OCH_3 products and the secondary OCH_2 products will travel with roughly the same directions and velocities toward the detector, and both will be detected at $m/z = 29$. The $m/z = 29$ signal intensity will thus reflect the relative probability of primary OCH_3 formation. The signals at $m/z = 15$ (CH_3^+) should, presumably, come only from the OCH_3 product and might be expected to be preferable for the determination of the relative probability of OCH_3 production. However, the $m/z = 15$ TOF distributions exhibited low signals and poor signal-to-noise ratios, especially for lower collision energies, and they proved unsuitable for an accurate determination of the excitation function. Signals were also observed at $m/z = 12$ (C^+), 13 (CH^+), and 14 (CH_2^+), and based on the shape of the distribution and arrival time to the detector are believed to originate from the OCH_3 radical. The signals at these masses, like the $m/z = 15$ signal were, however, very low.

Figure 5.4 shows TOF distributions collected at $m/z = 16$ and 29, corresponding to ten different center-of-mass collision energies, ranging from 39.2 to 76.0 kcal mol^{-1}. The signal intensities of the scattered products varied with center-of-mass collision energy in part because the corresponding oxygen-atom flux in the hyperthermal beam varied. The incident oxygen-atom flux was proportional to the intensity of the oxygen-atom inelastic scattering signal. In order to obtain the dependence of the scattered OCH_3 flux (proportional to the $m/z = 29$ signal) on collision energy, the integrated fluxes derived from the $m/z = 29$ TOF distributions were divided by the corresponding integrated oxygen-atom fluxes, which were derived from the TOF distributions collected at $m/z = 16$.[13] The relative flux of OCH_3, corrected for the incident oxygen-atom intensity, is shown as a function of center-of-mass collision energy in Fig. 5.5. The curve resulting from connecting the ten data points represents the relative excitation function for the title reaction.[14] The energy threshold for the reaction appears to be between 43.8 and 46.1 kcal mol^{-1}. Because the data only provide relative values, the experimental excitation function may be normalized somewhat arbitrarily.

Discussion

Concurrent with the experimental efforts described above, electronic structure and dynamics calculations were carried out by Schatz *et al.* An overview of this work will be presented here; however, a detailed treatment of the theoretical work on $O(^3P) + CH_4$ at high collision energies may be found in Ref. 1. Using several different levels of theory (the highest being CCSD(T)/AUG-cc-pVTZ), OCH_3 was found to be generated by two distinct reaction mechanisms, each of which has an identified saddle point. Structures of the two saddle points are shown in Fig. 5.6. The lower-energy saddle point, with an energy of about 47 kcal mol^{-1} and referred to as TS1, corresponds to a structure in which the exiting hydrogen atom is located in a near collinear arrangement with respect to the C and incoming O atom. In the

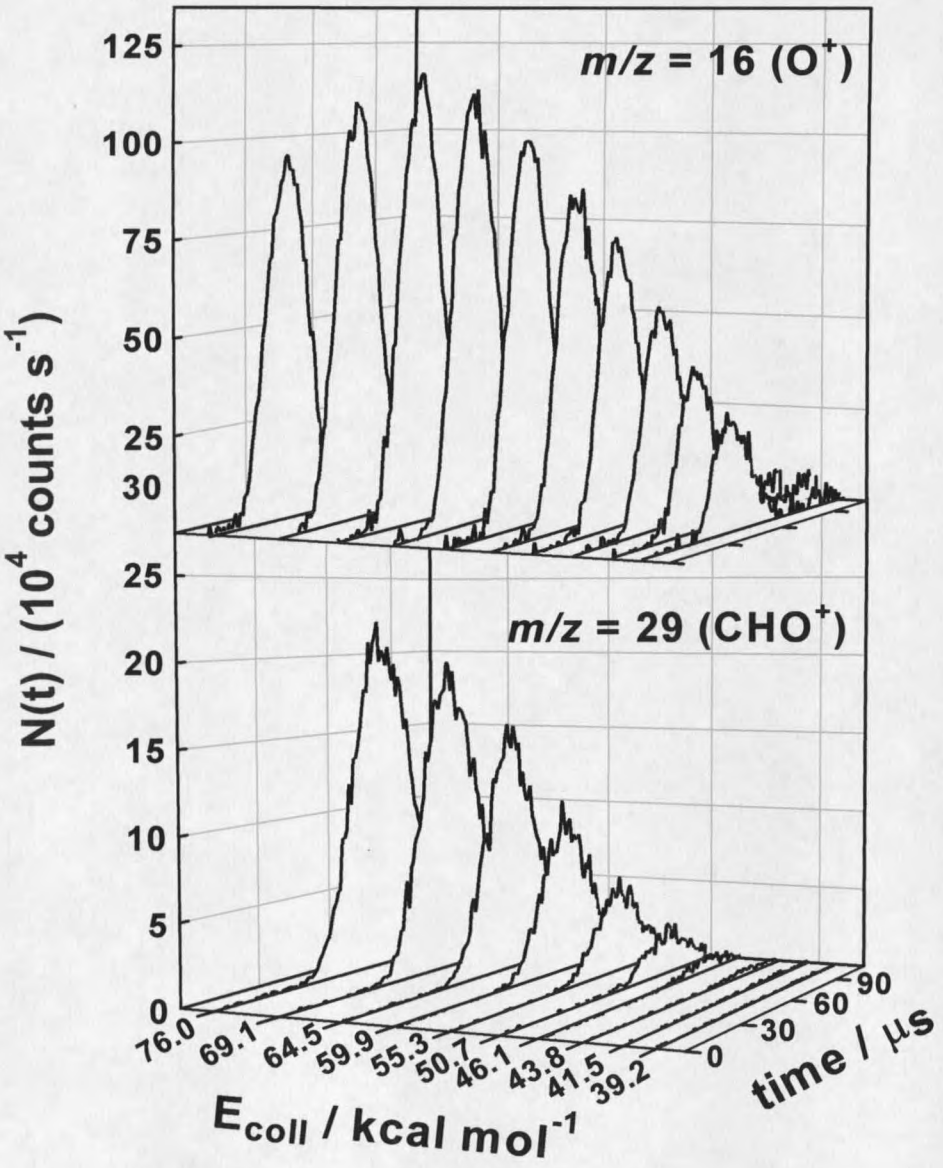

Figure 5.4. Time-of-flight (TOF) distributions of inelastically scattered O (top) and reactively scattered OCH_3 (bottom; detected at m/z=29), collected with the detector angle adjusted to coincide with the direction of the center-of-mass velocity vector, which ranged from 4 to 7° with respect to the oxygen-atom beam direction. Ten TOF distributions were collected for both products, corresponding to ten different center-of-mass collision energies, E_{coll}. Time zero in these distributions corresponds to the nominal time at which the oxygen-atom beam pulse intersected the CH_4 beam pulse.

higher-energy saddle point or TS2 (~59 kcal mol^{-1}), the O–C–H configuration (where H is the atom being eliminated) forms a nearly perpendicular angle. Saddle point energies were calculated using ROHF and UHF MSINDO Hamiltonians and were found to be above and below, respectively, the CCSD(T) calculated value for TS1, and therefore calculated UHF and ROHF MSINDO reaction thresholds were expected to be, respectively, lower and higher bounds to the threshold expected from the CCSD(T) calculations. Based on the reaction barrier estimates from the MSINDO Hamiltonian, direct dynamics calculations were run to determine cross sections at several different collision energies. In addition to the ground-state triplet surface (1^3A), the surface for which the barrier calculations were performed, excitation function calculations for the first excited triplet surface (2^3A) were also performed, as it is believed to contribute to the reactive process.

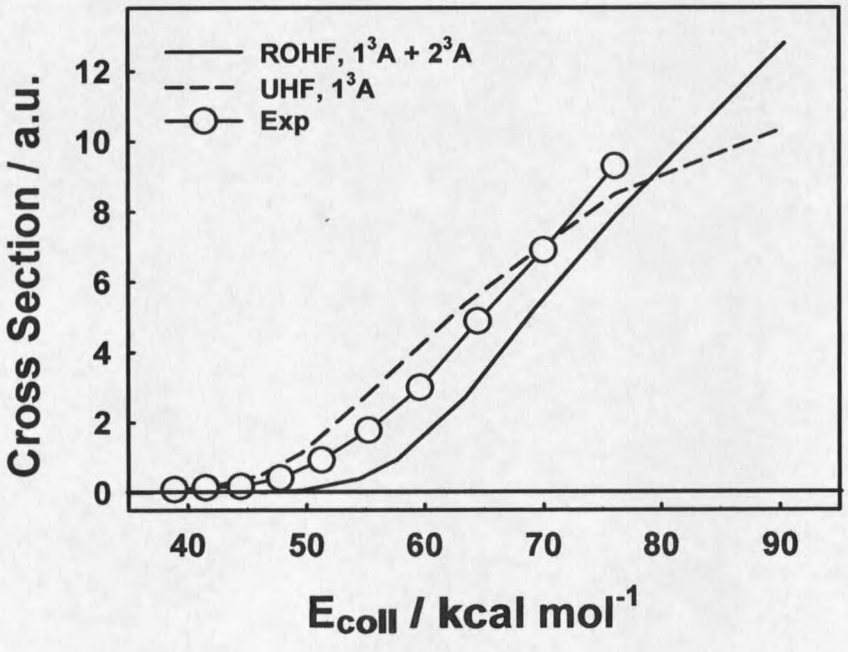

Figure 5.5. Experimental and calculated excitation functions (cross section vs. collision energy) for the $O(^3P) + CH_4 \rightarrow OCH_3 + H$ reaction. Circles connected with a dotted line drawn as a guide show experimental results. The solid line is for the ROHF MSINDO $1^3A + 2^3A$ cross sections and the dashed line is for the UHF MSINDO 1^3A cross sections.

The resulting calculated excitation functions are shown in Fig. 5.5, which also shows the comparison between measured and calculated excitation functions. The normalization of the experimental curve in Fig. 5.5 shows that the shape of this curve matches the ROHF MSINDO ($1^3A + 2^3A$) calculated excitation function almost exactly, although the ROHF curve appears shifted to higher energy by ~7.5 kcal mol^{-1}. Both the experimental threshold and the cross sections for collision energies slightly above threshold are clearly between the UHF (1^3A) and ROHF MSINDO ($1^3A + 2^3A$) cross sections, which indicates that the experimental threshold is between the UHF and ROHF MSINDO barriers. The most accurate calculation of the barrier height carried out by Schatz *et al.*, (CCSD(T)/AUG-cc-pVTZ), was midway between the UHF and ROHF MSINDO barrier heights, and therefore is in excellent agreement with the measured threshold of ~45 kcal mol^{-1}.

At energies above threshold, we see in Fig. 5.5 that the experiments are in better agreement with the ROHF MSINDO cross sections that include contributions from the ground and lowest excited triplet surface than with the ground state only UHF MSINDO cross sections. The contribution of the 2^3A surface clearly makes the calculated cross section increase with collision energy at the same rate as the experiments for high energy. On the other hand, neglect of this excited surface makes the UHF MSINDO cross section increase too slowly, thereby cutting through the experimental curve. Therefore, the 2^3A surface must be accounted for in the calculations in order to satisfactorily reproduce experiment. It should also be noted that the cross sections obtained in the crossed-beams experiments reported here are not absolute cross sections, and need to be calibrated. The calibration method has been to best match the calculations. Therefore, although there is always uncertainty in the absolute values of the cross sections, the trends should be correct, and all statements about the involvement of excited surface should apply.

Another important point that can be inferred from the results in Fig. 5.5 is the importance of intersystem crossing from the initial triplet state to singlet states that also correlate to the $H + OCH_3$ products. It is well-known that triplet-singlet crossings can occur in reactions involving $O(^3P)$ atoms colliding with closed-shell species, however the importance of this process likely varies significantly with the target molecule. One of the best studied of these systems, from a theoretical perspective, is $O(^3P) + H_2$ where very detailed information about the intersystem crossing exists,[2,15] and intersystem crossing is found to be a relatively small (few percent) effect. However intersystem crossing is likely the dominant reaction mechanism for the $O(^3P) + CH_3I$ reaction based on molecular beam observations.[16]

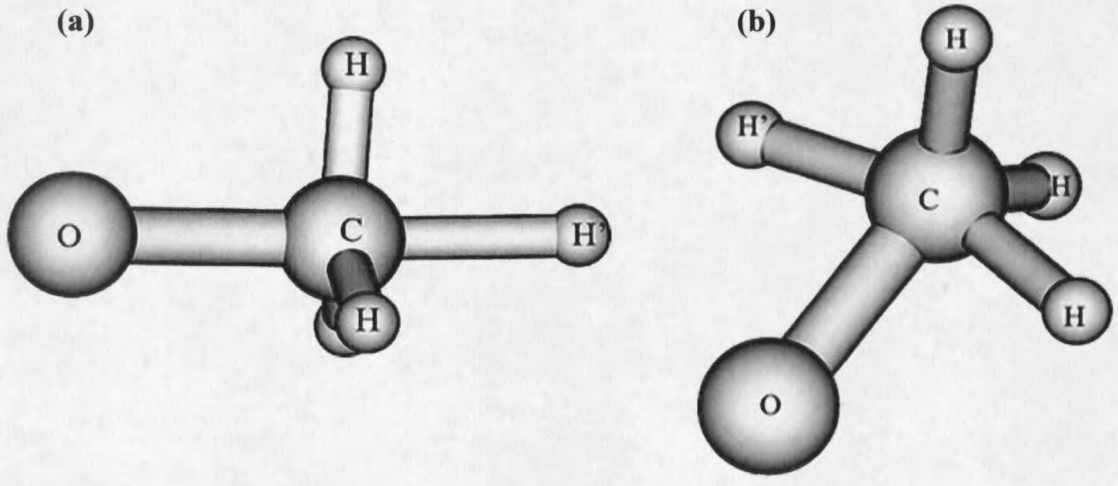

Figure 5.6. Saddle point structures associated with the $O(^3P) + CH_4 \rightarrow OCH_3 + H$ reaction. (a) TS1, lower-energy structure. (b) TS2, higher-energy structure.

Calculations by Schatz *et al.* suggest that triplet-singlet intersystem crossing is possible on the TS2 potential since there are singlet crossing points below the TS1 and TS2 barriers for reaction. If hopping occurred from the triplet to singlet surface at the point of intersection, the system would evolve to products without surmounting any subsequent barrier since hydrogen atom elimination on the singlet surface proceeds without a barrier and the observed reaction threshold would be that of the lowest energy crossing between the triplet and singlet surfaces. The presence of crossings well below the triplet barrier would therefore lead to a significant cross sections for energies below the triplet reaction barrier, but in the experiments, no signal is observed for the OCH_3 product below the predicted barrier. Therefore, although triplet-singlet intersystem crossing undoubtedly does take place, the coupling must be small enough to make transitions from triplet to singlet states before the barrier negligible. This conclusion that cleanly stems from the experimental results is to be contrasted with the reactivity of $O(^3P)$ species with cyclohexane clusters where addition reactions are believed to play an important role even at thermal collision energies.[17]

Conclusion

The $O(^3P) + CH_4 \rightarrow H + OCH_3$ excitation function was measured in a crossed-beams experiment and compared with direct dynamics quasiclassical trajectory results. The experimental measurement of the barrier for OCH_3 formation was ~45 kcal mol^{-1}. The shape of the experimental excitation function can only be reproduced when the ground and first excited state triplet surfaces are included in the calculations. Theoretical excitation functions are shifted from the experimental excitation function by an energy that would indicate an accurate description of the reaction barrier height by means of CCSD(T)/AUG-cc-pVTZ calculations. Calculations show that intersystem crossings between triplet and singlet surfaces can occur at energies substantially below the reaction barrier, however, the experiments indicate

an absence of reactivity at energies below the lowest energy saddle point on the triplet surfaces, suggesting only a negligible contribution of intersystem crossing to the reaction cross sections. Formation of OCH_3, CH_2OH and OCH_2 was seen in both experiment and theory. The nascent product is mostly OCH_3, which has enough excess energy either to isomerize to CH_2OH or to dissociate to $OCH_2 + H$, with the latter being greatly favored.

References

1. D. Troya, R. Z. Pascual, and G. C. Schatz, *J. Phys. Chem.* **107**, 10497 (2003).

2. T. Suzuki and E. Hirota, *J. Chem. Phys.* **98**, 2387 (1993).

3. G. M. Sweeney, A. Watson, and K. G. McKendrick, *J. Chem. Phys.* **106**, 9172 (1997).

4. A. C. Luntz and P. Andresen, *J. Chem. Phys.* **72**, 5851 (1980); P. Andresen and A. C. Luntz, *J. Chem. Phys.* **72**, 5842 (1980).

5. F. Ausfelder and K. G. McKendrick, *Prog. React. Kinetc. Mech.* **25**, 299 (2000).

6. X. Liu and A. G. Suits, "The Dynamics of Hydrogen Atom Abstraction From Polyatomic Molecules," in *New Directions in Reaction Dynamics*, Eds. K. Liu and X. Yang (World Scientific, Singapore) to be published.

7. D. J. Garton, T. K. Minton, D. Troya, R. Pascual, and G. C. Schatz, *J. Phys. Chem. A* **107**, 4583 (2003).

8. A. M. Wodtke, Ph.D. Thesis, University of California, Berkeley, 1986.

9. J. J. Lin, Y. T. Lee, and X. Yang, *J. Chem. Phys.* **109**, 2975 (1998).

10. NIST Chemistry WebBook, http://webbook.nist.gov/chemistry.

11. S. P. Walch, *J. Chem. Phys.* **98**, 3076 (1992).

12. T. P. Marcy, R. R. Diaz, D. Heard, S. R. Leone, L. B. Harding, and S. J. Klippenstein, *J. Phys. Chem. A* **105**, 8361 (2001).

13. The $m/z = 16$ time-of-flight distributions were corrected by subtracting the O_2 component that fragments to $m/z = 16$ in the ionizer (11% of the signal intensity detected at $m/z = 32$), thus yielding time-of-flight distributions that represent scattering of O atoms only.

14. A variation in the ionizer fragmentation patterns of primary OCH_3 and secondary OCH_2 products would introduce an error in the shape of the experimental excitation function. However, such an error is mitigated by the fact that both OCH_3 and OCH_2 fragment mostly to $m/z = 29$. Therefore, we expect the excitation function derived from the experiment to be a faithful representation of the "true" excitation function.

15. M. R. Hoffmann and G. C. Schatz, *J. Chem. Phys.* **113**, 9456 (2000).

16. M. Alagia, N. Balucani, L. Cartechini, P. Casavecchia, M. van Beek, G. G. Volpi, L. Bonnet, and J. C. Rayez, *Faraday Discuss.* **113**, 133 (1999).

17. Y. Rudlich, Y. Hurwitz, S. Lifson, and R. Naaman, *J. Chem. Phys.* **98**, 2936 (1993).

INELASTIC AND REACTIVE SCATTERING DYNAMICS OF $O(^3P)$ COLLISIONS WITH CH_4 AND CD_4

Introduction

In the previous chapter, the experimental excitation function for the reaction, $O(^3P) + CH_4 \rightarrow H + OCH_3$, was presented and compared with the results of direct dynamics calculations. The excitation function is one important piece of the puzzle in understanding the details of the reaction of hyperthermal $O(^3P)$ with CH_4 and gives valuable information about the lack of intersystem crossing in the OCH_3 formation channel. Furthermore, it provides input into how well theoretical methods describe real reactive events. A more complete description of how reactions between $O(^3P)$ and CH_4 proceed can be obtained by further probing the scattering dynamics of the various possible reactions. Dynamical information provides an understanding of how products formed in a collision scatter from each other, how energy is partitioned during the reactive collision, as well as an estimation of the relative yield of each product channel.

Prior to the research described in this thesis, the only experimentally observed reaction through which $O(^3P)$ reacts with CH_4 was hydrogen atom abstraction to form OH.[1,2] The dynamics of hydrogen abstraction from alkanes have been studied in some detail because of the fairly low barriers to reaction, 7, 4.5, and 3.3 kcal mol^{-1} for primary, secondary, and tertiary hydrogen atoms, respectively,[3] which can be surmounted using relatively low translational energy $O(^3P)$ atoms produced by photodissociation of NO_2 and SO_2[1,2] or by a microwave discharge source.[3,4] An early study by Walch and Dunning suggested that the $O(^3P) + CH_4$ reaction proceeds through a collinear O-H-CH_3 intermediate.[5] Simultaneous to that study, Andresen and Luntz[3,6] proposed that the transition state in all reactions of $O(^3P)$

with hydrocarbons has a collinear O–H–R geometry, where R is any alkyl fragment. Luntz and Andresen proceeded to develop a triatomic model for the generic reaction of $O(^3P)$ + HR where the hydrocarbon radical, R, was considered to be a structureless particle, and the dynamics were dominated by the $O(^3P)$ interaction with the C–H bond.[6] Assuming a collinear transition state,[5-7] the line-of-centers model[8] can be used to understand many experimental results on the dynamics of $O(^3P)$ and analogous $Cl(^2P)$ reactions with alkanes at different collision energies.[9,10] In the line-of-centers model, if there is enough energy along the reaction coordinate to overcome the barrier to reaction, the reaction will proceed.[8] At collision energies near the barrier to reaction, as in experiments that have been done on $O(^3P) + CH_4$,[1,2] the line-of-centers model predicts that there must be a relatively low impact parameter collision (a "head-on" collision between the $O(^3P)$ and the alkane), where there is enough energy along the O–H–R reaction coordinate for the barrier to be surmounted and the reaction to occur. The resulting OH distributions in these low collision energy experiments are backwards scattered, indicating a small impact parameter collisions. In the reaction of $O(^3P)$ with methane at low collision energies, McKendrick *et al.* found very cold vibrational and rotational distributions in the OH product.[2] Using laser induced fluorescence, they were unable to detect vibrational states above the ground state, and rotational distributions were similar for all alkanes studied, having a peak around j = 0 or 1 and a maximum at j = 10. Blank and coworkers observed this trend in reactions of Cl with propane, which also has a collinear transition state similar to that of the $O(^3P)$ reactions.[10] At low collision energies, the HCl product was mostly backwards/sideways scattered; however, as the collision energy was increased, the HCl product began to show a peak in the forward scattering direction. They suggested the onset of a stripping mechanism at high collision energy which occurs through larger impact parameter ("glancing") collisions. The proposed stripping mechanism is a natural outcome of the line-of-centers model, because as the collision energy is increased,

the "cone of acceptance", or the number of impact parameters that have sufficient energy along the line-of-centers to lead to reaction, will increase. The HCl products scattered in the forward direction were believed to be vibrationally cold based on previous studies by Varley and Dagdigian,[11] which reinforces the assumption of a weak interaction between the reactants. This stripping mechanism was also observed by Kajimoto *et al.* in reactions of $O(^3P)$ with larger alkanes[9] and by Zare *et al.* in reactions of $Cl(^2P)$ with vibrationally excited methane.[12] In the reaction of $O(^3P)$ with methane, however, the stripping mechanism has never been observed experimentally.

While there is considerable information on the dynamics of OH formation in reactions of $O(^3P)$ with CH_4, there have been no experiments and only one series of calculations by Schatz *et al.* that have examined the hydrogen elimination channel to form $OCH_3 + H$.[13] As discussed in the previous chapter, the lack of experimental observation of this channel is due to the high collision energy (large relative translational energies) required to overcome the considerable ~45 kcal mol^{-1} reaction barrier.

In this chapter, product channels observed in the reaction of hyperthermal $O(^3P)$ with CH_4 and their associated dynamics are explored, and relative product yields are obtained. Reactions of $O(^3P)$ with CH_4 and CD_4 were investigated. The hydrogen-atom abstraction channel (OH formation) and the relative product yields were obtained for the reaction of $O(^3P)$ with CH_4. The necessity of deuterated methane arises because of the unfavorable kinematics of the hydrogen-atom elimination channel (OCH_3 formation). As mentioned in Chapter 5, the small recoil velocities of the OCH_3 (i.e., size of the Newton circle), while favorable for obtaining the excitation function, severely limit the angular and velocity resolution when probing dynamical properties of the reaction, $O(^3P) + CH_4 \rightarrow H + OCH_3$. A larger Newton circle is obtained for this channel when $O(^3P)$ reacts with CD_4, because (1) the velocity of OCD_3 recoiling from a D atom is larger than the velocity of OCH_3 recoiling from

an H atom and (2) the collision energy is higher as a result of a larger reduced mass (see Figs. 6.1 and 6.2). The slightly larger Newton circle, which is expected to give a wider lab angular and velocity range into which the OCD_3 products will scatter, makes it possible, in principle, to extract more information on the dynamics of the hydrogen elimination reaction.

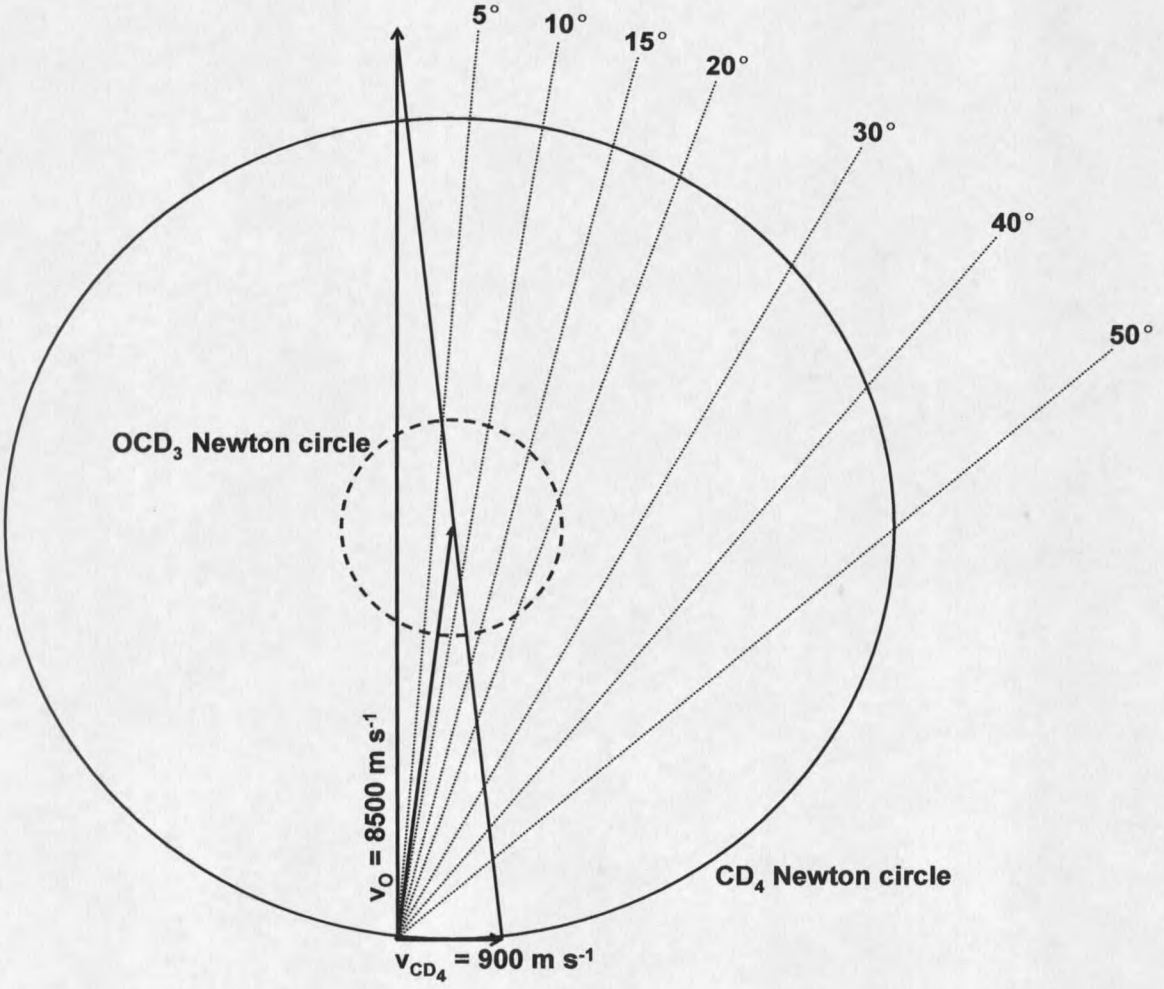

Figure 6.1. A Newton diagram for the reaction of $O(^3P)$ with CD_4 at E_{coll} = 78 kcal mol^{-1}. The smaller circle (dashed) represents the maximum recoil velocity of the OCD_3 fragment given the energy available for the reaction, $O(^3P) + CD_4 \rightarrow OCD_3 + D$. The larger Newton circle (solid) is the maximum recoil velocity of CD_4 scattering inelastically from $O(^3P)$. The available energy in the inelastic scattering of CD_4 is equal to the collision energy.

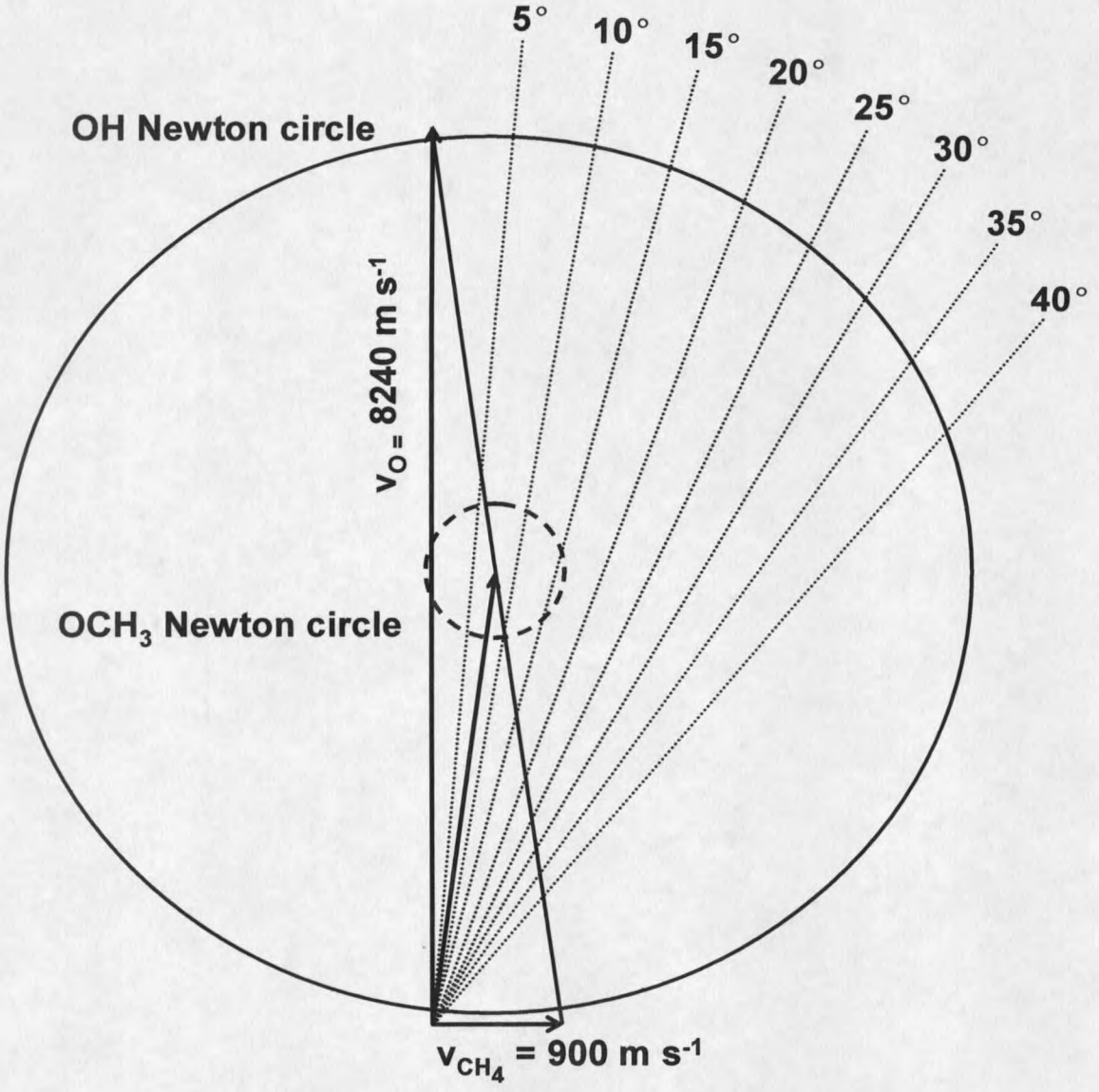

Figure 6.2. A Newton diagram showing the OH + CH_3 and H + OCH_3 channels of the O(^3P) + CH_4 reacton at E_{coll} = 67 kcal mol^{-1}. The dotted lines represent the laboratory angles for which data were collected. The smaller circle (dashed) represents the maximum recoil velocity of the OCH_3 fragment given the energy available for the reaction, O(^3P) + CH_4 → OCH_3 + H. The larger Newton circle (solid) is the maximum recoil velocity of reactively scattered OH from reaction of CH_4 with O(^3P).

In addition to the hydrogen atom abstraction and elimination reactive channels of $O(^3P)$ + CH_4, the inelastic scattering dynamics of CD_4 from $O(^3P)$ and the possible reactions involving O_2, which is a component in the hyperthermal oxygen beam, are investigated.

Experimental Details

Experiments were performed with the use of the crossed molecular beams apparatus described in Chapter 2. Pulsed beams of neat CH_4 and CD_4 traveling at ~0.9 km s^{-1} were created using a piezoelectric pulsed valve. The pressure behind the nozzle of the pulsed valve was held at 60 psig. The pulsed beam passed through a 2 mm skimmer into a differential pumping region and then exited into the main scattering chamber (held at ~10^{-7} torr) through a 2.5 mm diameter aperture. No dimers or larger clusters were detected in the methane beams. The CH_4 and CD_4 beams were crossed with a pulsed beam containing ~70 percent ground-state oxygen atoms created from the laser detonation source. In all of the experiments, the oxygen-atom beam passed through two 2 mm diameter skimmers before reaching the main scattering chamber and was velocity selected using a synchronized, 17.8 mm diameter, chopper wheel rotating at 400 Hz. The nominal velocity of the oxygen-atom beam used to study the $O(^3P)$ reaction with CH_4 was 8.24 km s^{-1}, corresponding to a collision energy of 67 kcal mol^{-1}. Three different oxygen-atom beam nominal velocities were used to study to the reaction of $O(^3P)$ with CD_4: 8.24 km s^{-1} (E_{coll} = 73 kcal mol^{-1}), 8.42 km s^{-1} (E_{coll} = 76 kcal mol^{-1}), and 8.55 km s^{-1} (E_{coll} = 78 kcal mol^{-1}). The velocity width (FWHM) of the all of the oxygen-atom beams was ~440 m s^{-1}. The fraction of O_2 in the beams ranged from 20 to 40 percent, depending on beam conditions. Products scattering from the crossing point of the beams traveled 33.7 cm where they entered the Brink-type ionizer (held at ~10^{-12} torr). Species that were ionized (approximately 1 in 10^5) were then mass selected with a quadrupole mass filter and counted.

For the reaction of $O(^3P)$ with CH_4, signal was observed and time-of-flight (TOF) distributions were collected for a mass-to-charge ratio (*m/z*) of 17 (OH^+) in 2.5° increments from 5° to 25° and 5° increments from 25° to 45°. No signal was observed at *m/z* = 18 (H_2O^+). Reactive signals originating from the OCH_3 radical were also observed at *m/z* = 12 (C^+), 13 (CH^+), 14 (CH_2^+), 15 (CH_3^+), 28 (CO^+), 29 (CHO^+), 30 (OCH_2^+), and 31 (OCH_3^+). Analogous products and corresponding ionizer fragments were observed in the O + CD_4 reaction, with the addition of a signal detected at *m/z* = 20, which was determined to be CD_4^+ arising from inelastic scattering of CD_4 from O. There was no detectable signal at *m/z* = 12 (C^+). Time-of-flight distributions were collected at *m/z* = 20 (CD_4^+) in 10° increments from 10° to 50° and at *m/z* = 30 (CDO^+) in 2° increments from 5° to 19°.

Results and Analysis

$O(^3P) + CH_4$

Formation of the OH radical has been observed in the reaction of hyperthermal $O(^3P)$ with CH_4. The OH product scatters with large c.m. velocities (see Fig. 6.2), resulting in relatively low signal levels. Representative TOF distributions collected at six different lab angles for *m/z* = 17 (OH^+) with E_{coll} = 67 kcal mol^{-1} are shown in Fig. 6.3. The solid-line curves come from a simulation of the data using optimized center-of-mass (c.m.) angular and translational energy distributions (see Figs. 6.5 and 6.6). The poor signal-to-noise levels in the TOF distributions at *m/z* = 17 are exacerbated by the large H_2O background in the detector. (In the detector, H_2O dissociatively ionizes to OH^+) Any possibility of the signal at *m/z* = 17 coming from mass leakage from the large inelastic scattering signal at *m/z* = 16 (O^+) was eliminated by increasing the resolution of the quadrupole mass filter until no signal was observed at *m/z* = 16.5. This high resolution operation, which was needed for unambiguous

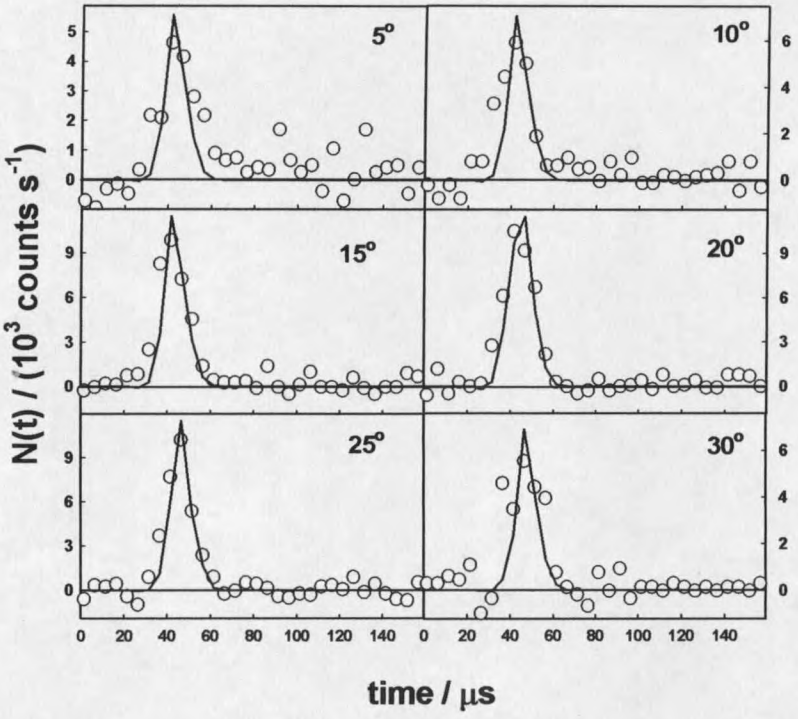

Figure 6.3. Representative time-of-flight distributions of reactively scattered OH following reaction of $O(^3P)$ with CH_4 at E_{coll} = 67 kcal mol^{-1}. The open circles are the experimental data. The solid line is the forward convolution simulation to the data derived from c.m. distributions shown in Figs. 6.5 and 6.6.

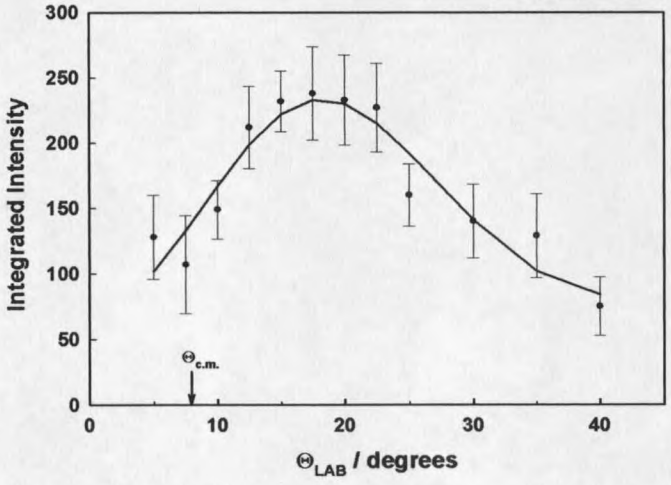

Figure 6.4. Laboratory angular distribution of the OH product from the reaction of $O(^3P)$ with CH_4. The black dots are the experimental data and the solid line is the forward convolution simulation to the data. The error bars are estimated from fitting the TOF distributions with a modified gaussian function and finding maximum and minimum acceptable fits by adjusting the gaussian parameters. The integrated range of these fits are represented by the error bars.

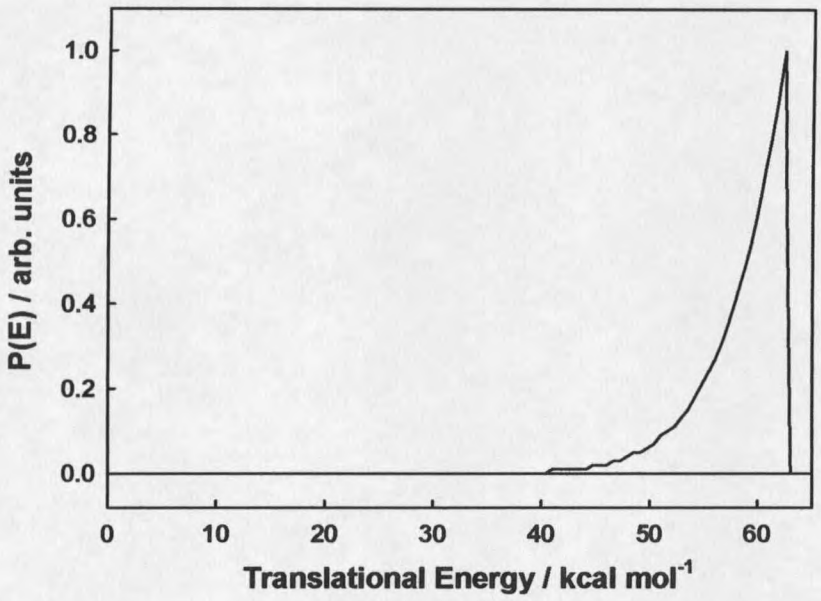

Figure 6.5. Center-of-mass translational energy distribution for the $O(^3P) + CH_4 \rightarrow OH + CH_3$ reaction at $E_{coll} = 67$ kcal mol^{-1} derived from the TOF and laboratory angular distributions for $m/z = 17$ (OH^+) through the forward convolution method.

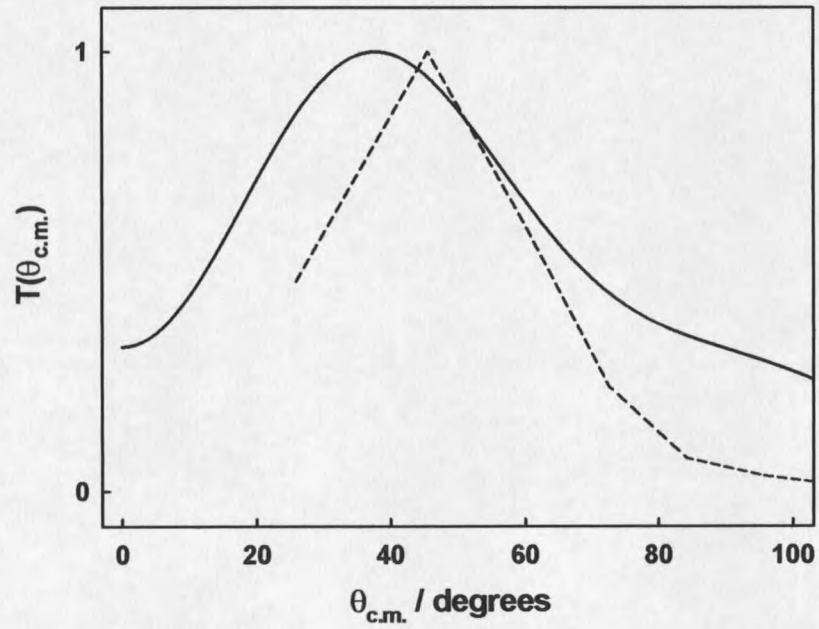

Figure 6.6. The solid line is the center-of-mass angular distribution of the OH product from the reaction of $O(^3P) + CH_4 \rightarrow OH + CH_3$ reaction at $E_{coll} = 67$ kcal mol^{-1}, derived from the TOF and laboratory angular distributions for $m/z = 17$ (OH^+) through the forward convolution method. The dashed line is the c.m. angular distribution obtained from MSINDO direct dynamics calculations at $E_{coll} = 90$ kcal mol^{-1}.

detection of OH^+, further reduced signal levels. The corresponding experimental laboratory angular distribution and calculated distribution from the forward convolution simulation of the data are shown in Fig. 6.4. From quick inspection of the angular distribution, which has a maximum at a lab angle of ~17°, it is evident that the OH radical is scattered in the forward direction (where a lab angle of 0° is defined as the direction of the oxygen atom beam), indicating a stripping mechanism for reaction.

Further evidence for a stripping mechanism can be seen in the c.m. translational energy and angular distributions, obtained from the forward convolution simulation to the data, shown in Figs. 6.5 and 6.6. The translational energy distribution has a maximum near the available energy, which is the collision energy corrected for the endoergicity of the reaction. Thus, nearly all energy available for the reaction goes to translation of the OH and CH_3 fragments, with very little imparted into internal energy. The c.m. angular distribution, although broad, shows forward-sideways scattering of the OH, with a peak in the distribution near 40°. The experimental angular distribution is in good agreement with the distribution obtained from MSINDO direct dynamics calculations by Schatz *et al.*, which has a peak near 45°. It is possible that there is some backwards scattering that we were unable to observe due to limitations in the angular range where product detection was possible, although very little backwards scattering was observed in the direct dynamics calculations. From the c.m. translational energy and angular distributions, a c.m. velocity-flux map showing the angular region for which the experiment was sensitive is shown in Fig. 6.7.

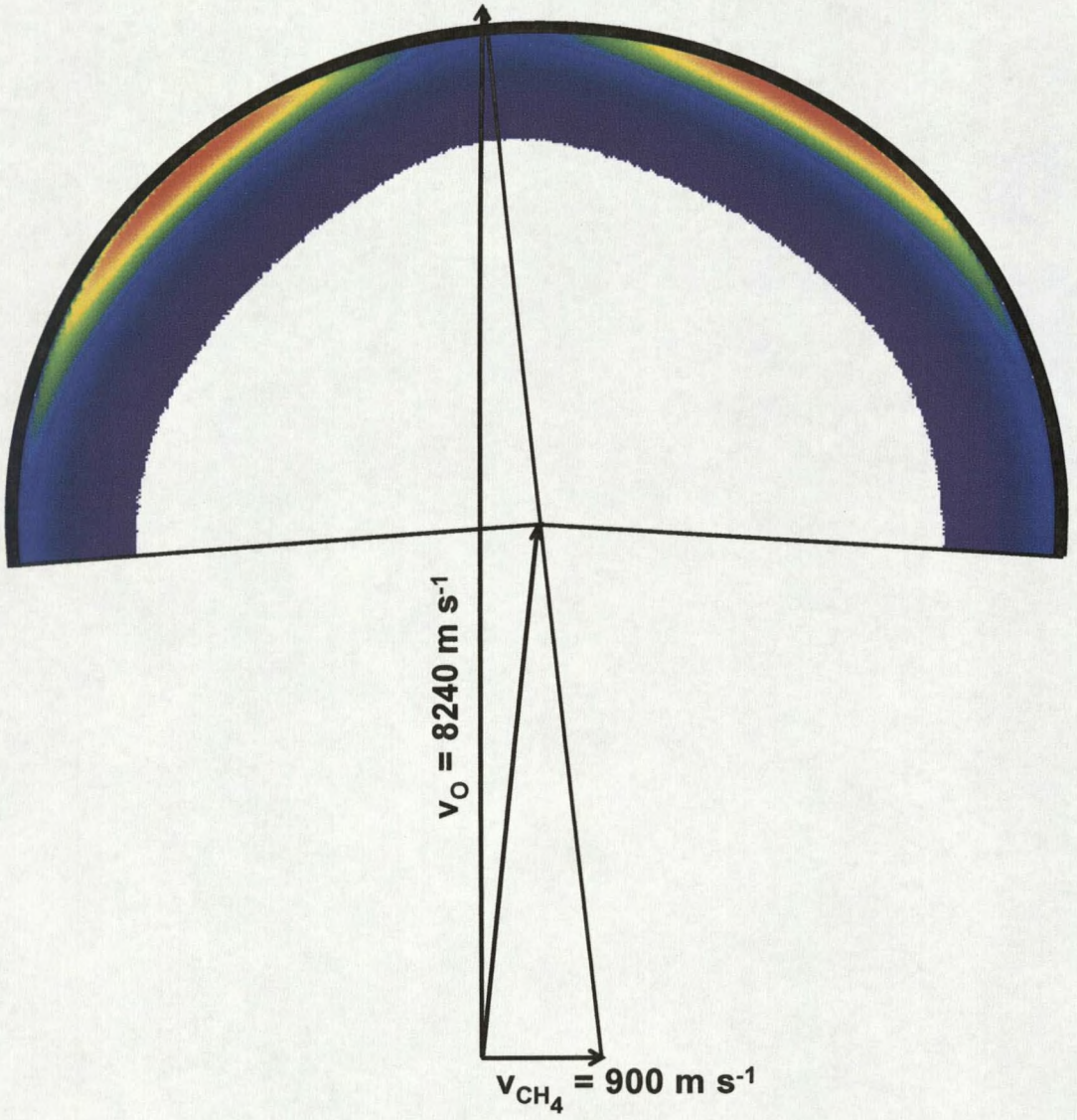

Figure 6.7. Center-of-mass velocity-flux map, superimposed on a Newton diagram, for the OH product from the reaction, $O(^3P) + CH_4 \rightarrow OH + CH_3$, at $E_{coll} = 67$ kcal mol^{-1}. Only the range of the contour plot for which the experiments are sensitive is shown.

$\underline{O(^3P) + CD_4}$

Inelastic Scattering

Inelastic scattering of CD_4 from $O(^3P)$ was also observed. We did not attempt to look for the inelastic scattering signal with $O + CH_4$ because CH_4^+ has the same mass-to-charge ratio as O^+, and the inelastic scattering of signal for CH_4 would be indistinguishable from the

oxygen atom scattering signal. With CD_4 on the other hand, the inelastic scattering signal may be detected at the CD_4^+ parent mass, $m/z = 20$, where the detector background is very low. The only other possible product that could contribute to the signal at $m/z = 20$ is D_2O. However, because of the absence of signal at $m/z = 18$ (H_2O^+) in the O + CH_4 reaction, it was possible to conclude that the $m/z = 20$ signal in CD_4 was solely from inelastic scattering. The CD_4 was found to be scattering inelastically from $O(^3P)$ and not O_2 in the beam by measuring the peak velocities of the scattered CD_4 in the laboratory frame, which defined a circle about the c.m. for the O + CD_4 collision. If the CD_4 were scattering from O_2, the CD_4 velocities would be expected to follow a Newton circle resulting from the O_2 + CD_4 interaction. We can therefore conclude that most of the detected inelastic scattering signal of CD_4 at $m/z = 20$ is from collisions of CD_4 with oxygen atoms. Time-of-flight distributions for $m/z = 20$ (CD_4^+) collected in 10° increments from 10° to 50° at a collision energy of 76 kcal mol^{-1} are shown in Figure 6.8. The laboratory angular distribution is shown in Fig. 6.9. Translational energy and angular distributions derived from the forward convolution simulation of the data are shown in Figs. 6.10 and 6.11, respectively.

The translational energy distribution has a maximum near the available energy, which is the collision energy in the case of inelastic scattering. However, there is a long tail that extends down to ~50 percent of the available energy, indicating that in some of the collisions there is a very large amount of energy transferred into internal modes of the CD_4. On average it appears as though ~10 to 20 percent of the available energy goes into internal energy of the recoiling CD_4. In the c.m. angular distribution, some of the CD_4 appears to be scattered into the forward direction relative to the CD_4 beam. The data, however, are only sensitive to the range of 0° to 100° in the c.m. frame with respect to the direction of the incident oxygen atom beam. So, while we can say that there is an increase in scattering in the forward direction, we cannot be certain about the details of the scattering in the range of 100° to 180°

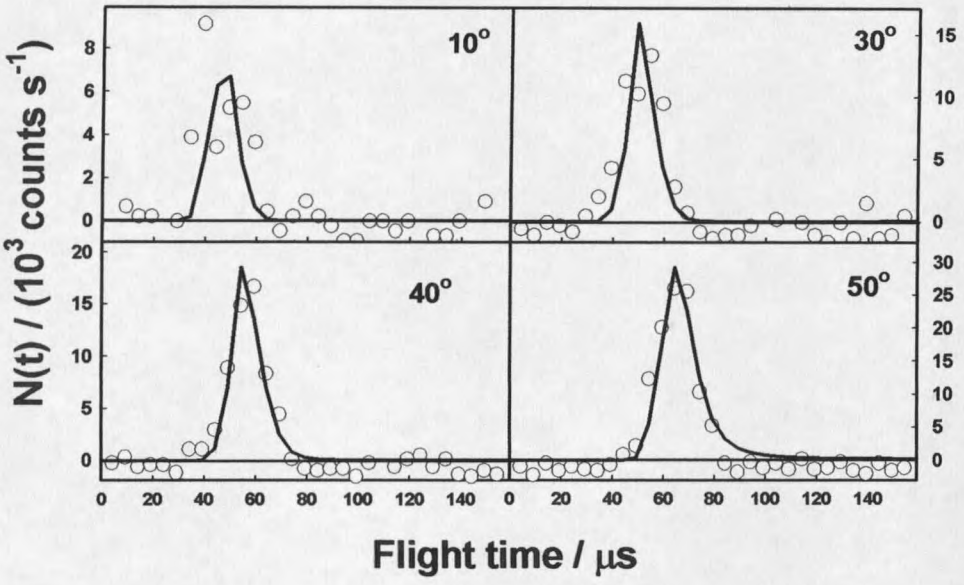

Figure 6.8. Representative time-of-flight distributions of inelastically scattered CD_4 following collisions with $O(^3P)$ at E_{coll} = 76 kcal mol^{-1}. The open circles are the experimental data. The solid line is the forward convolution simulation to the data based on c.m. angular and translational energy distributions shown in Fig. 6.10 and 6.11.

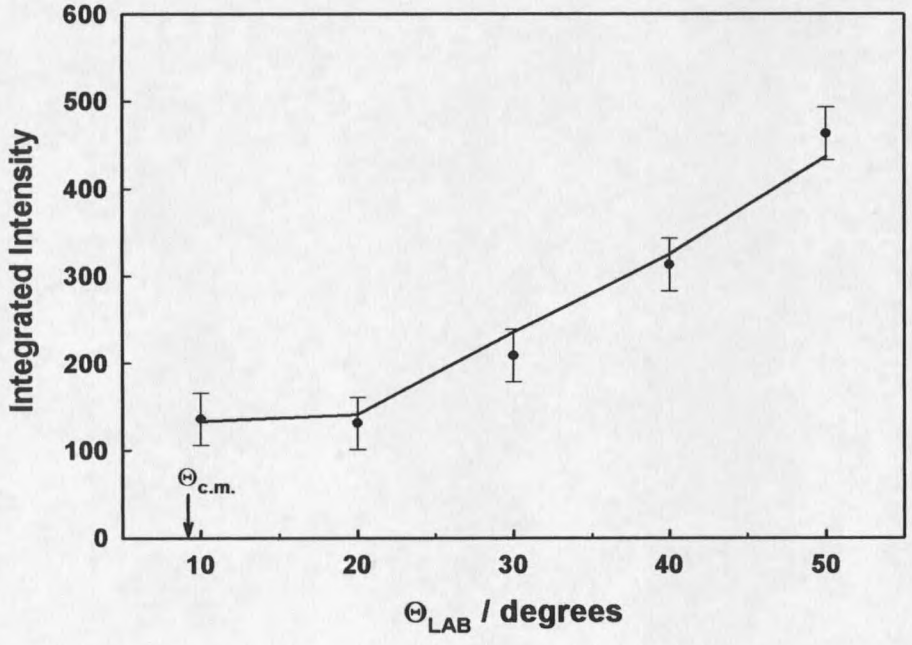

Figure 6.9. Laboratory angular distribution of CD_4 that scatters inelastically from $O(^3P)$ with E_{coll} = 76 kcal mol^{-1}. The black dots are the experimental data and the solid line is the forward convolution fit to the data.

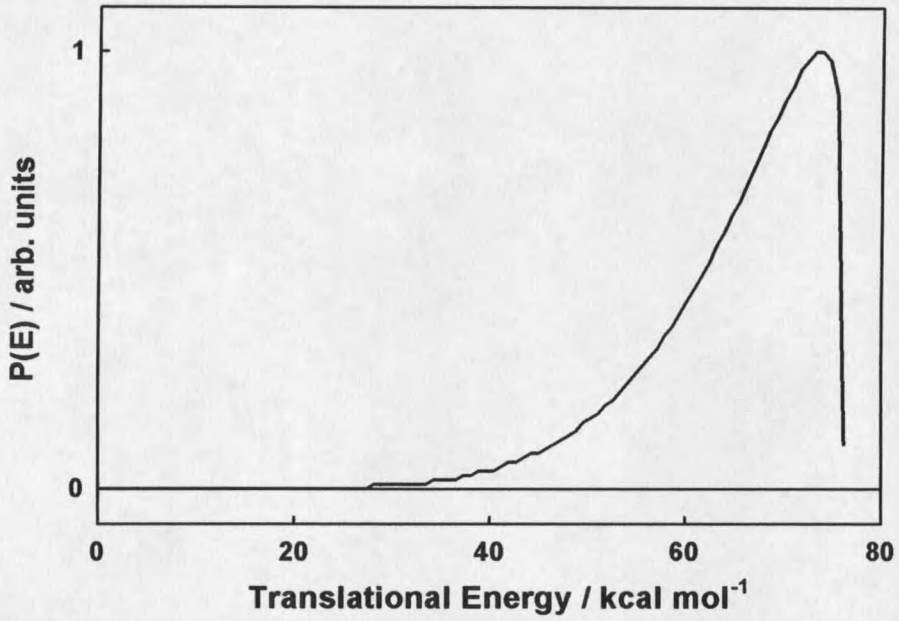

Figure 6.10. Center-of-mass translational energy distribution for the inelastic scattering of CD_4 from $O(^3P)$ at E_{coll} = 76 kcal mol^{-1} derived from the TOF and laboratory angular distributions for m/z = 20 (CD_4^+) through the forward convolution method.

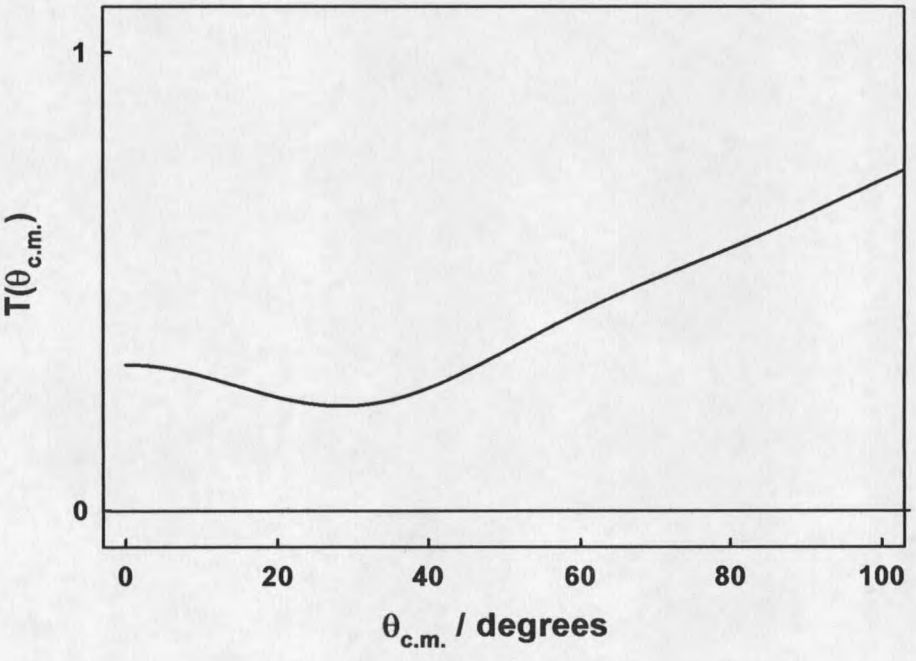

Figure 6.11. Center-of-mass angular distribution for the CD_4 product from inelastic scattering from $O(^3P)$ at E_{coll} = 76 kcal mol^{-1} derived from the TOF and laboratory angular distributions for m/z = 20 (CD_4^+) through the forward convolution method.

in the c.m. frame (i.e., forward scattering for CD_4). Although we are not sensitive to the forward scattered component of CD_4, we expect forward scattering of the CD_4 to be very large compared to backwards scattered CD_4. A c.m. velocity-flux contour plot of CD_4 scattering from oxygen atoms in the range that the experimental data is sensitive to is shown in Fig. 6.12.

Reactive scattering

In addition to the well known OH formation reaction, we have observed for the first time direct evidence of the hydrogen atom elimination reaction, $O(^3P) + CH_4 \rightarrow OCH_3 + H$. Experimental results for the excitation function for this reaction were presented in Chapter 5. Like the reaction of $O(^3P)$ with CH_4, the reaction of $O(^3P)$ with CD_4 at hyperthermal collision energies proceeds through both hydrogen atom abstraction and elimination channels. Time-of-flight distributions for products detected at m/z = 18 ($^{18}O^+$, OD^+), 28 (CO^+), 30 (CDO^+), 32 (O_2^+, OCD_2^+), and 34 ($O^{18}O^{16+}$, OOD^+) are shown in Fig. 6.13. These data were collected at a laboratory angle of 6.5° and with a collision energy of 73 kcal mol^{-1}. The OD formation channel was presumed to have similar dynamics as the OH channel discussed previously and was not examined with CD_4. A further reason that the D atom abstraction reaction was not investigated was because of interference from ^{18}O and the large background in the detector from H_2O^+ at m/z = 18, the mass at which the OD fragment would be detected. Therefore, this section will focus on the dynamics of the hydrogen atom elimination channel.

Similar to what was observed in the $O + CH_4$ reaction discussed in Chapter 5, the cracking pattern at m/z = 30 and 32 suggests detection of OCD_2, a secondary dissociation product created from the primary OCD_3 product (which has a large amount of internal energy from the reactive collision). Most of the signal for the OCD_3 product is detected at m/z = 28, 30, and 32. There is no signal detected at m/z = 34 at the expected arrival time for the OCD_3 product, indicating that isomerization to the more stable $DOCD_2$ radical is not as prevalent

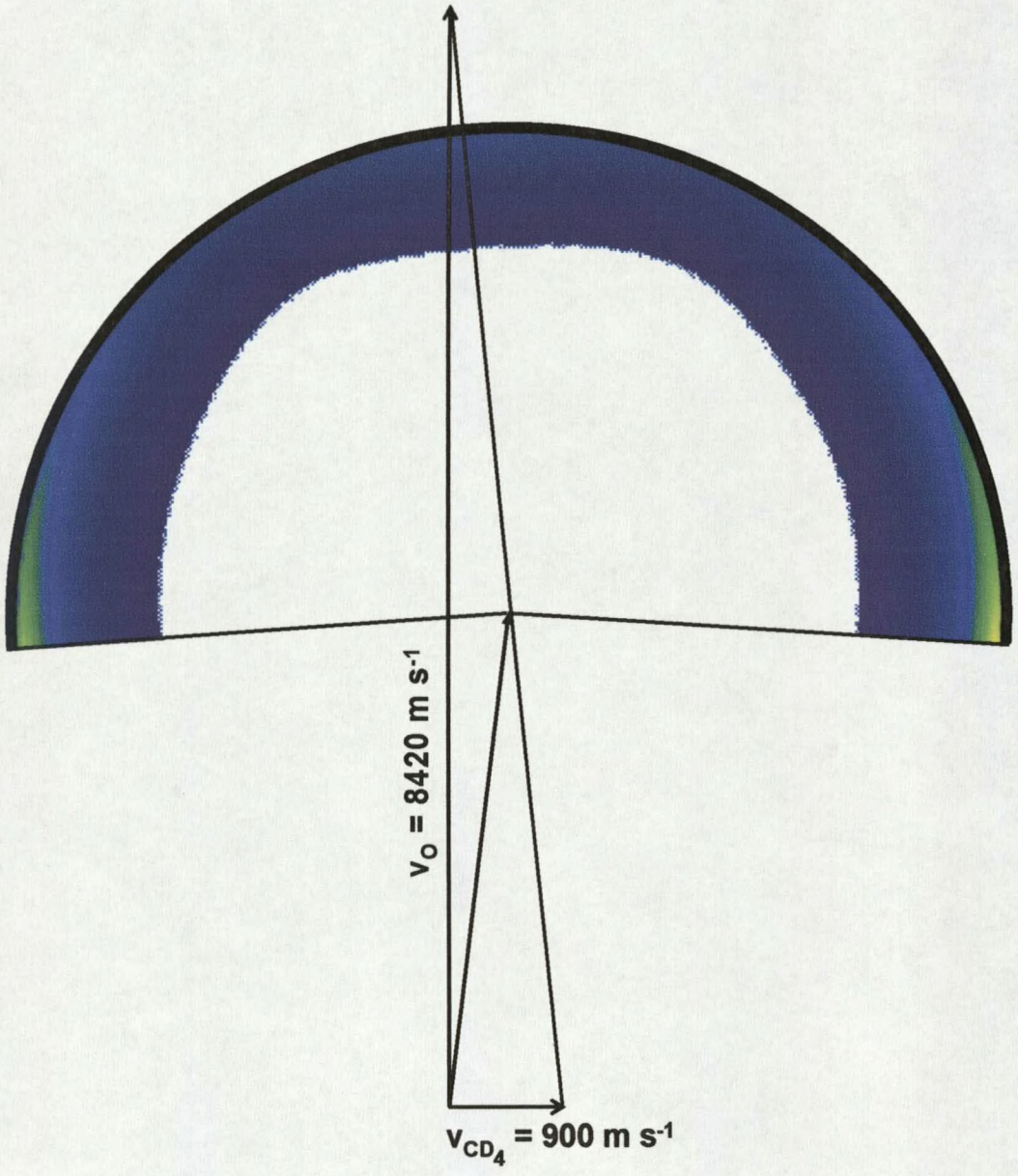

Figure 6.12. Center-of-mass velocity-flux map superimposed on a Newton diagram for CD_4 inelastically scattering from $O(^3P)$ at E_{coll} = 76 kcal mol^{-1}. Only the range of the contour plot for which the experiments are sensitive is shown.

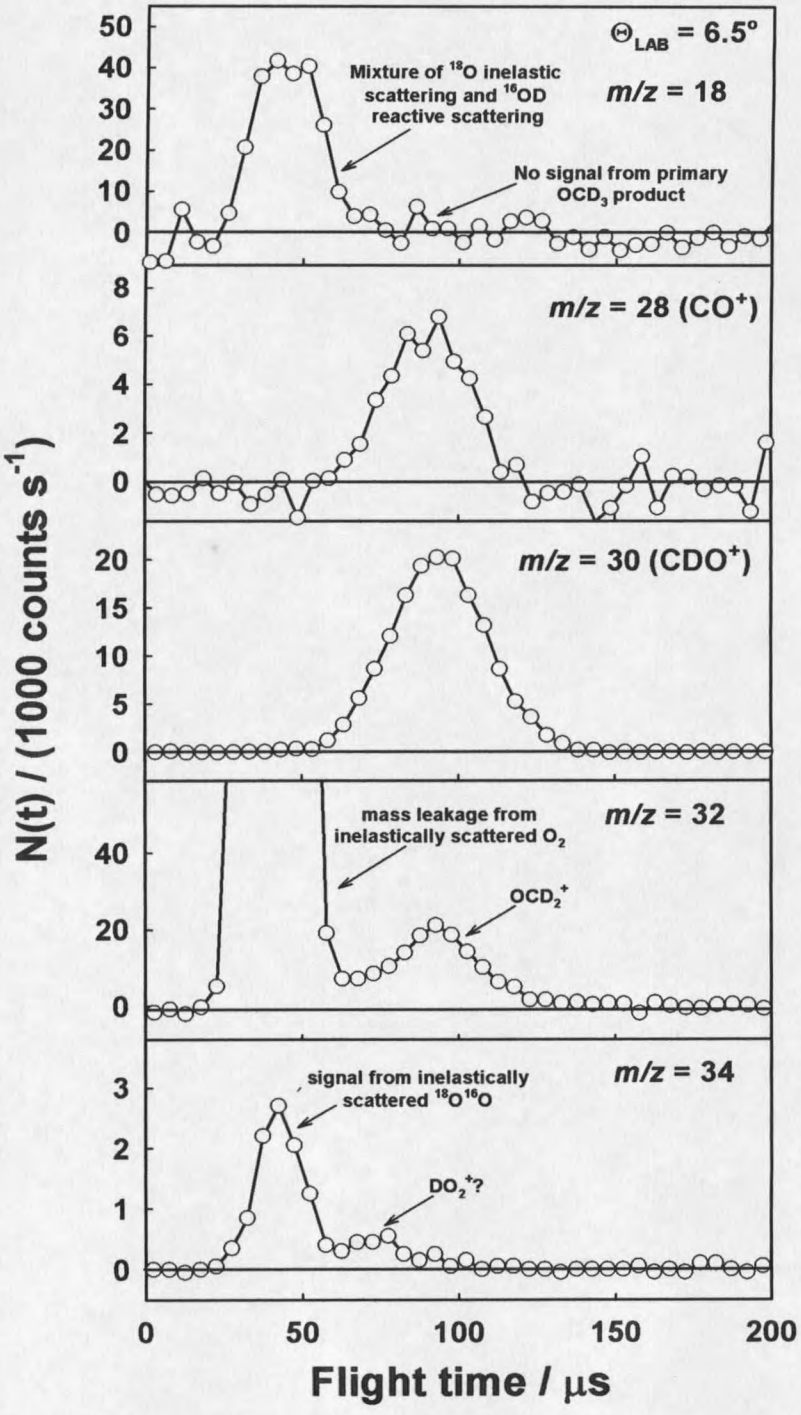

Figure 6.13. Representative time-of-flight distributions collected at five different mass-to-charge ratios resulting from $O(^3P)$ colliding with CD_4 at E_{coll} = 73 kcal mol^{-1} and at Θ_{LAB} = 6.5°. The open circles are the experimental data. A solid line is used to connect the data points.

as in the O + CH_4 case, where the $HOCH_2^+$ ion fragment was observed at $m/z = 31$ at the same arrival time to the detector as the other OCH_3 fragments. Further evidence supporting more complete secondary dissociation of the OCD_3 product can be seen upon comparing the signal at $m/z = 15$ (CH_3^+) and $m/z = 18$ (CD_3^+) shown in Fig 6.14. There is no peak at the expected flight time for the OCD_3 product present at $m/z = 18$ (CD_3^+), although there is for $m/z = 15$ (CH_3^+), suggesting complete secondary dissociation of the OCD_3 product. The slightly higher collision energy in the oxygen atom reaction with CD_4 compared to the reaction with CH_4, 73 vs. 67 kcal mol^{-1}, may be contributing to the larger degree of secondary dissociation observed in the O + $CD_4 \rightarrow OCD_3$ + D reaction.

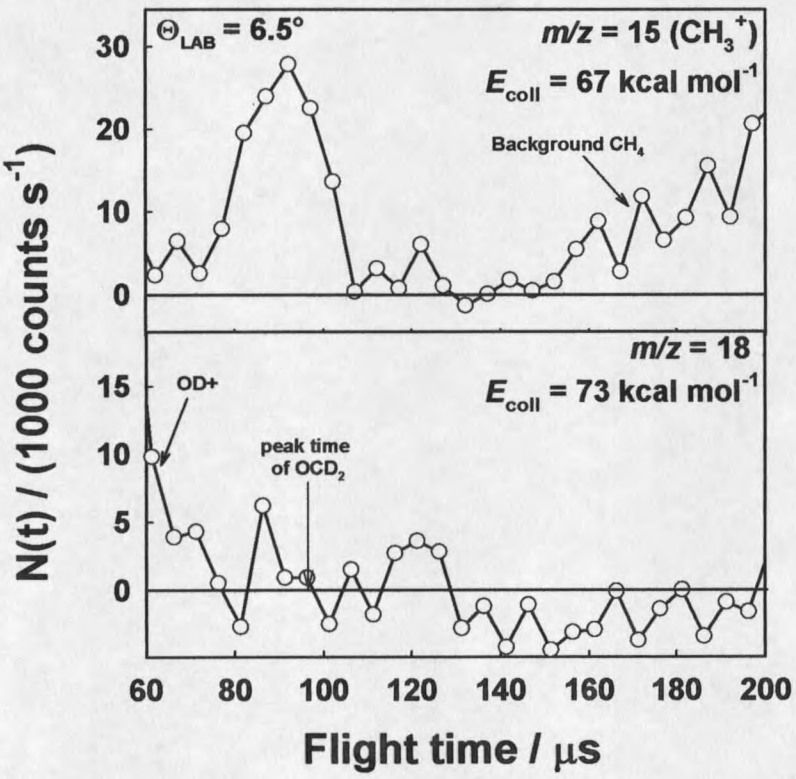

Figure 6.14. Time-of-flight distributions of $m/z = 15$ (CH_3^+) collected at E_{coll} = 67 kcal mol^{-1} in the reaction of $O(^3P)$ with CH_4 (above). Time-of-flight distributions of $m/z = 18$ (CD_3^+) collected at E_{coll} = 76 kcal mol^{-1} in the reaction of $O(^3P)$ with CD_4 (below). The predicted peak time of the OCD_2 is obtained from peak times at $m/z = 28$ (CO^+) and $m/z = 30$ (CDO^+).

Secondary dissociation of the primary reaction product, OCD_3, may or may not have a large impact on the observed scattering dynamics. Example Newton diagrams for the reaction of $O(^3P)$ with CD_4 showing the OCD_3 product Newton circle and a second Newton circle representing the secondary dissociation product OCD_2 are shown in Fig. 6.15. If the Newton circle from the secondary dissociation product of the OCD_3 is small relative to the OCD_3 Newton circle, i.e., the velocity of the OCD_2 in the c.m. frame is much less than the velocity of the OCD_3 (Case 2, Fig. 6.15), the dynamics observed at $m/z = 30$ (OCD_2^+) will not be significantly affected within our velocity resolution, because the OCD_2 velocities and directions do not differ much from those of the primary OCD_3 product. So, the scattering will be dominated by the OCD_3 product recoiling from a D atom. However, if the Newton circle from the OCD_2 product is comparable in size to or larger than the OCD_3 Newton circle (Case 1, Fig. 6.15), the true dynamics of the OCD_3 product will not be obtainable from the data in which the secondary OCD_2 product is detected. For the moment, we will assume that the dynamics more closely follow Case 2, where the primary OCD_3 is significantly faster than the OCD_2 secondary dissociation fragment, and conduct the analysis assuming that the $m/z = 30$ (CDO^+) signal reflects the dynamics of the primary OCD_3 product. Representative TOF distributions of the $m/z = 30$ (CDO^+) ionizer fragment collected at six lab angles and with E_{coll} = 78 kcal mol^{-1} are shown in Fig. 6.16, and the corresponding laboratory angular distribution is shown in Fig. 6.17. The signal at $m/z = 30$ decays away at a lab angle of ~20°. The laboratory angular distribution at $m/z = 30$, which gradually decreases from 5°, is distinctly different from the OH angular distribution in Fig. 6.4, which peaks around 17°. The point at 5° may be higher than predicted because of secondary dissociation or other apparatus effects not taken into account.

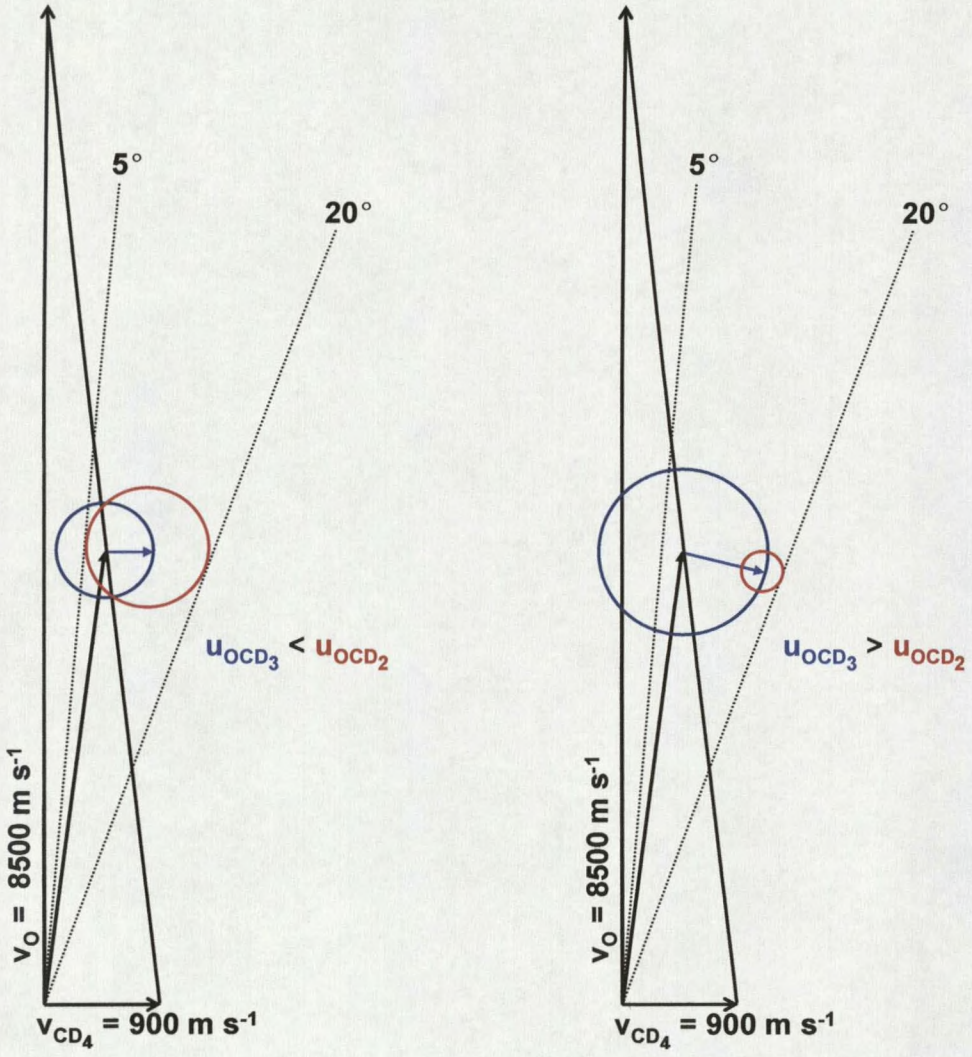

Figure 6.15. Newton diagrams for $O(^3P) + CD_4 \rightarrow OCD_3 + D$, showing the OCD_3 Newton circle (blue). If the OCD_3 undergoes secondary dissociation to OCD_2, its scattering will appear as a second Newton circle (red) with its center-of-mass directly on and all around the OCD_3 Newton circle. The OCD_2 scattering will therefore appear as a shell around the OCD_3 Newton circle. Two cases are shown. **Case 1:** In the Newton diagram to the left, 20 percent of the available energy in the $O(^3P) + CD_4$ reaction goes into translation of the OCD_3 and D products, resulting in a small primary Newton circle for OCD_3. In order to see the OCD_2 signal die off at a lab angle of 20° (what is observed in the experiments) the c.m. velocity of the secondary dissociation fragment, OCD_2 must be large relative to the c.m. velocity of the OCD_3. **Case 2:** On the right, 60 percent of the available energy for the $O(^3P) + CD_4$ reaction is going into translation of the OCD_3 product. In this case, the c.m. velocity of the OCD_2 secdonary dissociation fragment must be small compared to the c.m. velocity of the parent OCD_3 in order to see the decline in signal at 20°. In this second case, the dynamical properties of the OCD_2 product will more closely reflect the dynamics of the original OCD_3 product.

Figures 6.18 and 6.19 show the c.m. translational energy and angular distributions for $m/z = 30$ that were derived from the TOF and lab angular distributions in Figs. 6.16 and 6.17, respectively. The very broad translational energy and angular distributions are most likely the result of the secondary dissociation process. We must therefore think of these distributions more as "effective" distributions encompassing all processes that lead to signal at $m/z = 30$, rather than distributions detailing the behavior of the OCD_3 product alone. The broad translational energy distribution has a maximum around 13 kcal mol^{-1}, corresponding to only about 20 percent of the available energy. Because the translational energy distribution has a maximum at relatively low energy, the resolution of the c.m. angular distribution derived from the forward convolution method is reduced, because the lower the product velocity, the smaller the effective Newton circle, and the more difficult it is to discern forward and backward peaks, regardless of the angular distribution. Nonetheless, closest simulation of the data is obtained when the c.m. angular distribution is relatively isotropic as shown. The broad and featureless nature of the translational energy and angular distributions suggest that perhaps our initial assumption that the c.m. velocity of the OCD_3 was much larger than the secondary dissociation product, OCD_2, may not be entirely correct. Shown as dashed lines in Figs. 6.18 and 6.19 are translational energy and angular distribution results from MSINDO direct dynamics calculations by Schatz *et al.* for the $O + CD_4 \rightarrow OCD_3 + D$ reaction at a collision energy of 71 kcal mol^{-1}. In the direct dynamics calculations, the trajectories were not run long enough to observe secondary dissociation of the OCD_3 fragment, so the results obtained are absent of any affects due to secondary dissociation. The translational energy distribution from these calculations has a maximum at much higher energy than the experimental results, despite a lower collision energy, and the peak is also narrower. The general features of the experimental and calculated angular distributions are similar, they both rise up at small and large c.m. angles with a drop in the middle. However, the calculated distribution shows

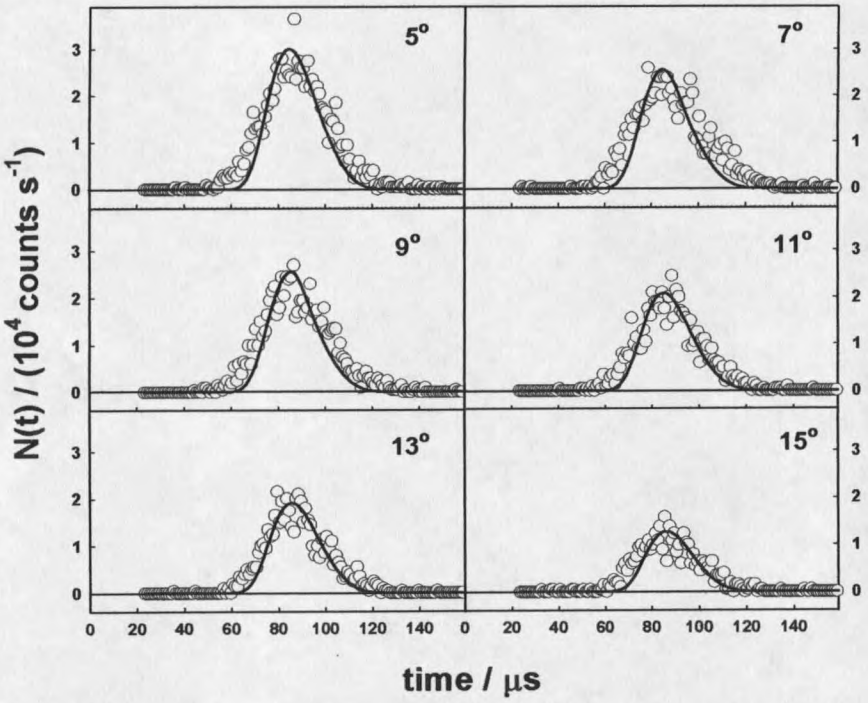

Figure 6.16. Representative time-of-flight distributions of the OCD_3 product from the reaction of $O(^3P) + CD_4 \rightarrow OCD_3 + D$ at E_{coll} = 76 kcal mol^{-1}. The open circles are the experimental data. The solid line is the forward convolution simulation to the data, based on c.m. angular and translational energy distributions shown in Figs. 6.18 and 6.19.

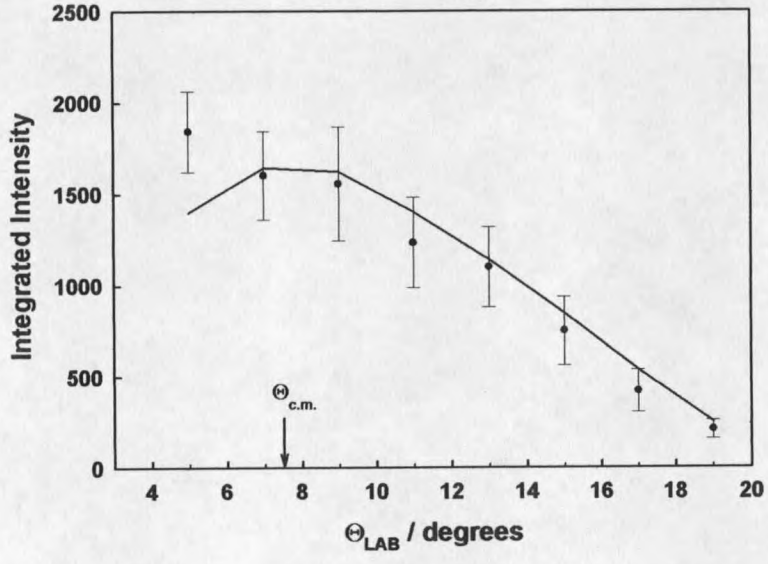

Figure 6.17. Laboratory angular distribution of the OCD_3 product from the reaction of $O(^3P)$ with CD_4 with E_{coll} = 76 kcal mol^{-1}. The circles are the experimental data and the solid line is the forward convolution fit to the data.

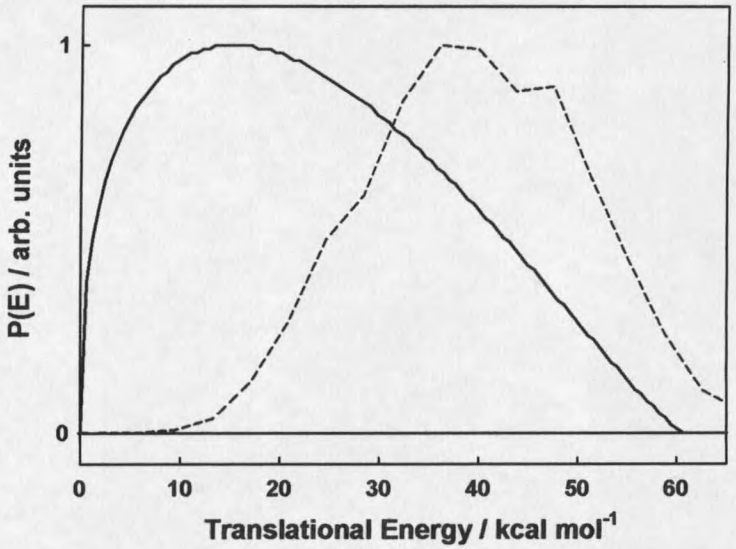

Figure 6.18. The solid line represents the center-of-mass translational energy distribution for the $O(^3P) + CD_4 \rightarrow D + OCD_3$ reaction at E_{coll} = 78 kcal mol^{-1}, obtained from the TOF and laboratory angular distributions for m/z = 30 (CDO^+) through the forward convolution method. The dashed line is the distribution obtained from MSINDO direct dynamics calculations for E_{coll} = 71 kcal mol^{-1}.

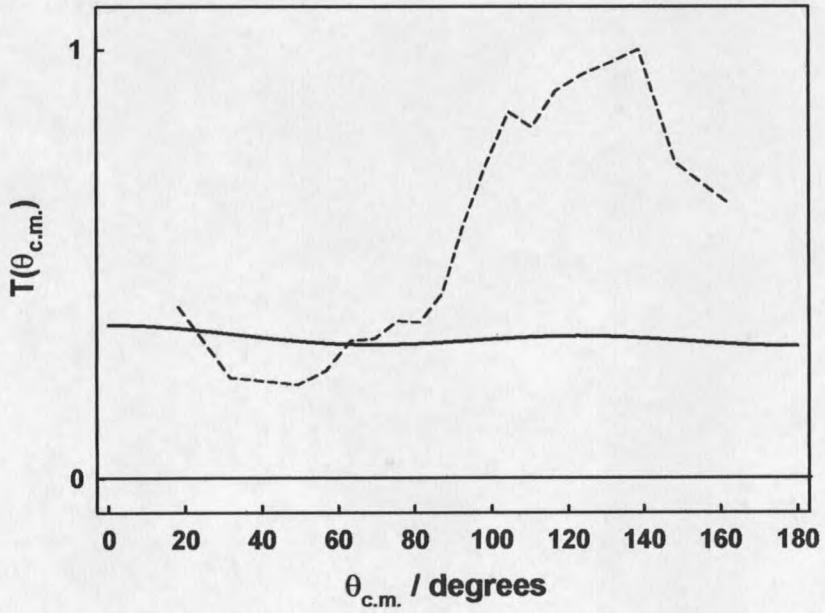

Figure 6.19. Center-of-mass angular distribution of the OCD_3 product from the reaction of $O(^3P) + CD_4 \rightarrow D + OCD_3$ reaction at E_{coll} = 78 kcal mol^{-1}, obtained from the TOF and laboratory angular distributions for m/z = 30 (CDO^+) through the forward convolution method. The dashed line is the distribution obtained from MSINDO direct dynamics calculations for E_{coll} = 71 kcal mol^{-1}.

much more backwards scattering than forward, while the experimental distribution shows about the same amount of forward and backwards scattering. In light of these comparisons, it seems that secondary dissociation is indeed perturbing the experimental results on the dynamics of the reaction pathway that produces OCD_3 as a primary product.

Relative Yields of Primary Reactive Pathways for $O(^3P) + CH_4$

The relative yield of a particular reaction is the fraction of reactive collisions that lead to specific products. In the $O(^3P)$ reaction with CH_4, the possible primary product channels are $OH + CH_3$ and $OCH_3 + H$. In order to estimate the relative yields of these two channels, the relative cross section of each reaction channel must be determined and the relative detection efficiency of each product must be known. In these experiments, relative cross sections are derived from scaling the calculated TOF distributions obtained from the input c.m. translational energy and angular distributions to fit the experimental TOF data in the forward convolution simulation to the data. The c.m. translational energy and angular distributions from the $O(^3P) + CD_4 \rightarrow OCD_3 + D$ reaction were used to obtain the relative cross section for the hydrogen atom elimination channel with CH_4. This was necessary because in order to obtain a ratio of relative cross sections from different reaction channels, TOF distributions for all products must be collected under identical conditions. The best TOF distributions for both the OH and OCH_3 formation channels were collected with CH_4 as the reactant, and not CD_4. So, for the purposes of determining a relative yield, it was necessary to assume that the c.m. translational energy and angular distributions for the $O(^3P) + CH_4 \rightarrow OCH_3 + H$ reaction would be the same (or at least similar) to those obtained from the analogous reaction with CD_4. The relative cross section calculated in the forward convolution simulation is sensitive to the both the translational energy and angular distributions used to simulate the experimental

TOF data. Because the experimental data has the complication of secondary dissociation affecting the derived c.m. translational energy and angular distributions, c.m. distributions from direct dynamics calculations at the semiempirical (MSINDO) level from Schatz *et al.* on the reaction of $O(^3P)$ with CD_4 with no secondary dissociation, were also used to obtain a relative cross section via the same method of scaling the predicted TOF distributions to the experimental TOF distributions. The calculated and experimental relative cross sections provide a range in which the true relative cross section probably resides. Only about 56 percent of the total OCH_3 signal is detected at $m/z = 29$ (CHO^+), as a result of secondary dissociation or ionizer fragmentation to other masses (mostly $m/z = 15$, 28, and 30). Therefore, the relative cross section obtained from the $m/z = 29$ signal must be corrected to account for the signal at these other masses. This is done by dividing the relative cross section obtained from the $m/z = 29$ signal by 0.56. Determining the relative cross section for the OH formation channel is simpler, since ionizer fragmentation of OH to O is negligible and no corrections are needed for the OH relative cross section. Ionization efficiencies of the OH and OCH_2 product fragments also must be taken into account in determining the relative product yield, since the two species are not ionized and thus detected with equal efficiency. Published results of ionization efficiencies for OH and OCH_2 were 1.17 and 2.85 Å^2, respectively.[14,15] The relative cross sections are divided by their respective ionization efficiencies, and the relative product yield is then determined. The range of relative product yields of the two channels is estimated to be:

$$O(^3P) + CH_4 \rightarrow OH + CH_3 \qquad (60 - 80\%)$$
$$\rightarrow OCH_3 + H \qquad (20 - 40\%).$$

Although very approximate, this range of relative yields shows that the hydrogen elimination is a non-negligible and important reactive channel for $O(^3P)$ reactions with CH_4. The precise relative yield is elusive with the present data set since there is uncertainty in c.m. translational energy and angular distributions used for fitting the data. The assumption that these

distributions are the same for the OCH_3 and OCD_3 reactions with similar collision energies, though reasonable, is not entirely accurate, and the secondary dissociation process is perturbing the true distributions for the OCH_3 formation channel. However, we believe that the range provided is very conservative and provides a guideline with which a semiquantitative understanding of the relative importance of each channel can be viewed. It is interesting to note that although the barrier for the OCH_3 formation channel is much higher than that of the OH formation channel (45 kcal mol^{-1} vs. ~8 kcal mol^{-1}) at higher collision energies, the cross section of the hydrogen elimination channel becomes comparable to (and eventually exceeds) that of the hydrogen abstraction channel.[13]

Reactions Involving Molecular Oxygen

At least 20 percent of the oxygen beam is molecular oxygen, O_2. The amount of O_2 varies depending on beam conditions, but it is nonetheless present in all the experiments. In the experimental results discussed thus far, the sole reactants have been $O(^3P)$ and CH_4 or CD_4. The slower peak observed at $m/z = 34$ in the CD_4 experiment, however, cannot be assigned to any reactions involving oxygen atoms, and thus illuminates the possibility of molecular oxygen reacting with the CD_4. The fast signal at $m/z = 34$ (see Fig. 6.13) has the exact shape and arrival time as the $m/z = 32$ (O_2^+) peak, and the integrated $N(t)$ for $m/z = 34$ is 0.4 percent of the total integrated $N(t)$ for $m/z = 32$ and 34, corresponding to exactly the amount of ^{18}O expected to be observed in O_2, and we can therefore conclude that the fast peak is simply detection of $^{18}O^{16}O$. The slower peak, however, is more curious. Its peak arrival time to the detector, 76 μs, is faster than the peaks at $m/z = 28$, 30, and 32, the main fragments of the OCD_3 product, which arrive at 93 μs. In contrast, the $O + CH_4$ results (see Fig. 5.3) showed the $m/z = 31$ peak from OCH_3 arriving at exactly the same time as the $m/z = 28$, 29, and 30 peaks. It is thus possible that this slower signal at $m/z = 34$ could be coming

from a reaction of the ground, $O_2(^3\Sigma)$, or possibly first excited, $O_2(^1\Delta)$, species present in the hyperthermal beam. The reactive pathways with which O_2 can react with CD_4 to form a product that could be observed at m/z = 34 are $O_2(^3\Sigma) + CD_4 \rightarrow OOD + CD_3$, where the OOD^+ product ion is detected, and $O_2(^1\Delta) + CD_4 \rightarrow DOOD + CD_2$, where the DOOD product cracks to OOD. Direct dynamics calculations on $O_2(^3\Sigma, ^1\Delta) + CH_4$ by Schatz *et al.* add some insight into the possibility of reactions involving O_2. At a collision energy of 100 kcal mol^{-1} (O_2 beam velocity of 8240 m s^{-1}), the cross section for reaction of $O_2(^3\Sigma)$ to form OOH is negligible, even though the calculated barrier to reaction, ~55 kcal mol^{-1}, is greatly exceeded by the collision energy. The reaction of CH_4 with $O_2(^1\Delta)$ to form HOOH has a larger cross section, ~0.2 a.u., at a collision energy of 100 kcal mol^{-1}. However, the cross section for the reaction, $O_2(^1\Delta) + CH_4 \rightarrow H_2O + CH_2$, is 4 times larger, and therefore should be observable if any $O_2(^1\Delta)$ is present in the reactant beam. The presence of $O_2(^1\Delta)$ was therefore investigated by looking for evidence of H_2O and D_2O in the $O(^3P)$ reaction with CH_4 and CD_4, respectively. The predicted cross section is about one fifth the calculated cross section for $O + CH_4 \rightarrow OH + CH_3$ for O and O_2 velocities of 8240 m s^{-1}, already making it a challenge to observe in the experiment because of very low signal levels (e.g., see Fig. 6.3). In addition, the large exoergicity of this reaction results in very large predicted c.m. velocities, leading to an even more unlikely chance that the signal could be observed experimentally, because the fast products would be spread out in velocity space. Compounding the difficulty of observing the H_2O product is the high H_2O background in the detector, as mentioned earlier. After a thorough search for any sign of signal from H_2O at several lab angles and collision energies, none was found, suggesting that it is unlikely that there is a significant amount of $O_2(^1\Delta)$ is present in the hyperthermal beam. These results leave open the possibility that the slow peak at m/z = 34 might be coming from the $O_2(^3\Sigma) + CD_4 \rightarrow OOD + CD_3$ reaction (and the direct dynamics calculations underestimated the cross section) or that there is a tiny amount of $O_2(^1\Delta)$ present

that is reacting to form DOOD. In either case, these reactions occur with a low probability and can only barely be detected at $m/z = 34$, which has very low background in the mass spectrometer.

Discussion

Abstraction of a hydrogen atom to form OH is the only reactive channel observed when $O(^3P)$ encounters an alkane at low collision energies, and it is also the dominant channel at the high collision energies used in these experiments. Because the barrier for the $O(^3P) + CH_4 \rightarrow OH + CH_3$ is only ~8 kcal mol^{-1} (ΔE_r = 2.5 kcal mol^{-1}) and the experimental collision energy is 67 kcal mol^{-1}, there is a large excess of available energy for larger impact parameter collisions to lead to reaction, and therefore a stripping mechanism would be predicted.[8] The stripping mechanism has never been directly observed previously in the $O(^3P) + CH_4$ reaction. The experimental c.m. translational energy distribution (see Fig. 6.5) is relatively narrow and shows a peak near the available energy, suggesting that nearly all of that energy goes into translation, which is an indication that OH is formed from $O(^3P)$ stripping off a hydrogen atom. The large translational energies observed suggest that very little energy is transferred to internal modes of the OH and CH_3 fragments. Very little internal energy transfer is consistent with the picture of hydrogen abstraction from larger alkanes by $O(^3P)$ and $Cl(^2P)$ that has been developed from studies of hydrogen atom abstraction reactions at lower collision energies[1-10] and is also consistent with calculations done by Schatz *et al.* for $O(^3P) + CH_4$ at collision energies representative of those used in these experiments.[13] At 67 kcal mol^{-1}, the collision energy used for the $O + CH_4$ experiment described herein, direct dynamics calculations by Schatz *et al.* (employing B3LYP/6-31G*) suggested that ~93 percent of the available energy should be channeled into translation. A c.m. angular distribution showing forward

scattering is a second indication that the reaction is proceeding via a stripping mechanism, and indeed the experimentally obtained c.m. angular distribution (see Fig. 6.6) shows mostly forward scattering of the OH product, with at peak in the distribution at ~45°. Semiempirical (MSINDO) calculations by Schatz *et al.* matched well with this result, having a peak at ~48°. The location of the peak in the angular distribution being forward, but not directly forward (i.e., 0°), may be the result of hydrogen atoms neighboring the to-be-abstracted hydrogen atom interfering with a direct pathway to reaction which would lead OH scattering at 0°. MSINDO semiempirical calculations showed that at a collision energy of 54 kcal mol^{-1}, most of the reactive collisions occurred when the impact parameter was in the range of 1 to 5 a.u, and this range was shifted to higher minimum impact parameter values as the collision energy increased. The calculations also showed that the OH product shifted to more forward scattering as the collision energy increased, and this effect was interpreted not only as larger impact parameter collisions leading to reaction, but as the smaller impact parameters preferentially forming the OCH_3 product thereby closing down the mechanism for small impact parameter collisions leading to the OH product. Thus a sort of competition between the OH and OCH_3 channel develops at high collision energy. The presence of some smaller impact parameter collisions, however, likely accounts for the sideways scattered tail observed in the c.m. angular distribution. As seen from the velocity-flux contour map in Fig. 6.7, we are not sensitive to the backward scattered OH in these experiments. Backwards scattered OH is not predicted in the semiempirical calculations at the collision energies used in the experiment, but nonetheless some may still be present. We can conclude that most of the OH product is formed through a forward scattering, stripping type mechanism, where the $O(^3P)$ picks off a hydrogen atom during a glancing blow with the methane; however, some harder collisions can still lead to the formation of OH, but appear sideways (and maybe backwards) scattered in the c.m. angular distribution. These results seem to reinforce the validity of the triatomic model for hydrogen abstraction from CH_4 by $O(^3P)$.

Another novel result of these high collision energy experiments of $O(^3P)$ reacting with methane is the formation of the OCH_3, or methoxy radical, which accounts for somewhere between 20 and 40 percent of the reactive events. The collisions that will lead to formation of the OCH_3 product are much smaller impact parameter (more "head-on") collisions than was observed for the hydrogen abstraction channel, since the oxygen atoms must penetrate the hydrogen atoms to react directly with the carbon atom. In recent MSINDO direct dynamics calculations, Schatz *et al.* found that in collisions with impact parameters less than 1.5 a.u. the formation of OCH_3 was more likely than formation of OH. As a result of the harder collisions, significant energy transfer into internal modes was seen in the calculations, approximately 50 percent of the total available energy. Two transition states were found in these calculations, TS1 with an energy of about 47 kcal mol^{-1} and TS2 having an energy of 59 kcal mol^{-1}. The saddle point structures are shown in Fig. 5.6. Due to the geometry of the saddle point, the lower-energy saddle point structure would lead to backwards scattering of the OCH_3, while the higher-energy saddle point structure would lead to more isotropic scattering. At collision energies above 59 kcal mol^{-1}, barriers to both of the saddle points are exceeded, and therefore contributions from both would be expected in the scattering distributions. Semiempirical direct dynamics calculations showed that the OCH_3 products were scattered in the backwards direction for collision energies below 59 kcal mol^{-1}, indicating reaction via the lower energy saddle point, and as the collision energy was increased, the products became more isotropic with a slight favoring of the backwards direction.

The experimental results for the dynamics of the hydrogen elimination channel are much more difficult to extract from the scattering data than the hydrogen abstraction channel. There are several factors contributing to the complexity of studying OCH_3 formation, but perhaps the most difficult to unravel from our experimental data is the secondary dissociation of the internally excited OCD_3 to OCD_2 before reaching the ionizer. This process was identified

in the reaction of $O(^3P)$ with CH_4 in Chapter 5 by using published ionizer fragmentation patterns. An estimated 70 percent of the OCH_3 products underwent secondary dissociation before reaching the detector. With the higher collision energy of the $O(^3P) + CD_4$ reaction relative to that of the $O(^3P) + CH_4$ reaction, due in part to the increased reduced mass, more complete secondary dissociation to OCD_2 would be expected, and indeed, the lack of signal at the parent mass, $m/z = 34$ (OCD_3^+) and the lack of signal at $m/z = 18$ (CD_3^+) indicates that nearly all of the OCD_3 products underwent secondary dissociation before reaching the ionizer. The secondary dissociation process perturbs direct measurement of the translational energy and angular distributions of the primary OCD_3 product, because we are obtaining information about the parent product, OCD_3, by observing its dominant secondary fragment, OCD_2. We are therefore obtaining "effective" translational energy and angular distributions in these experiments. The degree of similarity between the "true" OCD_3 scattering distributions and the "effective" distributions is dependent on the velocity of the OCD_2 product following secondary dissocation. It is difficult to avoid secondary dissociation, because high collision energies are needed to surpass the 45 kcal mol^{-1} barrier. Therefore, in order to have enough energy to make the reaction occur, there is enough energy to cause secondary dissociation. In addition to the secondary dissociation, the OCD_3 product, if it reaches the ionizer intact, cracks to smaller mass fragments, leading to detection of the product at $m/z = 28$ (CO^+), 30 (CDO^+), and 32 (OCD_2^+), reducing signal levels at each mass. Nonetheless, scattering distributions for the $m/z = 30$ (CDO^+) product were obtained and used to gain insight into the reaction dynamics governing the formation of OCD_3.

The experimental c.m. translational energy distribution of the OCD_3 product shows that approximately 70 percent of the available energy is transferred into internal energy. Semiempirical calculations by Schatz *et al.* for $O + CH_4 \rightarrow H + OCH_3$ suggest that ~55 percent of the available energy goes into internal energy, much less than the experiment

suggests. The discrepancy between the experimental and theoretical results might be the result of the level of theory used, or it could be accounted for upon consideration of the secondary dissociation process. If we assume that the calculations are correct and only 55 percent of the available energy in the $O + CD_4 \rightarrow OCD_3 + D$ reaction goes into translation, we would have conditions resembling Case 2 in Fig. 6.15. The c.m. velocity of the OCD_3 could be determined exactly by assuming that 55 percent of the available energy goes into translation, and the c.m. velocity of the OCD_2 secondary dissociation product can be estimated by the fact that the reactive signal is gone at a lab angle of 20°. A Newton diagram illustrating these conditions is shown in Fig. 6.20. The OCD_2 Newton circles around the OCD_3 Newton circle will be more tightly packed on the inside of the OCD_3 Newton circle than outside, resulting in kinematic focusing of the OCD_2 product. The observed translational energy distribution would thus be biased toward lower energies, which is what is observed. The calculated and experimental c.m. angular distributions were both relatively isotropic; however, the calculated distribution more heavily favored scattering in the backwards direction. The lack of sensitivity of the angular distribution as a result of the translational energy distribution having a peak at low energy, could account for the differences observed. Nonetheless, more accurate DFT direct dynamics calculations are currently being run (in the Schatz group) on the $O + CD_4$ system, in order to improve the accuracy of the calculations and thus gain further insight into the scattering dynamics.

The relative yields of the two reaction products, OH and OCH_3, and corresponding B3LYP/6-31G* calculations were in good agreement. The calculations showed that approximately 30 to 40 percent of the reactive trajectories led to OCH_3 formation,[13] while the experimental results gave the range of 20 to 40 percent. Based on the calculations it is likely that the upper limit in the experimental range is probably the best estimate of the relative yield. An interesting result that emerged from the calculations by Schatz, *et al.* showed that as the collision energy

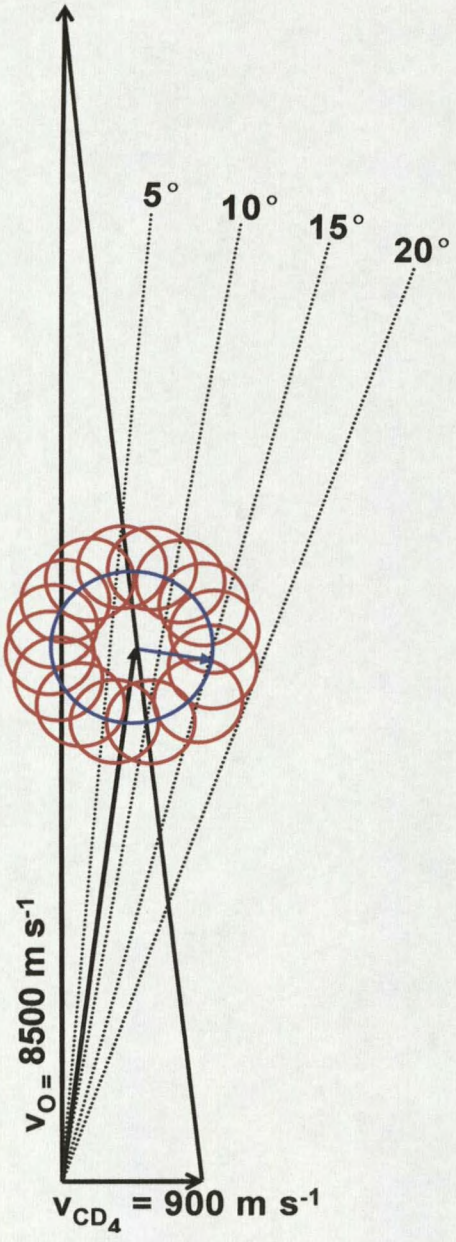

Figure 6.20. A Newton diagram for $O(^3P) + CD_4 \rightarrow OCD_3 + D$, showing the OCD_3 Newton circle (blue). If the OCD_3 undergoes secondary dissociation to OCD_2, its scattering will appear as a set of secondary Newton circles (red) with their center-of-masses directly on and all around the OCD_3 Newton circle. The OCD_2 scattering will therefore appear as a diffuse shell around the OCD_3 Newton circle. The case shown is for 55 percent of the available energy put into internal energy of the OCD_3 fragment. The resulting OCD_2 secondary dissociation fragment must show no signal beyond 20° in order to be consistent with the experiments. Therefore, a case in-between those shown in Fig. 6.15 is obtained and is believed to best reflect the hydrogen atom elimination reaction under our experimental conditions.

increases, the cross section for OCH_3 formation increases relative to the formation of OH, despite the fact that the barrier is ~35 kcal mol^{-1} higher. At low collision energies, the $O(^3P) + CH_4 \rightarrow OH + CH_3$ channel is dominant, but at collision energies above 100 kcal mol^{-1}, the $O(^3P) + CH_4 \rightarrow OCH_3 + H$ channel becomes dominant. The OCH_3 formation channel therefore seems to be very important under high collision energy conditions when an $O(^3P)$ atom encounters an alkane. Such reactions might be important in the hyperthermal reactions of oxygen atoms with hydrocarbon polymers on spacecraft in low Earth orbit. Formation of an oxy radical on a hydrocarbon surface would provide a direct pathway to the formation of CO and CO_2, and this initial reaction had not been considered previously in studying the erosion of hydrocarbon polymers by $O(^3P)$.

Another channel that was observed in the calculations but not observed unambiguously in the experiments was $O + CH_4 \rightarrow OCH_2 + 2H$. This mechanism has a relatively small cross section in the calculations and, if it is occurring, would not have a large contribution to the total cross section. A water formation channel was also observed in the calculations. However, the cross section for this channel was even lower, and there was no experimental evidence for this channel.

Molecular oxygen played a negligible role in these experiments, save a small, slow signal at $m/z = 34$ in the CD_4 experiment. This small peak could not be easily correlated with any channels in which $O(^3P)$ was the reactant. We therefore suggested the possibility of the formation of DOO from $O_2(^3\Sigma)$ or DOOD from $O_2(^1\Delta)$. While we looked for $O_2(^1\Delta)$ trying to detect H_2O from the reaction, $O_2(^1\Delta) + CH_4 \rightarrow H_2O + CH_2$, none was detected, although its detection was difficult because the cross section is relatively low and the background in the detector at $m/z = 18$ was high. Therefore, a very small amount of $O_2(^1\Delta)$ may be present. More data would be required to confidently assign the small peak observed at $m/z = 34$ to the $O_2(^3\Sigma)$ or $O_2(^1\Delta)$ channel.

Conclusion

Two primary reaction channels have been identified in the reaction of $O(^3P)$ with methane: $O(^3P) + CH_4 \rightarrow OH + CH_3$ and $O(^3P) + CH_4 \rightarrow OCH_3 + H$. The OH product is formed mainly through a stripping mechanism where the $O(^3P)$ has large impact parameter collisions with the CH_4, and very little energy is transferred into internal modes. Some of the OH products are formed through smaller impact parameter collisions, leading to sideways (and probably backwards) scattering, although a competition for small impact parameter collisions to lead to OH or OCH_3 develops at high collision energies. The widely accepted triatomic model for the interaction between an $O(^3P)$ atom and an alkane molecule is still applicable at the collision energies used in the experiments. The OH and CH_3 products have relatively cold vibrational and rotational distributions. Good agreement was obtained between direct dynamics calculated values of energy transfer and c.m. angular distributions and the experimental results.

Inelastic scattering of CD_4 from $O(^3P)$ was observed. The c.m. translational energy distribution showed a broad range of energy transfer into the scattered CD_4. Some collisions appeared have large amounts (~50 percent) of the collision energy transferred into internal energy in a sort of "super collision". In addition, the angular distribution showed scattering in the forward direction, with scattering decreasing in the sideways (and backwards) directions.

The hydrogen atom elimination channel was observed in the reaction of $O(^3P)$ with CD_4 and was found to account for 20 - 40 percent of the total reactive events. Much of the available energy, ~50 percent, is transferred into internal modes of the OCD_3. The excitation of internal modes leads to significant secondary dissociation of the OCD_3 into $OCD_2 + D$ before ionization. The signal at $m/z = 30$ (CDO^+) was used to examine the dynamics of the hydrogen elimination channel because of the high signal levels and low background, but as a

result of secondary dissociation, only "effective" c.m. distributions could be obtained. The experimental translational energy and angular distributions resemble the dynamics of the OCD_3 product, with the exception of bias to lower energies in the translational energy distribution due to kinematic focusing from secondary dissociation and overly broad and isotropic scattering in the c.m. angular distribution.

Although molecular oxygen is present in the hyperthermal beam, it played a negligible role in the observed dynamics. A small signal at $m/z = 34$ may be attributed to reaction of O_2 with CD_4, but more data would be required to confirm the reactive pathway.

References

1. T. Suzuki and E. Hirota, *J. Chem. Phys.* **98**, 2387 (1993).
2. G. M. Sweeney, A. Watson, and K. G. McKendrick, *J. Chem. Phys.* **106**, 9172 (1997).
3. P. Andresen and A. C. Luntz, *J. Chem. Phys.* **72**, 5842 (1980).
4. N. J. Dutton, I. W. Fletcher, and J. C. Whitehead, *Mol. Phys.* **52**, 475 (1984).
5. S. P. Walch and T. H. Dunning, Jr., *J. Chem. Phys.* **72**, 3221 (1980).
6. A. C. Luntz and P. Andresen, *J. Chem. Phys.* **72**, 5851 (1980).
7. C. Gonzalez, J. J. W. MCDouall, and H. B. Schlegel, *J. Phys. Chem.* **94**, 7467 (1990).
8. R. D. Levine and R. B. Berstein, Molecular Reaction Dynamics and Chemical Reactivity (Oxford University Press, New York, 1987).
9. H. Tsurumaki, Y. Fujimura, and O. Kajimoto, *J. Chem. Phys.* **112**, 5851 (2000).
10. D. Blank, N. Hemmi, A. G. Suits, and Y. T. Lee, *Chem. Phys.* **231**, 261 (1998).
11. D. F. Varley and P. J. Dagdigian, *Chem. Phys. Lett.* **255**, 393 (1996).
12. W. R. Simpson, A. J. Orr-Ewing, and R. N. Zare, *Chem. Phys. Lett.* **212**, 163 (1993).
13. D. Troya, R. Z. Pascual, and G. C. Schatz, *J. Phys. Chem. A* **107**, 10497 (2003).
14. Y-K Kim and J-P Desclaux, *Phys. Rev. A* **66**, 12708 (2002).
15. K. N. Joshipura, M. Vinodkumar, and U. M. Patel, *J. Phys. B* **34**, 509 (2001).

CONCLUSION

The experiments described in this thesis represent the first ever crossed molecular beams experiments done in the hyperthermal collision energy regime. These experiments pushed the limits of the crossed molecular beam technique employing "universal" electron impact ionization on several levels. In particular, velocity and time resolution presented significant challenges, especially in deciphering secondary dissociation and dissociative ionization events. In forging new ground, however, several important results emerged. Concurrent to these experiments, the same systems were investigated theoretically by the group of George Schatz at Northwestern University. The experiments provided crucial input for the validity of different theoretical methods, and in turn the theoretical results were also critical in the interpretation of some of the experimental results.

In Chapter 3, the electronic state distribution of oxygen atoms in the hyperthermal beams was characterized by measuring the excitation function for OH formation in the reaction, $O(^3P) + H_2 \rightarrow OH + H$. These data represent the first observation of this reaction in a crossed molecular beams experiment. Upon comparing the experimental excitation function with excitation functions predicted by very accurate theoretical calculations on the two lowest triplet surfaces ($^3A''$ and $^3A'$), essentially all (>99 percent) of the oxygen atoms in the beam were determined to be in ground $O(^3P)$ electronic state. Comparison with theoretical results also allowed the conclusion to be drawn that intersystem crossing does not occur at the collision energies used in the experiments. The experimental excitation function also provided a measurement of the barrier for hydrogen atom abstraction by $O(^3P)$ from H_2, which was found to be ~10 kcal mol^{-1}.

Once we established that the oxygen atoms in the hyperthermal beam were in the $O(^3P)$ state, experiments on the dynamics of the interaction of $O(^3P) + D_2 \rightarrow OD + D$ were performed. The OD product was found to be predominantly sideways and backwards scattered, with about 50 percent of the available energy channeled into internal excitation of the OD product. In this experiment, there was little evidence of intersystem crossing, however, because of resolution limitations, we cannot rule out that a tiny amount (<5 percent) of intersystem crossing might be occurring. The experimental conclusion that the reaction of $O(^3P)$ with D_2 proceeds on triplet potential energy surfaces was somewhat surprising, because theoretical calculations predicted as much as 40 percent of the reactive events might involve triplet-singlet crossing and yield products that exhibit singlet dynamics. The inelastic scattering of $O(^3P)$ from D_2 was also investigated and revealed very little translational to vibrational/ rotational energy transfer in hyperthermal collisions of $O(^3P)$ with D_2.

In addition to hydrogen, reactions of $O(^3P)$ with methane were also studied. An exciting result that emerged from these experiments was the discovery of a new channel in the $O(^3P)$ reaction with CH_4: hydrogen-atom elimination to form OCH_3. This product is formed internally hot, and undergoes secondary dissociation. The excitation function for the reaction, $O(^3P) + CH_4 \rightarrow OCH_3 + H$, was measured and matched well with a theoretical calculation of the excitation function that involved reaction only on the two lowest lying triplet potential energy surfaces, $1^3A + 2^3A$. Comparison of experiment and theory (which again suggested that intersystem crossing might be possible) showed no evidence for intersystem crossing in the experimental results. The barrier for the $O(^3P) + CH_4 \rightarrow OCH_3 + H$ reaction was measured and was found to be ~45 kcal mol^{-1}.

The dynamics of the reaction of $O(^3P)$ with methane were investigated. The hydrogen-atom abstraction (i.e., OH formation) channel was observed. While previous studies observed the OH product to be backwards scattered, we found the OH to be forward-scattered,

indicating that a stripping mechanism was occurring, the first time such a mechanism has been observed in $O(^3P)$ reactions with methane. The hydrogen-atom elimination channel was observed in the reaction of $O(^3P)$ with CD_4, although secondary dissociation of the OCD_3 product precluded a detailed examination of the dynamics. The secondary dissocation also added uncertainty in the calculation of the relative product yields for the reaction of $O(^3P)$ with methane; however, we were able to determine that ~20 - 40 percent of the reactive events lead to the formation of OCH_3 and ~60 - 80 percent lead to OH formation. In studying the inelastic scattering of CD_4 from $O(^3P)$, a small amount of energy transfer into internal modes of the CD_4 was observed. The possible involvement of O_2 in the reactions with methane was investigated and was found to play a negligible role.

While the results described in this thesis are very fundamental, they have far-reaching implications, particularly in the study of chemistries occurring in the low Earth orbit (LEO) environment. All of the experimental results in this thesis are being incorporated into theoretical models aimed at accurately describing hydrocarbon erosion and plume signatures in LEO, and many of the experimental results were not intuitive or predicted by theory. The hydrogen-atom elimination channel, which has a very large barrier, may be commonplace in the hyperthermal reactions occurring in LEO, but it is not intuitive when thinking in the context of typical terrestrial environments. Although it is invaluable in developing a detailed picture of the dynamics, we cannot completely rely on theory to predict events at these collision energies, because it needs to be calibrated. For example, theory predicted intersystem crossing for both $O(^3P) + H_2$ and CH_4 reactions, but it is not observed in the experiments.

Confirmation that the oxygen-atom beam is essentially all $O(^3P)$ provided confidence for future studies, both gas-surface and gas-phase, that the experiments faithfully represent the atomic-oxygen chemistry involving spacecraft in LEO. The hydrogen-atom elimination channel that has been identified in these experiments have also been seen in $O(^3P)$ reactions with ethane and propane, so it is likely occurring also on hydrocarbon surfaces. If an oxygen atom

can be added to a hydrocarbon surface in one collision, the next collision can lead to production of volatile CO and CO_2, thereby causing material removal from the surface.

The model hyperthermal $O(^3P)$ reactions presented in this thesis have provided much new insight into chemical reactivity in an unexplored regime of collision energies and will undoubtedly serve as a guide for further investigations aimed at understanding the chemistries occurring in the interaction of spacecraft and LEO environment.